DIRECT NUMERICAL SIMULATIONS OF WAVE-CURRENT INTERACTIONS OVER BUMPY WALLS

A DISSERTATION
SUBMITTED TO THE DEPARTMENT OF CIVIL AND ENVIRONMENTAL ENGINEERING
AND THE COMMITTEE ON GRADUATE STUDIES
OF STANFORD UNIVERSITY
IN PARTIAL FULFILLMENT OF THE REQUIREMENTS
FOR THE DEGREE OF
DOCTOR OF PHILOSOPHY

Akshay Patil

March 2023

This dissertation is online at: https://purl.stanford.edu/hc108hs0779

I certify that I have read this dissertation and that, in my opinion, it is fully adequate in scope and quality as a dissertation for the degree of Doctor of Philosophy.

Oliver Fringer, Primary Adviser

I certify that I have read this dissertation and that, in my opinion, it is fully adequate in scope and quality as a dissertation for the degree of Doctor of Philosophy.

Catherine Gorle

I certify that I have read this dissertation and that, in my opinion, it is fully adequate in scope and quality as a dissertation for the degree of Doctor of Philosophy.

Stephen Monismith

Approved for the Stanford University Committee on Graduate Studies.

Stacey F. Bent, Vice Provost for Graduate Education

This signature page was generated electronically upon submission of this dissertation in electronic format.

Abstract

Turbulence in estuarine bottom boundary layers influences a variety of biological and anthropogenic activities by driving the hydrodynamics and morphodynamic response of large-scale coastal ocean systems. Thus, a detailed understanding of these boundary layers enables accurate, long-term prediction of the fate of nutrients, pollutants, sediments, and other relevant quantities within estuarine environments. Typically, estuaries are driven by the mean turbulent currents and oscillatory wave motion that interact over naturally rough bottom boundaries. These wave-current interactions often occur non-linearly resulting in complex mean flow responses across the water column.

A direct forcing immersed boundary method was implemented in a second-order accurate, staggered finite-difference code enabling the modeling of rough-wall channel flows. Through the definition of the Corey shape factor (C_o), the effect of roughness shape characterisation on the mean flow drag was validated to show that the mean flow drag increases with decreasing C_o. Using a wide range of full- and minimal-span channel flow simulations with varying C_o and friction Reynolds number (Re_*), direct solutions of the governing equations were used to provide insights into the mean flow drag increase.

Having established a consistent way to estimate the mean flow drag as a function of the Corey shape factor, the dynamics of current-dominated, wave-current boundary layers over hydraulically smooth walls was studied using direct numerical simulations.

For the flat wall, wave-current boundary layer, the mean flow drag did not exhibit any substantial change when compared to the canonical flat wall channel flow. However, the bumpy wall, wave-current boundary layer showed elevated mean flow drag when compared to the canonical flat and bumpy wall channels. Using a turbulent kinetic energy (TKE) and Reynolds stress budget analysis, it was found that there was a decrease in the net TKE production to dissipation rate ratio as a result of the increased TKE dissipation rate. It was also observed that the pressure-strain rate correlations that scramble the TKE across the three diagonal components were comparatively enhanced for the bumpy wall, wave-current case. Consequently, unlike the flat wall, wave-current case, the bumpy wall, wave-current boundary layer exhibits increased mean flow drag.

Finally, using direct numerical simulations of a wave-dominated, wave-current boundary layer over rough walls, it was shown that the simple eddy-viscosity-based drag model proposed by Grant and Madsen (1979), which is meant for the wave-dominated regime, applies because the near-wall flow is three-component-like and isotropic. Additionally, it was observed that the turbulence in the boundary layer responds quickly to the imposed wave-driven mean shear, thus validating the assumption in the eddy-viscosity type models that the turbulence and mean wave-driven shear are in phase. Collectively, these observations validate the use of simple drag models of wave-current boundary layers in large-scale coastal ocean models in the wave-dominated regime. Further work is needed to develop parameterisations for the bottom drag in current-dominated boundary layers.

Acknowledgments

It would be an uphill task to concisely summarise the past three years at Stanford but here is a quick try. I want to thank my advisor, Oliver, for his infinite patience to deal with my incoherent ramblings and discussions [forced!] on the superiority of Scandinavian extreme metal music. But, all jokes aside, over the last three years, I have had the wonderful opportunity to learn everything about computational fluid dynamics [CFD] and much more. I appreciate your attention to detail, teaching me the three laws of CFD, inspiring me through our weekly meetings, and patiently guiding me through the whole process of writing a thesis.

Stephen reinforced my love for ocean waves through his course along with extensive discussions on GM79 and all its glory and failure. Stephen, thank you for continually inspiring me with your scientific acuity and comprehensive knowledge of turbulence literature. I owe a special thanks to Catherine for getting me excited about doing research and teaching. Thank you for being a wonderful mentor and teaching me the importance of a healthy work-life balance. I also want to thank Jeff for introducing me to the wondrous world of stratified turbulence. Your commitment to the EFML community is inspirational and I feel privileged to have had a chance to TA for you.

I would also like to thank Nick for demonstrating the value of precision in scientific discourse and introducing me to the alluring world of turbulence. It has been thoroughly inspiring to take every single one of your courses and gain the numerous insights you have on turbulence physics! Thanks to Leif, Derek, and Justin for

the numerous insightful questions, suggestions, and excitement you brought with you during the EFML seminars. Alex, thanks for your outstanding commitment to enable HPC cluster management at the Huang data center. Also, thanks for teaching me how to generate exceptionally safe passwords and data management techniques.

The EFML has been a constant source of motivation, support, and community during the entirety of my stay at Stanford. My first year at Stanford was extremely difficult both personally and professionally; during this time, Paul, Laura, and Mathilde have been essential sources of inspiration and support. I cannot thank these three [holy trinity!] enough for putting up with my constant questions, discussions, and complaints; you made me feel normal during times of adversity and I will forever be thankful for your support and love. I also want to thank Elisa and Jenny for being ultra-awesome peers as we figured out the PhD journey together. Spending time with you both in Pacifica will always be a highlight of my time at Stanford. An extended thank you to Yuki, Hayoon, Saksham, Ryan, Peiyun, Noah, Margaret, Jennifer, Yenchia, and Hao for everything you all have done for me. Galen, thanks for meeting up with me to discuss waves and currents over zoom despite your busy schedule.

The APS-DFD conference gang of 2022 will always have a special place in my heart; Max, Theo, Mattia, Themis, Nick, and Michael [Wind group]. APS 2022 was honestly the best part of this year and I want to thank you all for being such a never-ending source of joy and laughter. Special thanks to Theo, Mattia, and Themis for the night excursions on the streets of Indianapolis in search of the ultimate "how is it going?" response! Max thanks for your awesome board games initiative and I really hope that this becomes an EFML tradition. Ipshita, Renu, and Udhaya, cheers to the numerous adventures in the woods hiking, camping [more like glamping], and dealing with my abysmal sense of humor.

Outside of the Stanford world, I want to thank my cousin and his family for

their gracious invitation to stay in Chicago during the pandemic. Spending time with Anagha and Siddhant really made it easier to deal with the whole PhD research aspect of life. My elder brother, Prasad, has been a constant source of support and love for the longest time that I can recall. Thanks for always being there for me and supporting my aspirations; be it my failed music career or my aspirations to be a researcher. It would be fitting to say that you were the giant on whose shoulder I have always been standing! I also want to thank my parents for all the sacrifices they have made for me to be where I am today. My friends from Pune; Pooja, Aditya, Aarti, Reshma, Saket, Sanika, and Milind thanks for being such a wonderful bunch to hang out with.

Mruga, thanks for always being there for me despite the distance and countless other hurdles we faced over the past five years. Words cannot begin to describe the joy I feel being married to you. I am looking forward to us spending time together in the Netherlands and finally having the best croissants on the streets of Paris! Everything including this PhD research seemed so easy with you always by my side.

I am grateful for all the funding sources that enabled me to work on this interesting problem, including the SRCC, XSEDE compute grant CTS190063, and National Science Foundation award OCE 1736668.

Contents

List of Tables

List of Figures

Chapter 1

Introduction

Geophysical boundary layer flows over continental shelves are driven by various mechanisms such as waves, tides, density differences, and bottom slope. Such boundary layer flows generally exhibit highly non-linear features, and the relationships take on varying degrees of complexity depending on the type and combination of the driving mechanisms. Most estuaries can be classified based on such driving mechanisms that act over varying time and length scales (Grant and Madsen, 1986; Bosboom and Stive, 2022). One such estuary of interest is San Francisco Bay, the largest estuary on the California coast, comprised of hydrologically and geographically distinct sub-estuaries: Suisun Bay, San Pablo Bay, Central Bay, and South Bay as shown in figure 1.1. The flow in San Francisco Bay is primarily driven by astronomical tidal currents, wind-induced surface-gravity waves, and density differences due to river flows. South Bay experiences strong wind forcing typically during winter storms and summer sea breezes. This leads to strong wave generation that re-suspends much of the sediment, while the tidal currents transport sediments and other passive tracers throughout the Bay. In the South Bay, the flow driven by the northwesterly sea breeze is mainly directed downwind in the shallower shoals and upwind in the main channel (Conomos et al., 1985; Barnard et al., 2013).

In the recent past, nutrient enrichment has degraded many of the world's estuaries, including San Francisco Bay, thus requiring a detailed understanding of the interactions between the various driving mechanisms and the underlying flow within the estuary. Estuarine bottom boundary layers are the interfaces where exchanges of sediment, particles, nutrients, and organisms between the seabed and the overlying water column occur. These complex interactions serve as boundary conditions for large-scale coastal flow models. Thus, engineers and scientists have been using three-dimensional flow models to study and predict the transport and fate of pollutants, sediments, and other passive tracers in such coastal bottom boundary layers (Winterwerp, 2001; Cloern et al., 2020). Predicting the long-term evolution of such dynamically rich estuarine flow systems requires sophisticated numerical models and accurate parameterisations dealing with the multi-physics components involved. Coastal boundary layer flows have received extensive attention analytically and experimentally (Grant and Madsen, 1979; Kemp and Simons, 1982, 1983; Arnskov et al., 1993; Lodahl et al., 1998); and more recently, there have been numerical explorations of estuarine boundary layer flows (Scotti and Piomelli, 2001; Manna et al., 2012, 2015; Nelson and Fringer, 2018). In most experimental investigations, the bottom roughness is characterised using smooth beds or with standard shapes such as triangular, cubical, or spherical arrays. While such roughnesses can yield valuable insights, they introduce additional non-dimensional variables required to describe the flow geometry. The analytical wave-current models, most notably the Grant and Madsen (1979) model, involve several assumptions about the nature of the flow, which may not agree with the actual flow conditions.

Figure 1.1: Satellite view of the San Francisco Bay estuary. Image Source - European Space Agency.

My thesis work aims to use a scale-resolving computational framework to understand the turbulence dynamics over bumpy walls representing naturally rough estuarine boundary layer flows. First, I focus on the effect of roughness characteristics on the mean flow drag by comparing two types of roughness features combined with two flow Reynolds numbers. As the effect of roughness is quantified, I then focus on the dynamics of estuarine bottom boundary layers where the mean current is stronger than the oscillatory wave motion. Lastly, the dynamics of a wave-dominated, wave-current boundary layer are discussed to provide a detailed understanding of the turbulence dynamics and the applicability of reduced-order closures. This chapter provides a literature review essential to understand the results that will be presented in the following chapters. The literature review begins with a brief overview of steady, wave and wave-current boundary layers. This is followed by a short discussion on computational modeling of boundary layer flows that motivates the need to study bumpy wall, wave-current boundary layers.

1.1 Steady turbulent boundary layers

Turbulent channel flows are one of the most widely investigated canonical flow systems. The simple geometry encapsulates rich dynamics making channel flows prime candidates for studying wall-bounded turbulent flows (Eckelmann, 1974; Kim and Moin, 1985). This character has been capitalised to understand the detailed structure of steady, turbulent boundary layers over smooth walls (Krogstad and Antonia, 1994), while steady, turbulent boundary layers over rough walls have also received significant attention (Jiménez, 2004; Schultz and Flack, 2009; Flack and Schultz, 2014; Chung et al., 2021).

Smooth wall, turbulent boundary layers are sufficiently well understood both experimentally and numerically. Townsend (1976) suggests that the only velocity profile that works for smooth walls is the logarithmic law given by

$$\frac{\overline{U}}{u_*} = \frac{1}{\kappa} \ln\left(\frac{x_3 u_*}{\nu}\right) + B, \tag{1.1}$$

where $\overline{U}$ is the average (or mean) velocity, $u_* \equiv \sqrt{\tau/\rho_0}$ is the friction velocity, τ is the bottom stress, ρ_0 is the fluid density, κ is the von Kármán constant for non-stratified, flat-wall flows, x_3 is the vertical coordinate, ν is the kinematic viscosity of the fluid and B is the smooth wall empirical constant which is a weak function of the Reynolds number. Equivalently, the smooth wall empirical constant can be formulated in terms of a roughness height $z_0 = \nu/(9u_*)$. As shown in figure 1.2, the velocity profile shows four distinct regions viz., the linear layer ($x_3^+ < 5$), the buffer layer ($5 \leq x_3^+ < 30$), the log layer ($30 \leq x_3^+ < 180$), and the wake region ($x_3^+ > 180$). It is critical to note that the limits listed for the log layer and the wave region are Reynolds number dependent. The upper limit for the log layer increases with increasing Reynolds numbers as the inertial range increases. Although the linear layer is well understood, a universal, first principles-based model does not exist for

the buffer-layer even though some of the most interesting turbulence physics takes place in this region. The log layer has been the subject of a wide range of studies, and the dynamics within the wake region are generally well understood. In addition to the mean flow predictions, Jiménez and Moin (1991) and Flores and Jiménez (2010) have shown that the near-wall, non-linear turbulent kinetic energy production cycle maintains "healthy turbulence" for wall-bounded flows. The study by Jiménez and Moin provides crucial insights into the statistical flow properties. It elucidates the geometric requirements for "healthy turbulence" in channel flow geometries, also called the "minimal-span" channels. Many other studies have further investigated the flow features over smooth turbulent boundary layers, thus providing a detailed understanding of such flow configurations (Kim and Moin, 1985; Wei and Willmarth, 1989; Moser et al., 1999; Lozano-Durán and Jiménez, 2014).

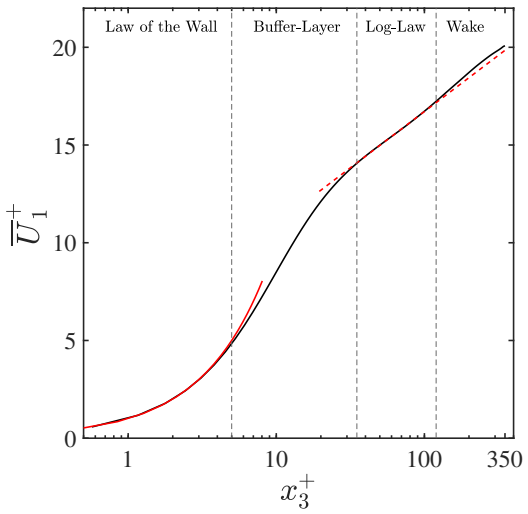

Figure 1.2: Typical velocity profile for a flat-wall turbulent channel flow (black solid line) for $Re_* = 350$. The solid red line marks the linear velocity region while the dashed red line marks the log-law velocity profile as given by equation 1.1 with $B = 5.2$ and $\kappa = 0.4$ (result is from the steady, flat-wall case discussed in Chapter 2).

Despite the prevalence of rough-wall boundary layers in geophysical and industrial flows, a detailed understanding of rough-wall boundary layer flows has been

limited to empirical or experimental investigations. Roughness features introduce other length scales in the flow system, i.e., streamwise (l_{x_1}) and spanwise (l_{x_2}) spacing and roughness height ($\overline{k}_s$), consequently introducing additional non-dimensional parameters such as the non-dimensional streamwise ($l_{x_1}/\overline{k}_s$) and spanwise ($l_{x_2}/\overline{k}_s$) spacing. Similar laws as equation 1.1 were proposed originally by Clauser (1954) and Hama (1954) independently and suggested that the primary effect of roughness was to introduce a downward shift in the log region of the velocity profile, while the overall profile exhibits a similar form as that of the flat wall (see figure 2.1). As a result, one can rewrite equation 1.1 as

$$\frac{\overline{U}}{u_*} = \frac{1}{\kappa} \log\left(\frac{x_3 - \overline{k}_s}{z_0}\right), \tag{1.2}$$

where $z_0 \equiv \overline{k}_s/\alpha_k$ sets the location of the log region of the velocity profile and α_k is the regression parameter that best fits the log region. Townsend (1976) subsequently hypothesised that for sufficient scale separation (i.e., large Reynolds numbers), the turbulence outside the roughness layer is independent of the wall boundary condition except that the wall sets u_*. Similarity arguments for rough walls as presented in equation 1.2 along with Townsend's hypothesis seem to hold for standard roughness types for smooth ($Re_k \lessapprox 4$) and rough ($Re_k \gtrapprox 50$) flow regimes, where the roughness Reynolds number is defined as

$$Re_k = \frac{u_* \overline{k}_s}{\nu}. \tag{1.3}$$

A notable exception has been transitional roughness flow regimes where such scaling arguments have been applied with varying success (Jiménez, 2004; Flack and Schultz, 2014).

Geophysical turbulent boundary layers over natural roughness elements like plants,

urban canopies, seabeds, corals, and other biological roughness elements cannot always be characterised using idealised roughness elements. As a result, most geophysical flows use the concept of equivalent sand grain roughness, first introduced by Nikuradse (1933). Since the regularity of roughness features is an exception for geophysical flows, a canonically similar or representative flow configuration would be that of a gravel-bed channel flow with idealised roughness features, such as that shown in figure 1.3. In this dissertation, hydraulically smooth and rough walls refer to bed characterisations based on the viscous sub-layer and roughness height, unless stated otherwise. As an example, a gravel-bed channel flow can be seen in figure 1.3, which shows the fully rough regime where the roughness height is larger than the viscous sub-layer thickness. The effect of roughness for geophysical flows can be modeled with a shear-stress augmentation originally proposed by Raupach et al. (1991) and further investigated by Miyake et al. (2000), Chow et al. (2005), Lowe et al. (2005), Chou and Fringer (2008), and Chung et al. (2015).

As for the turbulence dynamics of gravel-bed type channel flows, Nikora et al. (2007) introduced the concept of double-averaging, where

$$u(x_i,t) = \overline{u}(x_i) + u'(x_i,t) = \langle\overline{u}\rangle(x_3) + u_r(x_i) + u'(x_i,t), \tag{1.4}$$

where $u(x_i,t)$ is the instantaneous velocity, $\overline{u}(x_i)$ is the time-averaged velocity, $u'(x_i,t)$ is the turbulent velocity, $\langle\overline{u}\rangle(x_3)$ is the time- and planform-averaged velocity, and $u_r(x_i)$ is the dispersive or roughness-induced velocity. An equivalent expression for the shear-stress augmentation (canopy-drag) can be formulated where the roughness-induced velocity is only a function of the vertical coordinate. Mignot et al. (2009) discuss the implications of such a velocity decomposition for gravel-bed channel flows and suggest that the contribution of the double-averaged turbulent kinetic energy (TKE) flux can be locally high such that the double-averaged TKE production is

roughly 75% greater than the dissipation rate at the interface of the laminar viscous sub-layer where the TKE production is maximum. This was validated by Yuan and Piomelli (2014), who observed strong interaction between the roughness sub-layer and the outer layer. The above discussion details the rich flow features observed in channel flow like geometries over smooth and rough walls.

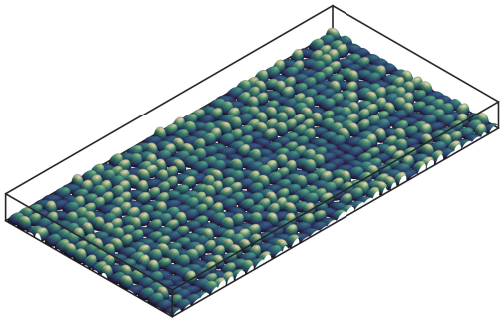

Figure 1.3: An example of a rough-wall channel flow composed of randomly-oriented ellipsoids with properties that can be adjusted to give the desired mean roughness height $\overline{k}_s$. Dark to light colour shading represents distance away from the bottom wall.

1.2 Turbulent wave boundary layers

Turbulent wave boundary layers or oscillatory wave boundary layers (OWBL) have been extensively studied empirically for naturally rough beds and numerically for smooth walls. The central problem of interest for most cases has been to arrive at a formulation of the friction factor (f_w) as a function of the wave Reynolds number

$$Re_w \equiv \frac{A^2\omega}{\nu} \equiv \frac{U_b^2}{\omega\nu}, \tag{1.5}$$

where A is the wave orbital excursion, ω is the wave frequency, and $U_b = A\omega$ is the wave orbital velocity. For non-stratified oscillatory boundary layers, Jonsson (1966)

showed that the friction factor has the functional dependence

$$f_w \equiv \frac{\tau}{\rho_0 U_b^2} = \mathcal{G}\left(Re_w, \frac{A}{\overline{k}_s}\right), \tag{1.6}$$

where $A/\overline{k}_s$ is a measure of the relative roughness. Typically, hydraulically smooth and rough OWBLs can be classified completely based on the wave Reynolds number and the relative roughness as detailed in equation 1.6 (see figure 3.1(a)). The friction factor is typically used to estimate the bed shear stress with

$$\tau = \frac{1}{2} f_w \rho_0 U_b^2. \tag{1.7}$$

Since f_w is not known a priori, a combination of turbulence modeling and/or empirical understanding of f_w is required to accurately prescribe the bed shear stress as a function of the wave Reynolds number and the relative roughness. As detailed in Nielsen (1992), the applicability of eddy-viscosity-based models for estuarine boundary layer flows has been extensively studied both experimentally and numerically. Jensen et al. (1989) carried out experiments for OWBL over hydraulically smooth and rough walls, while Spalart and Baldwin (1987) carried out Direct Numerical Simulations (DNS) over hydraulically smooth walls and found that for increasing $Re_w > 600$, the boundary layer can generate well-developed turbulence for parts of the wave cycle that agree with the velocity scaling laws discussed in equations 1.1 and 1.2. Additionally, for hydraulically smooth walls, the eddy-viscosity can be assumed to be time-invariant, and simple two-equation closure models for turbulent flows can be used to estimate the mean turbulence properties (Spalart and Baldwin, 1987).

For rough walls, Sleath (1987) detailed the essential characteristics of rough-wall OWBL based on the relative roughness ($A/\overline{k}_s$). Sleath found substantial variability in the turbulent intensity as a function of the wave phase and that the wave shear is in phase with the turbulent intensity. As opposed to the hydraulically smooth

wall findings of Spalart and Baldwin (1987), for rough wall OWBLs, Sleath observed considerable variations in the eddy-viscosity profiles, suggesting that analytical and numerical models that assume a time-invariant eddy-viscosity may incorrectly predict the evolution of the bed shear-stress over rough walls. Additionally, Jensen et al. (1989) observed a marked change in the turbulent intensities for OWBLs with the introduction of roughness elements. Ghodke and Apte (2017) studied the energetics of OWBLs over hexagonally packaged spheres in transitionally and very-rough, turbulent regimes by varying the relative roughness parameter. They observed that the flow undergoes a cascade short-circuiting where the mean kinetic energy (MKE) works against the pressure drag, thereby converting MKE to wake kinetic energy (WKE) associated with the roughness elements. They also observed decreased anisotropy during parts of the wave phase, implying the breakup of horse-shoe-type coherent structures and the re-distribution of energy from the streamwise component to the other two components. It is critical to note that the studies mentioned in this discussion employed regular roughness (except Jensen et al., 1989) to represent hydraulically rough walls. As a result, these findings are sensitive to a large number of parameters such as the spacing between the roughness elements in the spanwise and streamwise directions, the type of roughness shape used to generate the rough bed to name a few, consequently requiring further investigation.

1.3 Turbulent, wave-current boundary layers

Most of what is known about turbulent, wave-current boundary layers (WCBL) is based on in-situ measurements or experimental investigations. In estuarine flows, waves rarely exist in isolation and are almost always accompanied by steady currents, giving rise to a dynamically rich flow system. A general functional dependence of the wave-current friction factor ($f_{w,c}$) can be formulated as

$$f_{w,c} \equiv \frac{\tau}{\rho_0 U_b^2} = \mathcal{G}\left(\frac{U_c}{U_b}, \frac{H}{\overline{k}_s}, \frac{U_b}{\omega \overline{k}_s}, \frac{U_b \overline{k}_s}{\nu}\right), \tag{1.8}$$

where the parameters on the R.H.S are the flow dominance parameter (U_c/U_b), U_c is the representative velocity corresponding to the steady current, relative roughness ($H/\overline{k}_s$), H is the channel height, Keulegan-Carpenter number ($KC = U_b/(\omega \overline{k}_s)$), and the roughness Reynolds number based on the wave orbital velocity (Re_k^b). Note that the reference velocity used here is the wave orbital velocity, although equation 1.8 can be recast using U_c to define a friction factor functional dependence as detailed in Chapter 3. It is important to note that while most numerical models use the drag coefficient (C_d), it can be used interchangeably with the friction factor as their definitions are identical. For a hydraulically smooth wall WCBL with moderate friction Reynolds numbers, Lodahl et al. (1998) extensively studied the variation of shear stress as a function of increasing Re_w for wave-dominated flow regimes, i.e., $U_b/U_c > 1$. They observed that as the pulsating flow transitions from a current-dominated to a wave-dominated regime, the flow undergoes a non-monotonic bottom stress reduction with increasing wave strength, as seen in figure 1.4. As explained by Lodahl et al., this decreased drag or re-laminarisation behaviour is caused by attenuation of the vertical turbulent fluxes by the waves. This hypothesis was subsequently validated by Scotti and Piomelli (2001), followed by extensive numerical investigations by Manna et al. (2012, 2015) and Nelson and Fringer (2018) using DNS.

Lodahl et al. suggest that for $Re_w > 1.5 \times 10^5$ with smooth walls, the turbulence due to the steady flow component interacts with the unsteady component of the flow. As a result, regardless of the current-free state of the oscillatory component (laminar or turbulent), the WCBL always transitions to a turbulent state, thereby enhancing the vertical turbulent fluxes. This enables the momentum-rich, high-speed fluid to be transported closer to the wall, thus increasing the time-averaged wall shear stress.

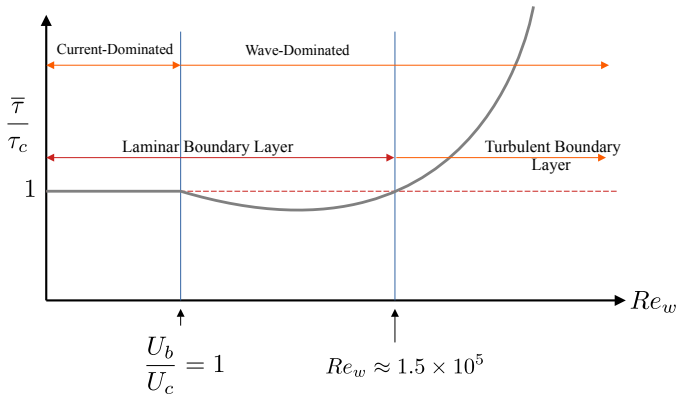

Figure 1.4: Mean wall shear stress as a function of wave Reynolds number for a pulsating, turbulent boundary layer flow over smooth walls. $\overline{\tau}$ is the time-averaged bottom stress, and τ_c is the bottom stress for the steady component of the flow (adapted from Lodahl et al., 1998).

It is important to note that the experimental setup used by Lodahl et al. (1998) corresponds to a wave that has an infinite wavelength. As a result, the wave-current flow is not subject to wave-strain-related effects. Consequently, the total stress is composed of just the viscous shear and Reynolds stress, as the wave stress is zero by definition.

A more geophysically relevant case is the enhancement of the mean stress in the wave-dominated regime over bumpy walls as observed in San Francisco Bay (Bricker et al., 2005; Egan et al., 2019). Analytically, the Grant and Madsen (1979) wave-current model is the most widely accepted theory for WCBLs over rough walls. Grant and Madsen suggest that the time-averaged velocity experiences increased flow drag due to the addition of a wave to a turbulent current over bumpy walls. Using this hypothesis, Grant and Madsen proposed a quadratic drag parameterisation for $f_{w,c}$ as a function of the relevant non-dimensional parameters (see equation 1.8). Since the model employs a time-invariant eddy-viscosity model, it is only applicable to fully-developed turbulent flow conditions (typically $Re_w > 1.5 \times 10^5$ for WCBLs).

Consequently, one of the key results from Grant and Madsen (1979) in which the flow experiences enhanced roughness for wave-dominated regimes is consistent with the process-based interpretation provided by Lodahl et al. for smooth wall WCBL. While the Grant and Madsen model seems to hold for varying flow conditions (Kemp and Simons, 1982, 1983; Soulsby et al., 1993; Arnskov et al., 1993; Barman et al., 2019), studies by Sleath (1987) and recent in-situ measurements in San Francisco Bay by Cowherd et al. (2021) have found that the eddy-viscosity is not time-invariant. These studies also found that the instantaneous boundary layer response assumed in Grant and Madsen may not hold. For small values of $A/\overline{k}_s$ where the roughness height is relatively large compared to the wave excursion, the friction factor comparison may not agree with the Grant and Madsen (1979) predictions as detailed in Yu et al. (2022). Additionally, for rough-wall flows such as those found over coral reefs, extensive work has been done to show that Grant and Madsen (1979) can lead to varying predictions of the location of the log-law region (Bricker et al., 2005; Rogers et al., 2018; Davis et al., 2021) because the form drag contributions increase when $A/\overline{k}_s << 1$ (Schlichting and Gersten, 2003; Rogers et al., 2018). These studies reinvigorate the need to understand WCBLs using numerical and experimental approaches.

The above discussion describes that while there is a substantial understanding of WCBLs over flat or hydraulically smooth walls, their rough wall counterparts seem to be relatively less understood. This is especially true in terms of numerical investigations using the DNS framework, with the exception of Bhaganagar (2008) and Jelly et al. (2020), in which they studied the effect of roughness for varying wave-frequency regimes. They suggest that flow experiences enhanced shear stress for high forcing frequency followed by decreasing shear enhancement with increasing forcing frequency. Jelly et al. observed a significant contribution of the pressure drag for the wave-current cases in the high-frequency forcing regime. The deficiency in a thorough understanding of wave-current interactions over hydraulically smooth and

transitionally-rough walls is the central motivation for this dissertation.

1.4 Computational modelling of turbulent boundary layers

Our understanding of steady and unsteady turbulent boundary layer flows has been significantly improved with numerical modelling. Moin and Kim (1982) used a large-eddy simulation (LES) framework to show the efficacy of simulating turbulent boundary layer flows, capturing the essential flow features in channel flow configurations. This pioneering work was followed by Kim and Moin (1985), who studied channel flow using a DNS framework to validate the basic scaling arguments presented in Section 1.1. Jiménez and Moin (1991) introduced the concept of "minimal-span" channel flows to detail the essential dynamics of wall-bounded non-linear production-dissipation cycles that sustain "healthy" turbulence. The idea of "minimal-span" channels aims to minimise the computational cost to study the boundary layer dynamics by reducing the size of the computational domain. Spalart and Baldwin (1987) studied OWBLs using the minimal-span channel concept and showed the validity of the time-invariant eddy viscosity and two-equation models when compared to experiments and DNS simulations. For wall-bounded flows using full-span channels to resolve the requisite flow features, Flores and Jiménez (2010) and Lozano-Durán and Jiménez (2014) recommend $L_{x_1} \geq 2\pi H$ and $L_{x_2} \geq \pi H$, where L_{x_1} is the streamwise channel length, L_{x_2} is the spanwise channel length, and H is the channel half height. A wide variety of steady and unsteady wall-bounded flows have been investigated using the LES and DNS frameworks for smooth walls (Scotti and Piomelli, 2001; Manna et al., 2012, 2015; Lozano-Durán and Bae, 2016, 2019). However, rough walls have not received such detailed attention.

Recently, there has been renewed interest in simulating rough-wall, turbulent boundary layer flows using the DNS framework. Scotti (2006) proposed a simple immersed boundary method (IBM) to simulate rough walls. Scotti employed randomly orienting ellipsoids to reproduce a rough wall with the roughness height known a priori. This approach has been further validated by Yuan and Piomelli (2014) to provide crucial insights into the effects of roughness. While other more straightforward approaches for modelling rough walls exist (Miyake et al., 2000; Chow et al., 2005; Flores and Jiménez, 2010), these methods, such as shear-stress augmentation, cannot be applied without a-priori knowledge of the drag coefficient (C_d). The IBM approach proposed by Scotti provides a relatively cheap and efficient method to directly simulate rough walls.

Many coastal flow models, such as SUNTANS (Fringer et al., 2006), Delft-3D (Deltares, 2010), and SWASH (Zijlema et al., 2011), employ standard two-equation turbulence models based on the wave-current interaction models primarily proposed by Grant and Madsen (1979). However, as discussed in Section 1.3, such simple models may not always yield the predicted results. Additionally, most coastal flow models employ simpler parameterisations to predict the long-term flow evolution, sediment transport, and pollutant scalar transport. Consequently, improving the reliability of the underlying parametric models can significantly improve the predictive capabilities of coastal flow models. Since the DNS framework is not feasible for large-scale estuarine flow domains, the development of reduced-order models allows studying estuarine flows over a wide range of flow parameters that are generally of interest to engineers. Thus, in this dissertation, the DNS framework will be used to facilitate the development of reduced-order models and assess the applicability of rough-wall models like those used by Spalart and Baldwin (1987), Winterwerp (2001), and Chou and Fringer (2008).

1.5 Dissertation overview

This dissertation is aimed at understanding the turbulence dynamics of wave-current boundary layer flows using DNS. While much is understood about these flows based on experimental and in-situ observational methods, there has been a substantial gap in the literature concerning the dynamics of wave-current interactions over bumpy walls, particularly using numerical simulations. To this end, my work aims to connect the mean flow drag to the properties of the roughness, which will be the focus of the second chapter. In this chapter, I discuss a method to characterise the bumpy wall and discuss the effects of changing roughness characteristics on the mean flow drag. Having established the effect of roughness characteristics, in Chapters 3 and 4 I study wave-current boundary layer dynamics in weak and strong wave flow conditions over bumpy walls. These Chapters provide fundamental insights into the validity of simple drag parameterisations that are used in large-scale coastal ocean models. Chapters 2, 3, and 4 include introductory and computational methods that may seem repetitive because each is written as a standalone manuscript that has been published or submitted to a peer-reviewed journal.

Chapter 2

Effect of roughness characterisation on the mean flow drag in a channel flow[1]

2.1 Abstract

Turbulent flows over bumpy walls are ubiquitous and pose a fundamental challenge to various engineering applications such as coastal boundary layers, drag on ships, hydraulic conveyance networks, and bluff body aerodynamics to name a few. In this study, we use direct numerical simulations (DNS) along with a direct-forcing immersed boundary method (IBM) to understand the connection between the roughness geometry and the mean flow drag. A bumpy wall is constructed using an array of randomly oriented ellipsoids characterised by the Corey shape factor (C_o). We find that our results exactly validate the experimental studies by Nikuradse (1933) for sand-grain type roughness ($C_o = 1.0$). Additionally, we observe that the mean flow drag increases for decreasing C_o through an increase in the form-drag contribution and a decrease in the viscous drag. We also develop a relationship between the statistics of the bottom height distribution and the roughness parameter (z_0) that

[1]A version of this chapter was submitted to the Journal of Hydraulic Engineering as "Effect of roughness characterisation on the mean flow drag in a channel flow", by Patil and Fringer.

may help explain the spread observed in the drag coefficient predicted when using conventional tools such as the Moody diagram.

2.2 Introduction

Turbulent boundary layers over rough walls are of significant interest to a variety of disciplines ranging from the aviation industry (Spalart and Mclean, 2011), shipping industry (Murphy et al., 2018), hydraulic conveyance networks (Moody, 1944), and estuarine/coastal modeling (Grant and Madsen, 1986), to name a few. A thorough review of recent advances in characterisation of the flow drag over rough walls is presented by Chung et al. (2021). They showed a large uncertainty of roughly $\pm 11\%$ still exists in most engineering applications of flow drag prediction. While the absolute magnitude of the uncertainty may not seem substantial, the same study suggests that these uncertainties have an expected cost of the order of billions of US dollars annually for naval applications (Chung et al., 2021). Consequently, understanding the uncertainty around the flow drag is a fruitful endeavour not only from a fundamental turbulence physics standpoint but from an engineering application perspective. Thus, a central question has aimed at specifying the flow drag as a function of the properties of the underlying roughness features.

Canonical flat-wall channel flows have been extensively studied as they encapsulate rich turbulence dynamics that support a wide range of applications (Kim et al., 1987; Tamburrino and Gulliver, 1999; López and García, 1999; Lozano-Durán et al., 2012). These studies have validated the analytical predictions of the time-averaged velocity profile close to the wall (i.e., the law of the wall) and away from the wall (i.e. the log-law) as shown in figure 2.1. For canonical flat-wall channel flows, the time-averaged velocity profile close to the wall obeys the law of the wall in that the velocity is linearly dependent on the distance from the wall (von Kármán, 1930). This region is

followed by the buffer layer that does not have a universal first principles-based model, even though most of the turbulence production occurs within this region (Pope, 2000). Townsend (1976) suggests that in the region above the buffer layer, the time-averaged velocity profile is given by

$$\frac{\overline{U}}{u_*} = \frac{1}{\kappa} \ln\left(\frac{x_3 u_*}{\nu}\right) + B, \tag{2.1}$$

where $u_* \equiv \sqrt{\tau/\rho_0}$ is the friction velocity, τ is the bottom stress, ρ_0 is the fluid density, κ is the von Kármán constant, ν is the kinematic viscosity of the fluid, and $B \approx 5.2$ is an empirical constant which is a weak function of the Reynolds number. This region is called the log-law region and has been the subject of a wide range of studies as previously mentioned. As for the wake region above the log-law, there is some empirical understanding (Pope, 2000) although this region has received less attention than the others.

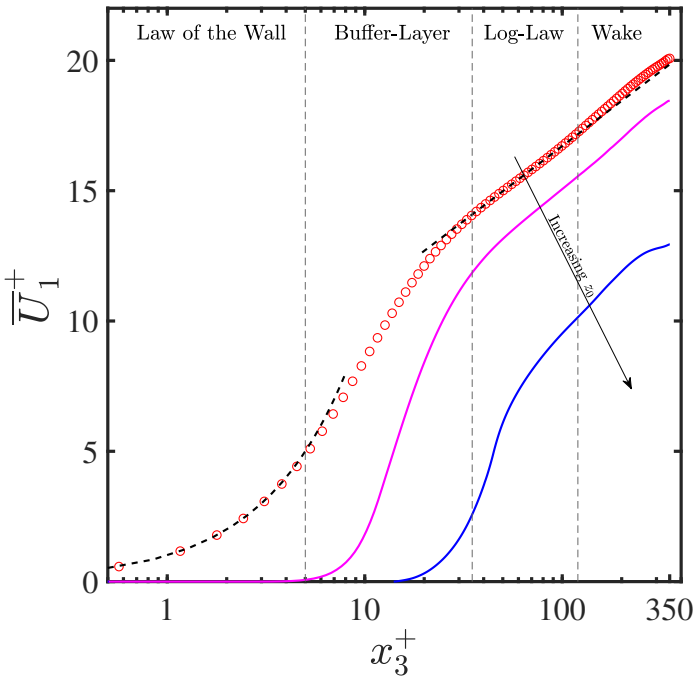

Figure 2.1: Time-averaged velocity profiles for three cases with varying wall boundary conditions. The red markers correspond to canonical flat-wall channel flow, the magenta line corresponds to a bumpy-wall channel with hydraulically-smooth wall conditions, and the blue line corresponds to a bumpy-wall channel with hydraulically-transitional wall conditions. The text at the top of the figure marks the various regions in the canonical flat-wall channel case. Note that these cases have identical friction Reynolds numbers (i.e. $Re_* \equiv u_* H/\nu = 350$).

While flat-wall channels are relatively well understood, bumpy-wall channel flows have so far evaded such a universal understanding. The primary challenge has been to universally connect the roughness characteristics to the time-averaged velocity profile and bottom stress. Clauser (1954) and Hama (1954) independently proposed that roughness acts to shift the log-law region downward when compared to the flat-wall channel cases as shown in figure 2.1. Consequently, the log-law velocity takes on the form

$$\frac{\overline{U}}{u_*} = \frac{1}{\kappa} \log\left(\frac{x_3 - \overline{k}_s}{z_0}\right), \tag{2.2}$$

where $\overline{k}_s$ is the mean physical roughness height, $z_0 \equiv \overline{k}_s/\alpha_k$ is the reference height that sets the location of the log-law, and α_k is a regression parameter that best fits the log-law. Townsend (1976) hypothesised that for sufficient scale separation (i.e., large Reynolds number), the turbulence within the log-law region is self-similar and that the wall boundary conditions set z_0. Nikuradse (1933) in his seminal work suggested that for sand-grain type roughness and large Reynolds numbers, the reference height for bumpy walls is $z_0 = \overline{k}_s/30$. Following the work by Nikuradse (1933), many studies have focused on characterising non-sand-grain type rough walls, based on bulk statistics such as higher moments of the probability distribution of the roughness heights (Thakkar et al., 2017), regularly spaced identical roughness elements (Volino et al., 2011; Schultz and Flack, 2009), and randomly oriented ellipsoidal roughness elements (Yuan and Piomelli, 2014). Owing to the large number of non-dimensional parameters needed to characterise the rough wall, most of the literature suggests a lack of universal scaling for the velocity shift in the transitionally rough flow regime. Thakkar et al. (2017) showed that the roughness characteristics such as the root-mean-squared roughness height can be used to characterise the peak turbulent kinetic energy for rough walls typically used in industrial applications. In geophysically relevant flows, Scotti (2006) validated a novel direct forcing immersed boundary method (IBM) with experimental results and observed that the turbulent statistics along with the dissipation characteristics can be accurately predicted. Scotti (2006) generated the bumpy wall using a set of randomly oriented ellipsoids thus eliminating the dependence of streamwise and spanwise spacing length scales on the parameters of interest. This method has been further validated to understand the turbulent kinetic energy and Reynolds stress budgets in boundary layers (Yuan and Piomelli, 2014, 2015).

The discussion presented in Scotti (2006) suggests that the bumpy wall generated using randomly oriented ellipsoids has a prescribed set of semi-axes lengths for the individual roughness elements. Using these lengths, we can define the Corey shape

factor as (Corey, 1949)

$$C_o = \frac{\alpha k_s}{\sqrt{(\beta k_s)(\gamma k_s)}} = \frac{\alpha}{\sqrt{\beta\gamma}}, \tag{2.3}$$

where k_s is the mean roughness height, α, β, and γ are non-zero constants defined such that αk_s is the minor semi-axis length, βk_s is the major semi-axis length, and γk_s is the intermediate semi-axis length. Based on the shape characterisation defined in equation 2.3, Scotti (2006) prescribes $C_o \approx 0.6$ which is expected to exhibit a mean flow drag that is larger than that for the case with roughness elements with $C_o = 1$ i.e., sand-grain type spherical roughness elements (Corey, 1949; Julien, 2010). The larger mean flow drag occurs due to flow separation as the roughness elements are relatively taller for $C_o = 0.6$ when compared to $C_o = 1.0$, thus increasing the form drag. While the work of Corey (1949) dealt with the drag force on the vertical settling of sedimentary particles, the Corey shape factor can be used to characterise general properties of the roughness. For example, as shown in figure 2.2, for the same mean roughness height ($\overline{k}_s$), the roughness function can be different based on the Corey shape factor (C_o). These observations provide sufficient motivation to investigate the effect of changing C_o on the flow drag as a systematic characterisation of engineering-based roughness features.

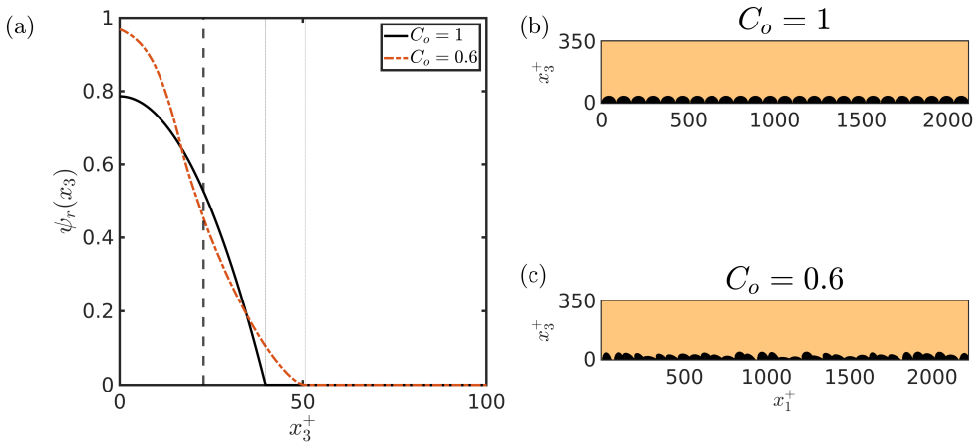

Figure 2.2: (a) Comparison of the area fraction ψ_r as a function of distance from the wall (x_3^+) for identical mean roughness height ($\overline{k}_s$) and different Corey shape factor (C_o). (b) and (c) show the arrangement of individual roughness elements along the streamwise direction of the channel. The non-dimensionalisation is presented using the wall units corresponding to $Re_* = 350$.

In this study, we quantify the effect of changing the Corey shape factor on the flow drag. Direct numerical simulations of a turbulent channel over varying C_o are used to present the first-order statistics and comment on the flow drag. Lower-cost simulations with minimal-span channels are used to estimate the flow drag over a larger number of simulations with different C_o. Lastly, we connect the roughness characteristics to the expected mean flow drag and present concluding remarks.

2.3 Problem formulation

2.3.1 Governing equations and computational framework

We simulate a steady channel flow with direct numerical simulation (DNS) in which we solve the incompressible Navier-Stokes equations

$$\partial_t u_i + \partial_j(u_j u_i) = -\frac{1}{\rho_0}\partial_i p + \nu\partial_j\partial_j u_i + \Pi_c\delta_{i1} + F_{\mathrm{IBM}}, \tag{2.4}$$

subject to the continuity equation

$$\partial_i u_i = 0. \tag{2.5}$$

In these equations, t is time, u_i is the velocity vector, x_j is the coordinate vector, ρ_0 is the density of the fluid, p is the pressure, ν is the kinematic viscosity of the fluid, Π_c is the driving pressure gradient, δ_{ij} is the Kronecker delta function, and F_{IBM} is the immersed boundary force used to model the effect of the roughness elements. The coordinate axes x_1, x_2, and x_3 are aligned in the streamwise, spanwise, and vertical directions, respectively. The channel is periodic in the streamwise and spanwise directions, while a no-slip boundary condition is imposed at the bottom wall where the roughness elements are located. The top wall has boundary conditions given by

$$u_3(x_3 = H) = 0, \quad \frac{\partial u_i}{\partial x_3}(x_3 = H) = 0, \quad \forall i \in 1, 2, \tag{2.6}$$

where H is the channel depth.

The governing equations are solved with a second-order accurate, finite-difference spatial discretisation on a staggered grid without any sub-grid scale modeling (i.e., these are direct numerical simulations). The fractional-step method is used along with a third-order accurate Runge-Kutta time-advancing scheme (Orlandi, 2000; Moin and

Verzicco, 2016; Kim and Moin, 1985). A bumpy wall is introduced with a direct forcing immersed boundary method based on the method proposed by Scotti (2006). The bumpy wall is generated by placing randomly oriented ellipsoids with fixed semi-axes such that the mean roughness height can be estimated a priori through the roughness function, which is the area fraction as a function of height, as shown in figure 2.2. Additional details of the computational framework can be found in Patil and Fringer (2022). As shown by Jiménez and Moin (1991) and Flores and Jiménez (2010), the near-wall, non-linear turbulent kinetic energy production cycle maintains "healthy turbulence" for wall-bounded flows. The study by Jiménez and Moin (1991) provides crucial insights into the statistical flow properties and elucidates the geometric requirements for "healthy turbulence" in channel flow geometries, also called minimal-span channels. This concept of the minimal-span channel has been subsequently used to understand the mean flow drag without resolving the entire velocity profile (Chung et al., 2015; MacDonald et al., 2017). As the name indicates, the minimal-span channels limit the domain size in the spanwise direction such that the flow domain resolves the minimal dynamics (i.e., the interaction of two streamwise streaks) required to correctly resolve the near-wall region that is responsible for most of the turbulence production (Jiménez and Moin, 1991; Flores and Jiménez, 2010; Pope, 2000). As a result, by correctly tuning the domain size in the spanwise direction, the mean velocity profile can be resolved adequately up to $x_3^+ \equiv x_3 u_*/\nu \approx 160$ (Jiménez and Moin, 1991; Flores and Jiménez, 2010; Chung et al., 2015; MacDonald et al., 2017).

2.3.2 Simulation parameters

We define the drag coefficient as

$$C_d = \frac{u_*^2}{U^2}, \tag{2.7}$$

where $u_* \equiv \sqrt{\tau/\rho_0}$ is the friction velocity, τ is the time-averaged bottom stress averaged over the bottom boundary, and U is the domain-integrated and time-averaged streamwise velocity. The friction velocity is fixed by choosing the driving pressure gradient $\Pi_c = u_*^2/H$ which in turn ensures that the bottom stress is given by $\tau = \rho_0 u_*^2$. As a result, since u_* is fixed, the drag coefficient changes due to changes in U. In this problem, there are seven relevant parameters, viz., the bottom stress (τ/ρ_0), velocity (U), channel depth (H), kinematic viscosity of the fluid (ν), and the three semi-axes lengths of the ellipsoid ($\alpha\overline{k}_s$, $\beta\overline{k}_s$, and $\gamma\overline{k}_s$). Additionally, there are two rotation angles (uniformly distributed) that are required to define the Euler angle rotations of the ellipsoids. However, as there are a relatively large number of roughness elements, it is assumed that the effect of sampling the rotation angles is not substantial as shown in Yuan and Piomelli (2014). Thus, using the Buckingham-pi theorem, the drag coefficient can be shown to have the functional dependence

$$C_d \equiv \frac{\tau}{\rho_0 U^2} \equiv \left(\frac{u_*}{U}\right)^2 = \mathcal{G}\left(Re, C_o, \frac{H}{\overline{k}_s}, S_p\right), \tag{2.8}$$

where $Re \equiv UH/\nu$ is the Reynolds number, C_o is the Corey shape factor defined in equation 2.3, $H/\overline{k}_s$ is the blocking factor, and $S_p \equiv (\alpha\beta/\gamma^2)^{1/3}$ is the sphericity of the ellipsoids. In equation 2.8, the last three terms on the right-hand side of the equation depend on the statistical properties of the bed. Therefore, rather than conduct an exhaustive study of the effects of the bed parameters, we focus on the effects of C_o while holding $H/\overline{k}_s$ fixed, and then relate the effective bottom roughness to the statistical properties of the bed. The sphericity (S_p) is not held constant although we minimize its effects by ensuring $S_p \geq 0.84$.

To understand the effect of C_o, we choose friction Reynolds numbers 350 and

700, fix $H/\overline{k}_s = 13.15$ and run a set of full-span simulations along with a series of minimal-span channel flows to extend the range of C_o while limiting the computational cost. To directly compare the flat wall cases to the bumpy wall cases, Jiménez (2004) recommend $H/\overline{k}_s > 40$, such that the change in the effective depth does not significantly affect the comparison. However, as all the bumpy wall cases have identical values of $H/\overline{k}_s$, they can be compared directly. Note that $\langle\cdot\rangle^+ \equiv \langle\cdot\rangle u_*/\nu$ indicates non-dimensionalisation using wall units unless specified otherwise. As shown in Table 2.1, we run a set of 13 simulations to understand the effect of changing C_o and Re_* on the mean flow drag.

The full-span channels have dimensions $2\pi H \times \pi H \times H$ and are discretised using $768 \times 512 \times 256$ grid points in the streamwise, spanwise, and vertical directions, respectively. Uniform grid spacing is used to resolve the roughness region beyond which hyperbolic tangent grid stretching is used. For $Re_* = 700$, this gives $\Delta x_1^+ = 5.73$, $\Delta x_2^+ = 4.30$, and $\Delta x_{3,\mathrm{min}}^+ = 0.66$ over the roughness region and $\Delta x_{3,\mathrm{max}}^+ = 10.0$ at the top of the channel. The dimensions of the minimal-span channels are $2\pi H \times 200\Delta x_2^+ \times H$ and discretised using $768 \times 64 \times 256$ grid points in the streamwise, spanwise, and vertical directions, respectively. For all simulations, a time-step size of $\Delta t^+ \equiv u_*^2 \Delta t/\nu = 0.045$ was used, based on a maximum Courant number of 0.4. Note that all bumpy wall simulations correspond to hydraulically transitional flow conditions, i.e., $4 \leq u_*\overline{k}_s/\nu \leq 70$, with $u_*\overline{k}_s/\nu = 26.6$ and $u_*\overline{k}_s/\nu = 53.2$ for $Re_* = 350$ and $Re_* = 700$, respectively.

The channel flow simulations are initialised with a flow field from precursor simulations interpolated and scaled to match the friction Reynolds number. The simulations are run for a total of 15 eddy-turnover times ($T_\epsilon = H/u_*$) with an initial transient of $10T_\epsilon$. Time-averaged statistics discussed in this paper are averaged over the last $5T_\epsilon$ unless otherwise specified. The flow is said to be statistically converged when the

total stress profile above the roughness elements follows the linear stress profile as discussed in Patil and Fringer (2022). The full-span channels are run on 256 CPUs and require about $276,500$ wall-clock hours to simulate a total of 15 eddy-turnover times. The minimal-span channels are run on 32 CPUs and require $7,700$ wall-clock hours to simulate a total of 15 eddy-turnover times, reflecting savings in computational cost by a factor of 36 when compared to the full-span simulations.

Case Name	**Description**	$\mathbf{Re_*}$	$\mathbf{C_o}$	$\mathbf{S_p}$
CF	Flat wall, full-span channel	350	-	-
C350C1	Bumpy wall, full-span channel	350	1.0	1.000
C350C06	Bumpy wall, full-span channel	350	0.6	0.94
C700C1	Bumpy wall, full-span channel	700	1.0	1.000
C700C06	Bumpy wall, full-span channel	700	0.6	0.94
MC350C1	Bumpy wall, minimal-span channel	350	1.0	1.000
MC350C08	Bumpy wall, minimal-span channel	350	0.8	0.97
MC350C06	Bumpy wall, minimal-span channel	350	0.6	0.94
MC350C04	Bumpy wall, minimal-span channel	350	0.4	0.84
MC700C1	Bumpy wall, minimal-span channel	350	1.0	1.000
MC700C08	Bumpy wall, minimal-span channel	350	0.8	0.97
MC700C06	Bumpy wall, minimal-span channel	350	0.6	0.94
MC700C04	Bumpy wall, minimal-span channel	350	0.4	0.84

Table 2.1: Simulations carried out in this study, where the first C⟨num⟩ corresponds to the friction Reynolds number, and the following C⟨num⟩ stands for the Corey shape factor. Thus, case C350C1 corresponds to a channel with a friction Reynolds number of 350 and a Corey shape factor of 1. All simulations have $H/\overline{k}_s = 13.15$. Case names starting with the letter M correspond to the minimal-span channel simulations.

2.4 Results

2.4.1 Mean and root-mean-squared velocity profiles

Changing the parameters and their impact on the mean flow drag can be inferred by observing the location of the log-law region in the time- and planform-averaged velocity profiles. Figure 2.3(a) shows a comparison of the time- and planform-averaged streamwise velocity for the full-span channel flow cases. Comparing the velocity profiles to the canonical flat-wall channel case (CF), the presence of roughness decreases the mean flow U and thus increases the bottom drag coefficient for the bumpy wall cases. The bumpy wall, log-law is given by equation 2.2, where Nikuradse (1933) found that $z_0 = \overline{k}_s/30$ for sand-grain type roughness (i.e., $C_o = 1.0$). As shown in figure 2.3, the red dashed line corresponds to the log-law estimate given by equation 2.2 and the Nikuradse (1933) estimate for z_0. Case C350C1 exactly matches this prediction and, more importantly, z_0 is not regressed unlike the other cases (i.e. $C_o = 0.6$). The mean flow drag for case C700C1 is larger when compared to case C350C1, as the drag increases with increasing Re_*. A similar observation can be made when case C700C06 is compared to case C350C06. The full-span channel results suggest that there is a consistent increase in the mean flow drag when decreasing C_o for the two Re_* considered.

To further understand the effect of C_o on the mean flow drag, we validated the use of minimal-span channels (Jiménez and Moin, 1991; Chung et al., 2015; MacDonald et al., 2017). As seen in figure 2.3(a), as the spanwise domain is restricted to incorporate the interaction of just two streamwise streaks, the velocity profiles in the minimal-span channels match the full-span counterparts for $x_3^+ \lesssim 160$, beyond which the profiles deviate from the log law. Therefore, because minimal-span channels accurately capture the near-wall velocity profiles, we used the minimal-span channels to extend the range of C_o without imposing a large computational cost that would

be required for the full-span channel cases.

In addition to the mean velocity profiles, there are distinct changes observed in the root-mean-squared (rms) velocity profiles as shown in figure 2.3(b). First, for cases with $C_o = 0.6$, there is a strong decrease in the rms velocity components when compared to the case with $C_o = 1.0$ in the near-wall region. Further away from the wall, cases with $C_o = 0.6$ are identical to those with $C_o = 1.0$, further confirming the de-coupled nature of the near-wall and outer regions of the flow (Townsend, 1976). Similar mean flow response for the two Reynolds numbers suggests that the effect of C_o is to modify the wall boundary condition such that decreasing values of C_o result in a larger effective z_0. As for the Reynolds and viscous stress profiles, most of the variations occur in the vicinity of the roughness elements. For the viscous stress, there is a prominent decrease in the maximum value with decreasing C_o. Additionally, as the friction Reynolds number increases, the relative contribution of the viscous stress decreases. These changes in the viscous stress profiles support the hypothesis that the stress contribution due to flow separation is expected to increase at the expense of the viscous stress for decreasing C_o (discussed later). The Reynolds stress profiles, on the other hand, are independent of C_o and follow the linear stress (blue dashed line) profile as expected.

2.4.2 Drag coefficient

To compare the drag coefficient for the full- and minimal-span channels, we define the drag coefficient

$$C_d^r = \left(\frac{u_*}{U_r}\right)^2, \tag{2.9}$$

where U_r represents the time- and planform-averaged streamwise velocity evaluated at $x_3^+ = 120$. This definition of the drag coefficient allows for comparison of the full-

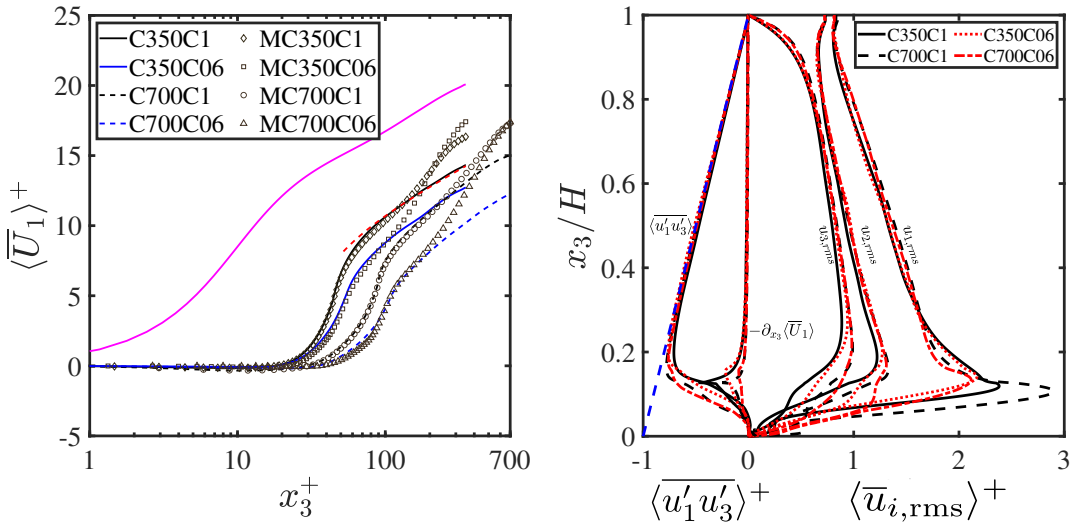

Figure 2.3: (a) Comparison of time- and planform-averaged velocity profiles for the full-span channel flow cases (lines) and minimal-span channel flow cases (markers). The magenta solid line marks the canonical channel flow case with $Re_* = 350$. The red dashed line marks the location of the log-law fit where $z_0 = \overline{k}_s/30$ as suggested by Nikuradse (1933). For clarity, the time- and planform-averaged velocity profiles for cases MC350C08, MC350C04, MC700C08, and MC700C04 are not shown. (b) Comparison of the root-mean-squared (rms) velocity profiles for the full-span channels (right of the zero mark on the x-axis) and the Reynolds and viscous stresses (left of the zero mark on the x-axis). The blue dashed line marks the total linear stress profile expected for channel flow cases.

and minimal-span channels for cases where the full log-law velocity profile may not be available. Such a definition of the drag coefficient is quite common, especially in field experiments where only point measurements may be available (e.g. Egan et al., 2019). Figure 2.4 shows a comparison of the drag coefficient for all cases detailed in Table 2.1. The overall trend is that with decreasing value of C_o there is an increase in the drag coefficient for the two friction Reynolds numbers considered. Additionally, the drag coefficient predicted using the minimal-span channels is consistent with the full-span channels providing further impetus to utilise the concept of minimal-span channels to predict the mean flow drag (Chung et al., 2015; MacDonald et al., 2017). For $Re_* = 350$, the drag coefficient increases as C_o decreases until about $C_o = 0.6$, beyond which C_d^r saturates and starts to decrease slightly. However, for $Re_* = 700$, a monotonic increase in the drag coefficient is observed with decreasing C_o. Because the estimate of C_d^r is sensitive to z_{ref}, C_d^r seems to saturate for $Re_* = 350$ but increases monotonically for $Re_* = 700$. Although it is unclear why case MC350C04 appears to be an outlier in the overall trend, it is omitted in the following analysis. C_d^r is more sensitive to C_o for higher Re_*, which is a result of the higher contribution of the form drag at higher Re_*, as discussed later.

Another way to understand the effect of changing the geometry of the bumps is through changes in the roughness parameter z_0 as shown in figure 2.5. For the full-span cases, z_0 can be regressed to best fit the log law (equation 2.2) because the log-law region is well resolved. This is evident in figure 2.3 which shows that the minimal-span channels reproduce the full-span velocity profiles. However, for the cases without companion full-span channels ($C_o = 0.4, 0.8$), the lack of a significant log law region does not allow such a regression to compute z_0. Consequently, to enable consistent comparison between the full- and minimal-span channels, z_0^r is inferred from the log law at a reference height of $z_{\text{ref}} = 120\nu/u_*$, such that

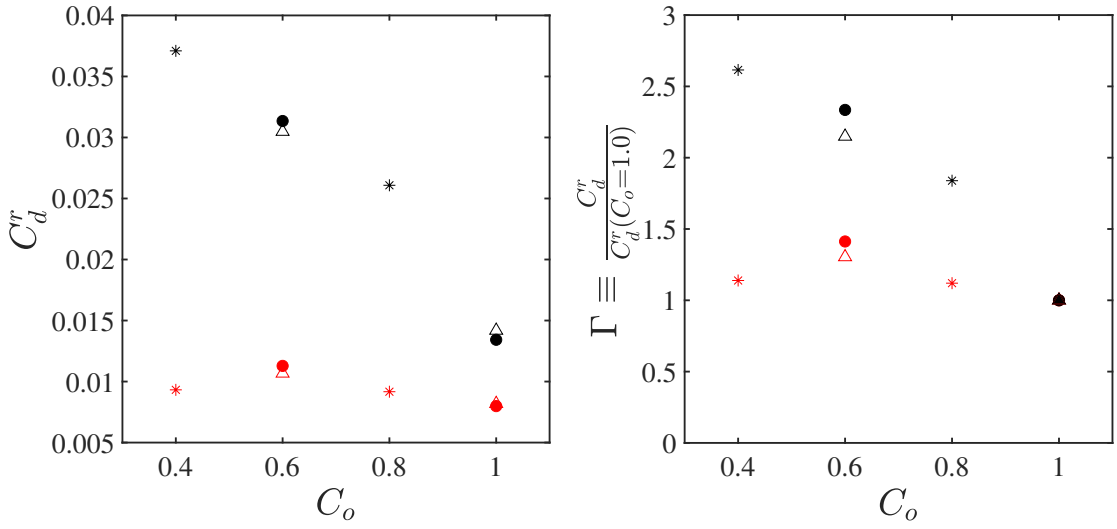

Figure 2.4: (a) Comparison of the drag coefficient for varying values of the Corey shape factor (C_o). Filled data markers correspond to full-span channel cases while empty markers correspond to minimal-span channel cases. Black markers indicate $Re_* = 700$ while red markers indicate $Re_* = 350$. (b) Same data as panel (a), but normalised using the drag coefficient for $C_o = 1$ such that the y-axis represents the relative gain (Γ) of the drag coefficient for decreasing C_o.

$$z_0^r = (z_{\text{ref}} - \overline{k}_s) \exp\left(-\frac{\kappa}{\sqrt{C_D^r}}\right), \tag{2.10}$$

where C_D^r is the drag coefficient defined in equation 2.9. Figure 2.5(a) suggests a similar overall trend as observed from the drag coefficient for changing C_o and Re_*. Additionally, it is clear that for increasing values of C_o, α_k decreases, suggesting that the roughness height z_0^r decreases for increasing C_o.

While these observations provide a consistent way to relate the roughness characteristics, it is often more practical to relate the roughness height z_0^r to statistical properties of the bed height in addition to the mean roughness (bed) height. Indeed, the results in the paper show very clearly that the bottom drag varies significantly through changes in C_o even though $\overline{k}_s$ is constant for all simulations. To relate z_0 to the statistical properties of the bed, we calculate the standard deviation of the bed

height

$$k_s^\sigma = \left[\frac{1}{N}\sum_{i=1}^{N}(k_s^i - \overline{k}_s)^2\right]^{1/2}, \tag{2.11}$$

where k_s^i is the height of each of the ellipsoids and $N \approx 360$ is the number of ellipsoids (N is approximate because the number of ellipsoids that can fit on the bottom wall is subject to the random orientation angles). We then regress the standard deviation to the roughness height with $z_0^r = \chi k_s^\sigma$, where χ is the regression parameter. As shown in figure 2.5(b), good correlation can be observed between k_s^σ and the roughness parameter i.e., z_0^r, where $\chi(Re_* = 700) = 0.188$ and $\chi(Re_* = 350) = 0.112$. Note that for $Re_* = 350$, the data point for $C_o = 0.4$ is not included in the regression as it appears to be an outlier. While it is unclear why this point is an outlier, we expect this to be a consequence of the minimal-span nature of the channel. Using linear regression, we observed $R^2 = 0.891$ for $Re_* = 700$ and $R^2 = 0.765$ for $Re_* = 350$, suggesting a strong correlation between the roughness characteristics and the expected roughness parameter. In addition to the Re_* dependence, the definition of C_o does not account for varying values of the sphericity (S_p) for identical C_o as suggested by Julien (2010). It is clear to see that z_0^r is sensitive to Re_* which can be inferred from the regression parameter. Some of the scatter observed in the data presented here can be attributed to the transitional roughness Reynolds number regime as the flow separation is localised to some roughness elements that penetrate beyond the viscous sublayer as shown in figure 2.6 and discussed in Schultz and Myers (2003) and Flack et al. (2012). These observations may help explain the variability observed in conventional methods to estimate the mean flow drag (e.g. Moody (1944) or the roughness function (ΔU^+) defined in Schultz and Myers (2003)).

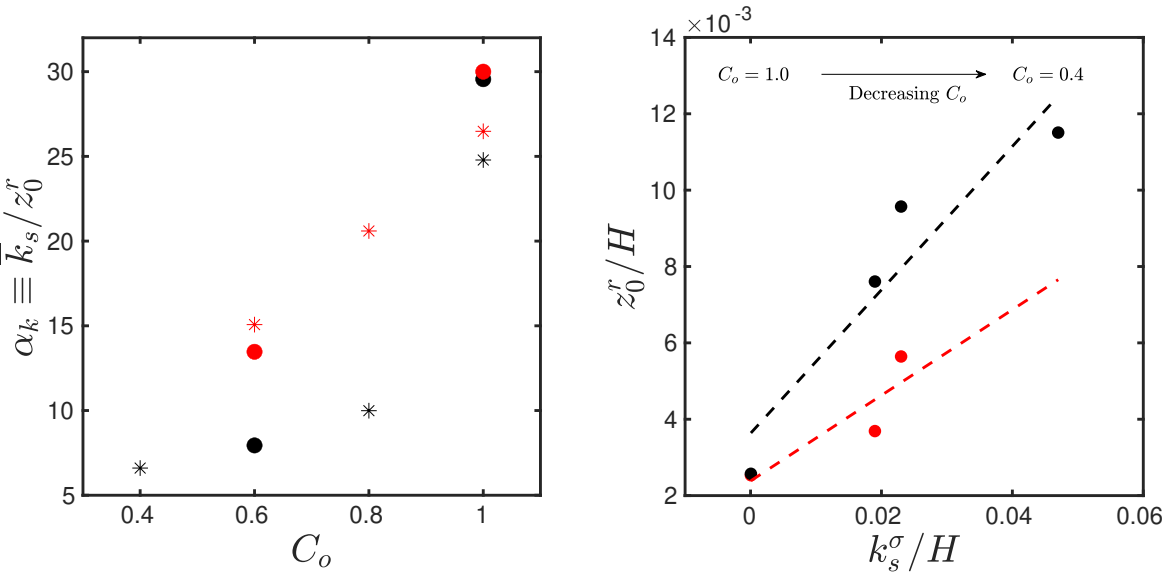

Figure 2.5: (a) Comparison of the effect of changing C_o and Re_* on the roughness parameter z_0^r. (b) Correlation between the standard deviation of the roughness (k_s^σ) and the roughness parameter (z_0^r). Dashed lines mark the linear fit to the data and the markers starting from the left correspond to $C_o = 1.0$, $C_o = 0.8$, $C_o = 0.6$, and $C_o = 0.4$, respectively. Marker colour scheme is identical to figure 2.4.

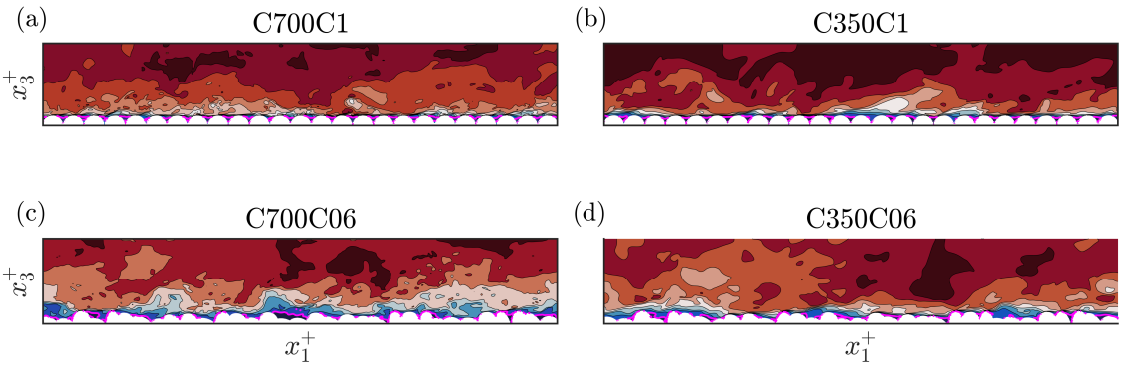

Figure 2.6: Contour plots along the channel centerline at time $t_\epsilon = tu_*/H = 12.0$, showing the instantaneous streamwise velocity normalised by the friction velocity for the four full-span channel cases. The white region marks the roughness elements. Blue colour indicates slower velocities while red colour indicates faster velocities. The solid magenta line marks the contour where $U_1 = 0$, thus regions enclosed by the magenta line correspond to negative streamwise velocity where there is flow separation.

2.4.3 Mean momentum partitioning

Increased mean flow drag with a simultaneous decrease in the viscous stress for decreased C_o suggests that there is a net increase in the form drag components as the flow separates at the crest of the roughness elements. As shown in figure 2.6, there is relatively more flow separation for cases C350C06 and C700C06 when compared to cases C350C1 and C700C1. These observations along with the attenuated viscous stress profiles and increased drag coefficient suggest that the form drag for smaller C_o increases.

Since the immersed boundary force (F_{IBM}) is imposed at every sub-step in the Runge-Kutta time-integration scheme, only the divergence-free velocity at the end of each time step is available (Yuan and Piomelli, 2014, 2015). Therefore, while the IBM force can be used to compare the total drag force on the bed, it does not give the relative contributions of viscous and form drag. To separately compute these components of the drag, we begin with the streamwise momentum equation

$$\partial_t u_1 + \partial_j(u_j u_1) = -\partial_1 P + \nu \partial_j \partial_j u_1 + \Pi_c + F_{\mathrm{IBM}}, \tag{2.12}$$

where $P = p/\rho_0$ is the modified or reduced pressure. Defining $\mathcal{V}_f$ as the volume occupied by the fluid above the roughness elements and integrating equation 2.12 over $\mathcal{V}_f$ gives, after using Gauss' theorem and noting that $F_{\mathrm{IBM}} = 0$ in $\mathcal{V}_f$ and imposing periodicity in the x_1 and x_2 directions and free-slip condition at $x_3 = H$,

$$\partial_t \int_{\mathcal{V}_f} u_1 \, d\mathcal{V} + \int_{\mathcal{A}_\mathrm{B}} u_1(u_j \, e_j) \, d\mathcal{A} = -\int_{\mathcal{A}_\mathrm{B}} P e_1 \, d\mathcal{A} + \nu \int_{\mathcal{A}_\mathrm{B}} e_j \partial_j u_1 \, d\mathcal{A} + \mathcal{V}_f \Pi_c, \tag{2.13}$$

where $\mathcal{A}_\mathrm{B}$ is the control surface at the bumpy wall that corresponds to the top of the roughness elements, and e_j is the unit normal vector pointing outward relative to $\mathcal{V}_f$. After time-averaging equation 2.13, the unsteady term vanishes, thus giving the momentum partitioning

$$\underbrace{\int_{\mathcal{A}_\mathrm{B}} \overline{u_1 u_j} \, e_j \, d\mathcal{A}}_{\text{Advective Term}} + \underbrace{\int_{\mathcal{A}_\mathrm{B}} \overline{P} e_1 \, d\mathcal{A}}_{\text{Form Drag}} - \underbrace{\nu \int_{\mathcal{A}_\mathrm{B}} e_j \partial_j \overline{u}_1 \, d\mathcal{A}}_{\text{Viscous Drag}} = \underbrace{\mathcal{V}_f \Pi_c}_{\text{Driving Force}}, \tag{2.14}$$

where the overbar represents the time average. The advective term on the left-hand side is non-zero because the IBM method imposes a force that produces a vanishing cell-centered velocity component, and a small, non-zero face-centered component, where $\mathcal{A}_\mathrm{B}$ is defined. As a result, the advective term does not vanish although it is much smaller than the other terms. Table 2.2 lists the normalised contribution of the three terms in the mean momentum equations for the full-span channel flow cases. The results indicate an enhanced form drag component for $C_o = 0.6$ that can be interpreted as a consequence of increased flow separation because the roughness elements are taller when compared to the case with $C_o = 1.0$. Additionally, this increase in the form drag occurs with a simultaneous decrease in the viscous drag for

the two Reynolds numbers. Since the driving pressure gradient (i.e., u_*^2/H) is constant for varying C_o for a given Re_*, only the bottom boundary conditions are responsible for an increase in the drag coefficient and the mean momentum partition. It is clear from Table 2.2 that there is a definitive increase in the form drag for decreasing C_o for both Re_*.

The relative importance of the viscous and form drag (relative drag) is depicted for varying C_o in figure 2.7. The minimal span channels capture the overall trend as predicted by the full span channels with a consistent over-prediction for all cases when compared to the full span data. As shown in figure 2.3, the time- and planform-averaged velocity profiles for the minimal-span channels leads to a flow velocity that is comparatively larger in magnitude away from the wall. Since the minimal-span channels do not effectively mix momentum in the vertical direction due to the span-wise domain constraint, we anticipate larger form drag as a result of this increased mean flow velocity away from the wall when compared to the full-span channel cases (Chung et al., 2015; Yuan and Piomelli, 2015). For both values of Re_*, the relative drag increases for decreasing values of C_o. Additionally, it is clear from this data that the relative drag increases faster for $Re_* = 700$ when compared to $Re_* = 350$, further validating the changes observed in C_d^τ (see figure 2.4).

Case Name	Form Drag	Viscous Drag	Advective Term	Sum
C700C1	0.773	0.214	0.017	1.00
C350C1	0.734	0.242	0.028	1.00
C700C06	0.863	0.129	0.011	1.00
C350C06	0.823	0.172	0.014	1.00
MC700C1	0.785	0.193	0.022	1.00
MC350C1	0.742	0.228	0.030	1.00
MC700C08	0.810	0.171	0.019	1.00
MC350C08	0.767	0.209	0.023	1.00
MC700C06	0.869	0.116	0.015	1.00
MC350C06	0.820	0.160	0.020	1.00
MC700C04	0.872	0.111	0.017	1.00

Table 2.2: Mean momentum partition computed using the discrete integration of the streamwise momentum equation. All terms are normalised by u_*^2/H.

2.5 Conclusions

We studied the effect of changing bottom boundary conditions through the definition of the Corey shape factor that characterises the individual roughness elements on the mean flow drag. Using a combination of full- and minimal-span channel flows and direct numerical simulations, we establish that decreasing Corey shape factors result in increased mean flow drag. Additionally, we validate that for sand-grain type roughness with $C_o = 1.0$, DNS can accurately replicate the Nikuradse (1933) estimate $z_0 \equiv \overline{k}_s/30$ without regression. We also observe that for decreasing values of C_o, there is enhanced flow separation for the two friction Reynolds numbers considered in this study. Furthermore, using a mean momentum analysis, we demonstrate that this

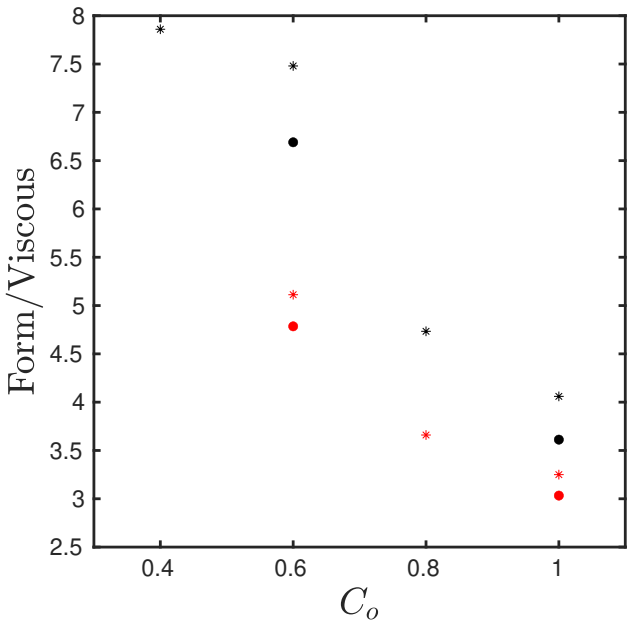

Figure 2.7: Comparison of the ratio of the form drag to the viscous drag for varying C_o. Black markers correspond to $Re_* = 700$ while red markers correspond to $Re_* = 350$. Full-span channels are denoted by filled circles while the minimal-span channels are denoted using the asterisk markers.

increased mean flow drag is a result of enhanced flow separation at the crest of the roughness elements that leads to a larger form drag contribution. Additionally, we show that the viscous drag decreases with the simultaneous increase in the form drag where these changes are both a function of the flow Reynolds number and the Corey shape factor. This study also explains variations in the drag coefficient (C_d or C_f) which is typically assumed to be only a function of the mean roughness height ($\overline{k}_s$). The drag coefficient was observed to be 2.5 times larger for $C_o = 0.4$ when compared to the drag coefficient when $C_o = 1.0$ for identical mean roughness height ($\overline{k}_s$) for $Re_* = 700$. Additionally, the roughness parameter correlates well with the standard deviation of the roughness height for varying C_o, thus providing a means to estimate the mean flow drag using the roughness characteristics.

Chapter 3

Drag enhancement by the addition of weak waves to a wave-current boundary layer over bumpy walls[1]

3.1 Abstract

We present direct numerical simulation (DNS) results of a wave-current boundary layer in a current-dominated flow regime (wave-driven to steady current ratio of 0.34) over bumpy walls for hydraulically smooth flow conditions (wave orbital excursion to roughness ratio of 10). The turbulent, wave-current channel flow has a friction Reynolds number of 350 and a wave Reynolds number of 351. At the lower boundary, a bumpy wall is introduced with a direct forcing immersed boundary method, while the top wall has a free-slip boundary condition. Despite the hydraulically-smooth nature of the wave-driven flow, the phase variations of the turbulent statistics for the bumpy wall case were found to vary substantially when compared to the flat wall case. Results show that the addition of weak waves to a steady current over flat walls has a negligible effect on the turbulence or bottom drag. However, the addition

[1] A version of this chapter was published in the Journal of Fluid Mechanics as "Drag enhancement by the addition of weak waves to a wave-current boundary layer over bumpy walls", by Patil and Fringer (2022).

of weak waves to a steady current over bumpy walls has a significant effect through enhancement of the Reynolds stress (RS) accompanied by a drag coefficient increase of 11% relative to the steady current case. This enhancement occurs just below the top of the roughness elements during the acceleration portion of the wave cycle: Turbulent kinetic energy (TKE) is subsequently transported above the roughness elements to a maximum height of roughly twice the turbulent Stokes length. We analyse the TKE and RS budgets to understand the mechanisms behind the alterations in the turbulence properties due to the bumpy wall. The results provide a mechanistic picture of the differences between bumpy and flat walls in wave-current turbulent boundary layers and illustrate the importance of bumpy features even in weakly energetic wave conditions.

3.2 Introduction

Estuarine bottom boundary layers are primarily driven by the combined action of tidal or wave-driven mean flows and oscillatory wave motions. Oscillatory wave motions provide the necessary bottom shear stress to erode the sediment bed, while the mean flows transport the sediment horizontally (Lacy and MacVean, 2016). Such bottom boundary layers often exhibit highly varying roughness characteristics both spatially and seasonally (Egan et al., 2019), leading to non-trivial effects in the bottom boundary layer dynamics. Due to practical limitations, most experimental literature on wave-current boundary layers has focused on flow conditions where the strength of the oscillatory wave motions is greater than the mean flow and the wave orbital excursion is larger than the roughness height. Numerically, the challenges in adequately resolving roughness features along with the turbulent physics impose steep requirements on the grid resolution. In the presence of laminar waves, the computational grid only needs to resolve the turbulence generated by the mean flow component.

However, as the oscillatory wave motion strengthens, turbulence generation occurs due to the mean flow shear and the instantaneous wave shear. This results in larger instantaneous flow Reynolds numbers, thus requiring finer grid resolution to resolve the turbulence. Accurate simulation of complex roughness features in a DNS framework imposes additional computational constrains. Consequently, most, if not all numerical studies investigating wave-current boundary layer flows have focused on understanding the dynamics for flat walls.

Typically, wave-current boundary layer flows are characterised by prescribing the strength of the mean flow, the strength of the oscillatory wave motion, and the ratio of the oscillatory wave excursion to the bed roughness height. The corresponding non-dimensional parameters are (a) the mean flow friction Reynolds number ($Re_* = u_* H/\nu$), where u_* is the friction velocity, H is the flow depth, and ν is the kinematic viscosity of the fluid, (b) the wave Reynolds number ($Re_w = U_b^2/(\omega\nu)$), where U_b is the maximum wave orbital velocity and ω is the wave frequency, and (c) the relative roughness ($A/\overline{k}_s$), where $A = U_b/\omega$ is the wave orbital excursion length, and $\overline{k}_s$ is the mean bed roughness height. As shown in figure 3.1(a), for a fixed relative roughness $A/\overline{k}_s$, purely oscillatory flow transitions from hydraulically smooth and laminar wave flow conditions to hydraulically rough and turbulent wave flow conditions with increasing Re_w. The flow may also transition to a hydraulically rough and turbulent wave flow state if the roughness height increases while $Re_w > 10^4$. For flat walls corresponding to the limit $A/\overline{k}_s \to \infty$, Lodahl et al. (1998) studied the effect of oscillatory wave motion over a turbulent mean flow and found two distinct flow regimes depending on Re_w and Re_* as shown in figure 3.1(b). The first regime (green line in figure 3.1(b)) corresponds to a low enough mean flow friction Reynolds number such that, upon increasing the wave strength (increasing Re_w), the wave-current boundary layer becomes wave-dominated (i.e., $U_c/U_b > 1$, where U_c is the mean flow velocity) before the wave transitions to a turbulent state (i.e., before

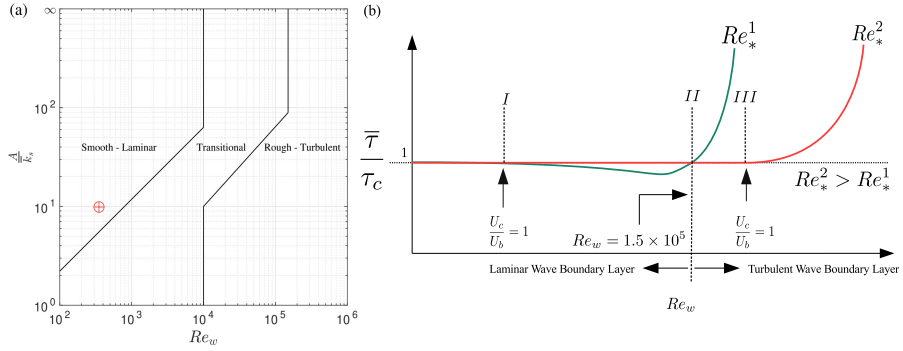

Figure 3.1: (a) Flow regime classification for purely oscillatory wave motion over bumpy walls. Black solid lines demarcate the boundaries of different wave flow conditions for varying Re_w and $A/\overline{k}_s$ (adapted from Lacy and MacVean (2016)). The red symbol marks case WC350B, one of the cases simulated in this paper as detailed in table 3.1. (b) Bottom stress (τ) for flat-wall, wave-current boundary layer flows for two mean flow Reynolds numbers Re_*^1 and Re_*^2 (adapted from Lodahl et al. (1998)). U_c is the mean flow velocity, U_b is the wave orbital velocity, and τ_c is the bottom stress without waves.

$Re_w = 1.5 \times 10^5$). This flow regime is characterised by a reduction in the bottom stress with the addition of waves between points I and II. Beyond point II, the wave becomes turbulent and the bottom stress increases monotonically with increasing wave strength. The second flow regime (red line in figure 3.1(b)) corresponds to a mean flow friction Reynolds number in which, upon increasing the wave strength, the wave-current boundary layer transitions to wave-dominated flow conditions after the critical value of $Re_w = 1.5 \times 10^5$. For this flow regime, the bottom stress remains constant and increases monotonically only after the flow becomes wave dominated (i.e., $U_b > U_c$). The findings of Lodahl et al. (1998) have since been validated numerically by Scotti and Piomelli (2001), Manna et al. (2012), Manna et al. (2015), and Nelson and Fringer (2018) to explain the underlying mechanisms leading to the non-monotonic bottom stress in the first regime.

Wave-current boundary layer flows over bumpy walls (finite $A/\overline{k}_s$ in figure 3.1(a))

have been extensively investigated experimentally (Grant and Madsen, 1979; Kemp and Simons, 1982, 1983; Arnskov et al., 1993). The Grant and Madsen (1979) wave-current model is the most widely accepted theory for wave-current boundary layer flows over rough walls. While the model holds for varying flow conditions, studies by Sleath (1987) and recent in-situ measurements in San Francisco Bay by Cowherd et al. (2021) have observed that the time-invariance of the eddy viscosity assumption does not hold for wave-current boundary layer flows. Cowherd et al. (2021) also found that the instantaneous boundary layer response assumed in Grant and Madsen (1979) may not hold.

Although the flat wall, wave-current boundary layer drag reduction has been thoroughly investigated numerically (Scotti and Piomelli, 2001; Manna et al., 2012, 2015; Nelson and Fringer, 2018), the energetics and mechanics of enhanced drag over bumpy walls have not been well studied for current-dominated flow conditions.The only exception is the work of Bhaganagar (2008) presenting first-order statistics for wave-current flows over egg-carton type roughness features in current-dominated flow conditions. In addition to the study by Bhaganagar (2008), numerical investigations of pulsative i.e., wave-current boundary layer flows have been carried out by Jelly et al. (2020) over a cosine based roughness topography in the recent past. Jelly et al. (2020) found that the contribution of pressure drag can be significant when compared to the skin friction drag during some portions of the wave cycle. They also found that outer-layer similarity proposed by Townsend (1976) holds for such unsteady forcing conditions. Despite these numerical explorations and the wide range of aforementioned experimental studies, the mechanisms explaining enhanced drag over rough walls predicted by Grant and Madsen (1979) are not well understood particularly in current-dominated flow conditions. These deficiencies reinvigorate the need to understand wave-current boundary layers using numerical simulations.

Although weak wind waves interacting with a turbulent current over roughness

elements are ubiquitous (Lacy and MacVean, 2016), numerical investigations of such systems are lacking in the literature. The present study aims to bridge this gap by using DNS to study the dynamics of a current-dominated, wave-current boundary layer over bumpy walls in hydraulically smooth (based on $A/\overline{k}_s$) flow conditions. In this paper, a hydraulically smooth bed corresponds to one in which $\overline{k}_s/\delta_w \lesssim 4$, where δ_w is the wave boundary layer thickness (Lacy and MacVean, 2016). The numerical wave-current flume replicates a U-tube type experimental setup that is commonly used to study wave-current boundary layers (Lodahl et al., 1998; Yuan and Madsen, 2015).

3.3 Problem formulation

3.3.1 Governing equations and computational framework

We perform DNS of wave-current boundary layer flows over flat and bumpy walls in a channel flow configuration using the immersed boundary method (IBM) to simulate the bumps. The governing equations are given by

$$\frac{\partial u_i}{\partial t} + \frac{\partial}{\partial x_j}(u_i u_j) = -\frac{1}{\rho_0}\frac{\partial p}{\partial x_i} + \nu\frac{\partial^2 u_i}{\partial x_j \partial x_j} + U_b\omega\cos(\omega t)\delta_{i1} + \Pi_c\delta_{i1} + F_{\mathrm{IBM}}, \tag{3.1}$$

$$\frac{\partial u_i}{\partial x_i} = 0, \tag{3.2}$$

where u_i is the velocity vector, t is time, x_j is the Cartesian coordinate vector, δ_{ij} is the Kronecker delta function, ρ_0 is the reference density of the fluid, p is the pressure, ν is the kinematic viscosity, U_b is the maximum wave orbital velocity, ω is the wave frequency, Π_c is the constant pressure gradient driving the flow, and F_{IBM}

is the immersed boundary force to represent the bumps (see below). Coordinate axes are aligned as x_1, x_2, and x_3 in the streamwise, spanwise, and vertical directions, respectively. Periodic boundary conditions are applied in the streamwise and spanwise directions, while a no-slip boundary condition is applied at the bottom wall and a free-slip boundary condition is applied at the top wall to simulate open-channel like geometries. The boundary conditions at the top wall are given by

$$u_3(x_3 = H) = 0, \quad \frac{\partial u_i}{\partial x_3}(x_3 = H) = 0 \quad \forall i \in 1, 2, \tag{3.3}$$

where H is the channel height. Choosing U_c, $\overline{k}_s$, and ν as the repeating variables, the bottom stress has a functional dependence given by (in this paper, the bottom stress is assumed to have units of velocity squared)

$$\frac{\tau}{U_c^2} = f\left(\frac{U_b}{U_c}, \frac{H}{\overline{k}_s}, \frac{U_c}{\omega \overline{k}_s}, \frac{U_c \overline{k}_s}{\nu}\right), \tag{3.4}$$

where the parameters on the R.H.S are flow dominance parameter (U_b/U_c), relative roughness ($H/\overline{k}_s$), Keulegan-Carpenter number ($KC = U_c/(\omega \overline{k}_s)$), and roughness Reynolds number ($Re_k = U_c \overline{k}_s/\nu$). The L.H.S of equation 3.4 is the drag coefficient. Note that the last two non-dimensional numbers can be represented using the friction velocity u_* instead of U_c, where $u_*/(\omega \overline{k}_s)$ is the friction velocity based Keulegan-Carpenter number, and $u_* \overline{k}_s/\nu$ is the roughness Reynolds number. It is important to note that this non-dimensional scaling is not unique for the governing equations described above. Choosing oscillatory motion based velocity (U_b), length ($A = U_b/\omega$), and time ($1/\omega$) scales gives

$$\frac{\partial u_i^*}{\partial t^*} + \frac{\partial}{\partial x_j^*}(u_i^* u_j^*) = -\frac{\partial p^*}{\partial x_i^*} + \frac{1}{Re_w}\frac{\partial^2 u_i^*}{\partial x_j^* \partial x_j^*} + \left(\cos(t^*) + T^* D^*\right)\delta_{i1} + F_{\mathrm{IBM}}^*, \tag{3.5}$$

where $(\cdot)^*$ denotes a non-dimensional quantity, Re_w is the wave Reynolds number, $T^* = u_*/(H\omega)$ is the response time scale ratio of the wave component to the characteristic turbulent component, and $D^* = u_*/U_b$ is the inverse of the flow dominance parameter as defined in equation 3.4 since u_* and U_c correspond to the steady component of the external forcing. By choosing a specific response time scale ratio such that "frozen" turbulence exists i.e., $\omega^+ > 0.04$ (Jelly et al., 2020), the flow system can be studied by only varying U_b.

The governing equations are solved with a staggered-grid, second-order accurate, finite-difference spatial discretisation (Orlandi, 2000; Moin and Verzicco, 2016). The fractional-step method with a third-order accurate Runge-Kutta time-advancing scheme is used to integrate the governing equations in time (Kim and Moin, 1985). The code has been validated in previous studies for turbulent channel flows (Lozano-Durán and Bae, 2016, 2019). We implement a direct forcing immersed boundary method to include irregular bumps at the bottom wall as proposed by Scotti (2006). It is important to note that computing surface integrals over the roughness elements is a non-trivial procedure due to the irregular nature of the bottom bathymetry. Consequently, computing forces over the roughness elements is not possible due to the direct forcing nature of the IBM. The principal utility of this approach is to model the effects of roughness without introducing additional control parameters. This computational approach to model the effect of roughness elements has been thoroughly validated by Yuan and Piomelli (2014).

3.3.2 Computational grid and simulation parameters

The channel has dimensions $2H$, H, and H in the streamwise, spanwise, and vertical directions, respectively. These channel dimensions are sufficiently large to correctly predict one-point statistics for $Re_* \leq 4200$ (Lozano-Durán and Jiménez, 2014). The constant pressure gradient in equation 4.6 is prescribed as $\Pi_c = u_*^2/H$, where $u_* =$

0.0035 m/s, and $H = 0.1$ m. The oscillatory pressure gradient in equation 4.6 is prescribed by fixing $U_b = 0.021$ m/s and $\omega = 2\pi/T_w$, where $T_w = 5$ s is the wave period. The non-dimensional forcing frequency $\omega^+ = 0.1026 > 0.04$ indicates that the turbulence is expected to display asymptotic behaviour towards the "frozen" state as detailed in Jelly et al. (2020). Based on these body forcing conditions, the flow is expected to be in the current dominated regime $U_b/U_c \leq 1$. Additionally, the roughness conditions for the bumpy wall case correspond to hydraulically smooth flow conditions since the relative roughness is $\overline{k}_s/\delta_w = 1.34 < 4$, where δ_w is the wave boundary layer thickness, the friction Reynolds number is $Re_* = u_* H/\nu = 350$, and the wave Reynolds number is $Re_w = U_b^2/(\omega\nu) = 351$. For the bumpy wall case, the channel is discretised with $512 \times 256 \times 128$ grid points, and for the flat wall case, the channel is discretised with $512 \times 256 \times 92$ grid points. Uniform grid spacing is used over the bumpy surface (roughness elements) with a resolution of $\Delta x_3^+ = 0.45$, where the plus unit indicates normalisation by wall units, i.e. $\Delta x_3^+ = u_* x_3/\nu$. Above the roughness crest, the grid is stretched so that the maximum vertical grid spacing at $x_3 = H$ is $\Delta x_{3,max}^+ = 6.6$. For the flat wall case, the first vertical grid cell has a height $\Delta x_3^+ = 0.5$ and stretched until $\Delta x_3^+ = 8.0$. Uniform grid spacing is used in the streamwise and spanwise directions with $\Delta x_1^+ = \Delta x_2^+ = 4.2$ for both the flat and bumpy wall cases. The mean roughness height for the bumpy wall cases is $\overline{k}_s^+ = 6$, with the grid resolution comparable to Yuan and Piomelli (2014). It is important to note that this grid resolution is sufficient to resolve the maximum friction velocity based on the superposition of the steady and oscillatory flows (Stokes, 1851). Using the maximum instantaneous friction velocity, the resolution over the roughness elements is $\Delta x_3^+ = 0.7$, $\Delta x_{3,max}^+ = 11.63$, and $\Delta x_1^+ = \Delta x_2^+ = 7.27$, which is sufficient for resolving the requisite turbulent features. Note that the instantaneous friction velocity is twice as large as the mean friction velocity for the flat wall case. However, since the waves are laminar, they are not expected to generate associated turbulent

structures for the flat wall case. Therefore, resolving the mean friction velocity is sufficient for the flat wall case. A time step size of $\Delta t^+ = \Delta t/T_\epsilon \equiv 1.75 \times 10^{-4}$ ($T_\epsilon = H/u_*$ is the eddy turn over time) is used for all cases based on ensuring a maximum Courant number of 0.4 for a total simulation time of 10^3 s or 200 wave periods for the wave-current cases. Simulations are run at the Texas Advanced Computing Cluster on Stampede2 (Intel KNL) using 64 processors. On average, 6144 processor hours are required to simulate 10^3 s of real time. The various flow simulations carried out are listed in table 3.1.

The rough wall at the bed is generated by placing an array of randomly oriented ellipsoids centered at $x_3 = -0.5\overline{k}_s$, with their semi-axes lengths $k_{s,x_1} = \overline{k}_s$, $k_{s,x_2} = 1.4\overline{k}_s$, and $k_{s,x_3} = 2\overline{k}_s$ as originally proposed by Scotti (2006). Using this algorithm, the value of $\overline{k}_s^+$ is known a-priori as seen in figure 3.2(c). Shape characterisation can be achieved through the definition of the Corey shape factor (Corey, 1949)

$$C_o = \frac{k_{s,x_1}}{\sqrt{k_{s,x_3} k_{s,x_2}}}. \tag{3.6}$$

The IBM algorithm results in a roughness function (or area fraction) $\psi_r(x_3)$ that is a function of the vertical coordinate axis, thus eliminating the need to include streamwise and spanwise separation length scales in the roughness function definition. Figure 3.2(a) shows a schematic of the channel with roughness elements at the bottom wall with the mean roughness height $\overline{k}_s^+ = 32$, and panel (b) shows one such ellipsoidal roughness element represented on the computational grid. The blue region corresponds to the grid points within the solid, while the yellow shaded region corresponds to the grid points that are within the fluid. Panel (c) shows the roughness function $\psi_r(x_3)$ for cases C350B and WC350B. The roughness features employed in this paper have $C_o = 0.6$. As discussed in Section 3.4.3, the smaller value of C_o when compared to sand-grain type roughness (spheres with $C_o = 1$) leads to a larger drag

Acronym	Re_*	Re_w	$\overline{k}_s^+ = u_*\overline{k}_s/\nu$	$H/\overline{k}_s$	$KC = u_*/(\omega\overline{k}_s)$	U_b/U_c	$\overline{k}_s/\delta_w$	N_w
C350F	350	0	-	-	-	-	-	-
WC350F	350	351	-	-	-	0.34	0	100
C350B	350	0	6	59	-	-	-	-
WC350B	350	351	6	59	1.64	0.34	1.34	100

Table 3.1: The various DNS cases carried out with C denoting the steady channel flow cases, WC denoting the wave-current case, 350 denotes the friction Reynolds number for the steady component, the letter F denotes the flat wall case, the letter B denotes the bumpy wall case, and N_w denotes the number of wave periods after an initial transient of 100 periods over which the statistics are gathered for the wave-current cases. The wave boundary layer thickness is defined as $\delta_w = \sqrt{2\nu/\omega}$. The wave-current cases are hydraulically smooth based on $\overline{k}_s/\delta_w < 4$ (Lacy and MacVean, 2016).

coefficient due to the protruding nature of the ellipsoids into the boundary layer.

3.3.3 Flow velocity decomposition and averaging methods

We decompose the flow variables $f_i(x_1, x_2, x_3, t)$ into four components

$$f_i(x_1, x_2, x_3, t) = \langle\overline{f}_i\rangle(x_3) + \widetilde{f}_{r,i}(x_1, x_2, x_3, t) + \langle\tilde{f}_{w,i}\rangle(x_3, t) + f_i'(x_1, x_2, x_3, t), \quad (3.7)$$

where the terms on the right-hand side are, respectively, the double-averaged, dispersive, wave, and turbulent flow components. This velocity decomposition is similar to Nikora et al. (2007) and Mignot et al. (2009) except for the wave component. In equation 3.7, the time average $\overline{\cdot}$, the phase average $\widetilde{\cdot}$, and the planform average $\langle\cdot\rangle$ are given by

$$\overline{f}_i(x_1, x_2, x_3) = \frac{1}{T_{avg}} \int_t^{t+T_{avg}} f_i(x_1, x_2, x_3, t')dt', \quad (3.8)$$

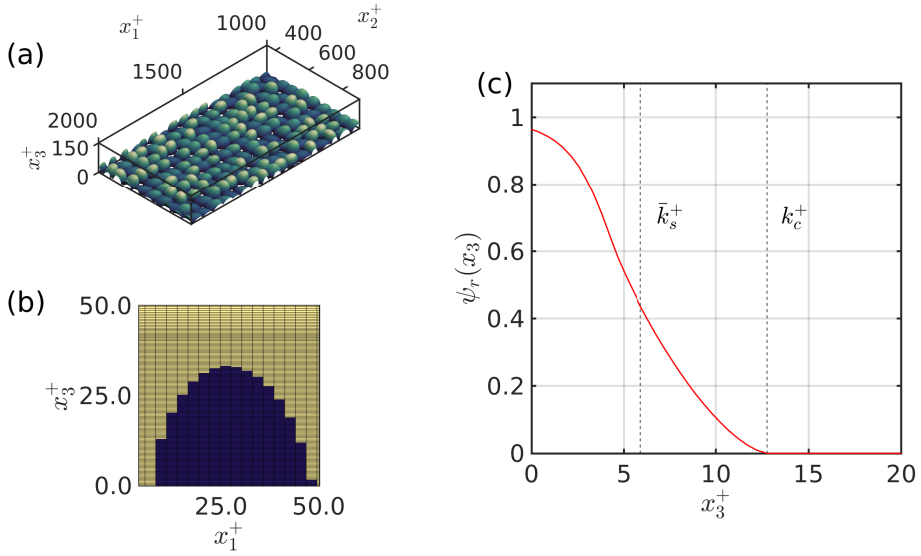

Figure 3.2: (a) Bumpy wall generated using an array of randomly oriented ellipsoidal elements for $\overline{k}_s^+ = 32$. (b) Close up view of the grid and roughness element for $\overline{k}_s^+ = 32$. (c) Roughness function depicting the mean roughness height $\overline{k}_s^+ = 6$ and the top of the roughness elements k_c^+ for the current dominated case discussed in this study.

$$\widetilde{f}_i(x_1, x_2, x_3, t) = \frac{1}{N_w} \sum_{j=1}^{N_w} f_i(x_1, x_2, x_3, t + jT_w) - \overline{f_i}(x_1, x_2, x_3), \tag{3.9}$$

$$\langle f_i \rangle(x_3, t) = \frac{1}{A_f(x_3)} \int_{A_f(x_3)} f(x_1, x_2, x_3, t) dA, \tag{3.10}$$

where T_{avg} is the time over which time-averaging is carried out, N_w is the number of waves over which the phase averaging is computed, and $A_f(x_3) = 2\pi^2 H^2[1 - \psi_r(x_3)]$ is the planform area occupied by the fluid which varies with height x_3 due to the bumps. Additionally, the vertical integral of the planform-averaged quantity gives the volume average

$$\langle f_i \rangle_v(t) = \frac{1}{H} \int_0^H \langle f_i \rangle(x_3', t) dx_3', \tag{3.11}$$

and the cumulative mean at time t_{cm} is given by

$$\overline{f}_i^{cm} = \frac{1}{t_{cm}} \int_0^{t_{cm}} f_i(t) dt. \tag{3.12}$$

Planform averaging equation 3.7 gives the vertical profile of the wave component

$$\langle \widetilde{u}_{w,i} \rangle(x_3, t) = \langle u_i \rangle(x_3, t) - \langle \overline{u}_i \rangle(x_3), \tag{3.13}$$

and phase averaging equation 3.7 gives the dispersive component (Raupach et al., 1991)

$$\widetilde{u}_{r,i}(x_1, x_2, x_3, t) = \widetilde{u}_i(x_1, x_2, x_3, t) - \langle \overline{u}_i \rangle(x_3) - \langle \widetilde{u}_{w,i} \rangle(x_3, t). \tag{3.14}$$

Using the time-averaged velocity component along with the identities in equations 3.13 and 3.14, the turbulent velocity component can be isolated using the identity in equation 3.7 as

$$u_i'(x_1, x_2, x_3, t) = u_i(x_1, x_2, x_3, t) - \langle \overline{u}_i \rangle (x_3) - \langle \widetilde{u}_{w,i} \rangle (x_3, t) - \widetilde{u}_{r,i}(x_1, x_2, x_3, t). \quad (3.15)$$

Using the time- and phase-averaging definitions in equations 3.8 and 3.9, it can be shown that for any two flow variables f and g, $\overline{\widetilde{f'\widetilde{g}}} = \widetilde{f'\widetilde{g}} = 0$, while, $\widetilde{f'} = \overline{\widetilde{f}} = 0$, $\widetilde{\widetilde{f}\widetilde{g}} = \widetilde{f}\widetilde{g} - \overline{\widetilde{f}\widetilde{g}}$, and $\overline{f'} = 0$ (Hussain and Reynolds, 1970). Velocity and pressure data are stored every $T_w/20$ for the wave-current cases to compute the statistics, and these data are used to study the phase variability

The turbulent Stokes length (l_t^+) defined as

$$l_t^+ = l_s^+ \left[\frac{\kappa l_s^+}{2} + \sqrt{1 + \left(\frac{\kappa l_s^+}{2} \right)^2} \right] = 9.8 \quad (3.16)$$

measures the height below which the waves affect the turbulence (Scotti and Piomelli, 2001). In equation 3.16, $l_s^+ = \sqrt{2u_*^2/\omega\nu} = u_*\delta_w/\nu = 4.4$ is the non-dimensional wave boundary layer thickness. Using the roughness crest (k_c^+) and the turbulent Stokes length (l_t^+), the channel depth H can be divided into three distinct regions in the vertical. The vertically-integrated flow quantity corresponding to each of these regions is given by

$$f_i^{(I)} = \int_0^{k_c^+} f_i dx_3^+, \quad (3.17)$$

$$f_i^{(II)} = \int_{k_c^+}^{2l_t^+} f_i dx_3^+, \quad (3.18)$$

$$f_i^{(III)} = \int_{2l_t^+}^{Re_*} f_i dx_3^+. \quad (3.19)$$

3.4 Results and discussion

3.4.1 Instantaneous flow features within the roughness elements

To assess the impact of the roughness elements on the near-wall flow features, figure 3.3 compares instantaneous horizontal velocity contours for the four cases discussed in this chapter. Owing to the small non-dimensional roughness $\overline{k}_s^+ = u_*\overline{k}_s/\nu = 6$ (formally, roughness is hydraulically smooth when $\overline{k}_s^+ \leq 4$ (Jiménez, 2004)), there are no obvious separation regions for the steady flow case with bumps. Furthermore, despite the stronger velocity fluctuations for the wave-current case with bumps (compare the flat and bumpy wave-current cases at $\omega t = 8\pi/5$ in figure 3.3), based on the small value of $KC = u_*/(\omega\overline{k}_s) = 1.64$, there are very weak flow-separation features when bumps are added to the wave-current case (at $\omega t = 3\pi/5$). This is consistent with Nielsen (1992), who points out that the relative importance of form drag (or flow separation induced pressure drag) decreases with decreasing KC number. Furthermore, as discussed in Section 3.4.5, the contributions due to the dispersive stresses that are associated with flow separation are minimal compared to the contributions from other flow features that are observed. Rather than exhibiting flow separation which would imply an increase in the form drag by the roughness elements, the flow in the roughness elements is dominated by viscous effects which essentially decelerate the flow, much like the flow in a wave-current, rough-wall boundary layer that resembles a canopy flow (Egan et al., 2019).

The viscous effects in the bumps merely alter the behavior of the Stokes boundary layer in the oscillatory flow. During the acceleration phase of the wave cycle ($\pi/10 \leq \omega t \leq 3\pi/5$), although the boundary layer thickness is substantially reduced for both

wave-current cases when compared to the steady cases, it is thicker for the wave-current case with bumps. Similarly, during the deceleration phase of the wave cycle ($\pi \leq \omega t \leq 8\pi/5$), there is a subsequent increase in the boundary layer thickness for both wave-current cases, although again it is thicker in the presence of bumps. This behavior of the boundary layer flow that is out of phase with the driving pressure gradient is consistent with the modified Stokes boundary layer depicted in figure 3.10. Despite the weak flow separation induced by the roughness features, they induce stronger flow variability and velocity fluctuations which produce stronger velocity shear and Reynolds stress, thus increasing the bottom drag coefficient as discussed in what follows.

3.4.2 Measure of convergence for turbulent statistics

The steady flat and bumpy wall cases C350F and C350B are simulated for a total of 40 eddy turnover times (T_ϵ). The first $10T_\epsilon$ involve an initial transient after which the flow requires about $20T_\epsilon$ for the turbulent kinetic energy (TKE) to equilibrate, beyond which the turbulence statistics are computed with $T_{avg} = 10T_\epsilon$. The initial conditions for these cases are given by

$$u_1(x_1, x_2, x_3) = 2U_c\,(1 - x_3/H) + \alpha_{TI} R(x_1, x_2, x_3), \tag{3.20}$$

$$u_2(x_1, x_2, x_3) = \alpha_{TI} R(x_1, x_2, x_3), \tag{3.21}$$

$$u_3(x_1, x_2, x_3) = \alpha_{TI} R(x_1, x_2, x_3), \tag{3.22}$$

where U_c is the mean of the velocity profile given composed of the viscous sub-layer and log-law,

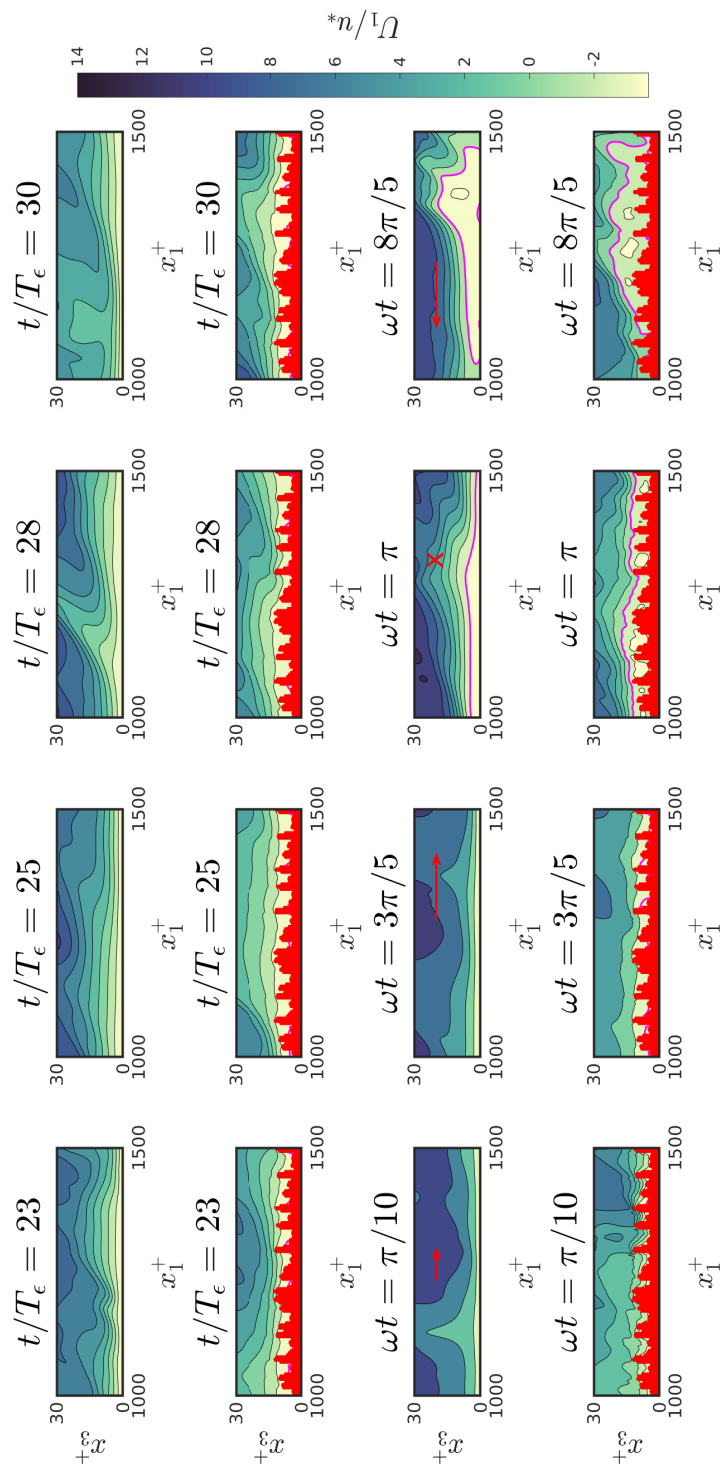

Figure 3.3: Contours of instantaneous streamwise velocity (u_1/u_*) for the four cases discussed in this chapter along the streamwise transect at $x_2^+ = 330$. The 1^{st} row corresponds to case C350F, the 2^{nd} row corresponds to case C350B, the 3^{rd} row corresponds to case WC350F, and the 4^{th} row corresponds to case WC350B. For the steady flow cases (i.e., C350F and C350B), the four panels correspond to different instantaneous turnover times $t^+ = u_* t/H$, while the four panels for the wave-currents cases (i.e., WC350F and WC350B) correspond to different wave phases ωt relative to time $t^+ = 20$. The magenta contours indicate $u_1/u_* = 0$, while the red arrows in the third row indicate the mean wave velocity $\sin(\omega t)$ for both wave-current cases. The roughness elements are indicated by the red regions in the figures. Transects at other locations and times exhibit similar behavior lacking obvious flow separation features.

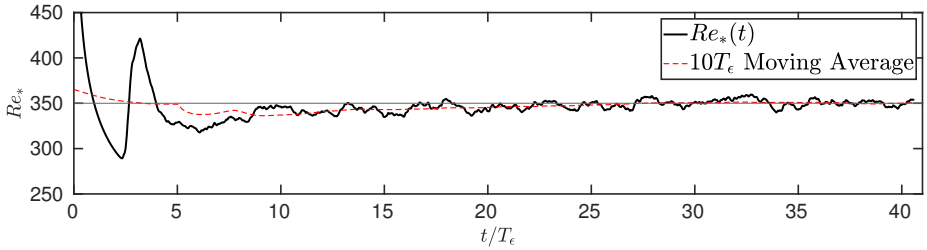

Figure 3.4: Time-evolution of Re_* for case C350F.

$$U_c = \frac{u_*}{Re_*}\left\{\int_0^{11.6} x_3^+ dx_3^+ + \int_{11.6}^{Re_*}\left[\frac{1}{\kappa}\ln\left(x_3^+\right) + 5.2\right] dx_3^+\right\}, \tag{3.23}$$

which ensures that the volume- and time-averaged velocity is given approximately by U_c. The magnitude of the initial perturbations is $\alpha_{TI} = 0.05$, $R(x_1, x_2, x_3)$ is a uniformly distributed random number in the range $[-1, 1]$, and $\kappa = 0.4$ is the von Kármán constant. Figure 3.4 shows the time evolution of the friction Reynolds number which converges after roughly $25T_\epsilon$, after which the deviations of the moving average over one eddy turnover from the target value are less than 0.5%. The flow transitions to a turbulent state at $3T_\epsilon$, subsequently leads to the evolution of streamwise turbulent structures that require about $20T_\epsilon$ to reach the target levels dictated by the driving pressure gradient. The linear stress profile in figure 3.5 is used as an indicator for the level of convergence and validation of the results attained in the DNS. The corresponding streamwise velocity profile also follows the linear and log-law analytic predictions when averaged over $10T_\epsilon$ following the initial transient of $30T_\epsilon$ as shown in figure 3.6.

Once the steady cases reach equilibrium after $30T_\epsilon$, the three-dimensional velocity fields are used as initial conditions for the wave-current cases. The convergence of time-averaged energetics in the wave-current cases can be estimated by observing the departure of the time rate of change of TKE from zero. This convergence criterion for the flat wall case can be formulated using the volume-integrated TKE balance

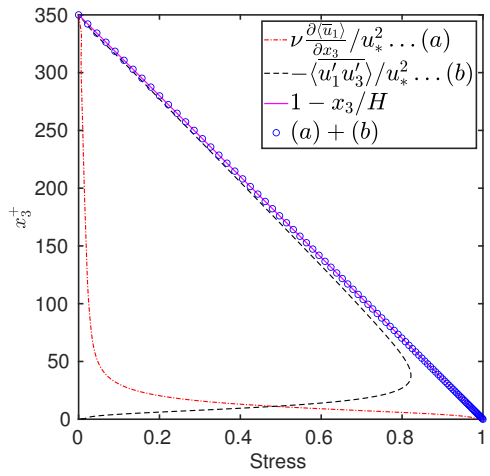

Figure 3.5: Time- and planform-averaged viscous stress, Reynolds stress, and total stress profiles for case C350F. The time averaging is carried out over $10T_\epsilon$ for $t/T_\epsilon \geq 30$.

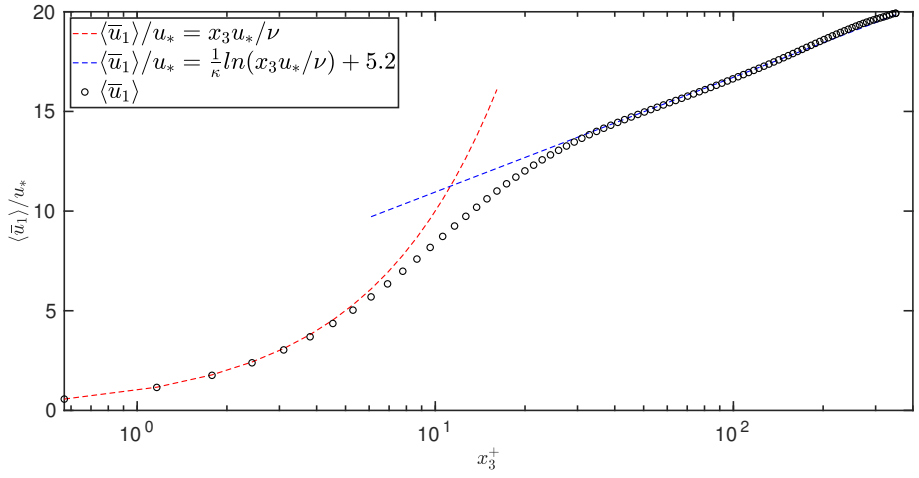

Figure 3.6: Comparison of time- and planform-averaged, streamwise velocity profile for case C350F against the linear and log-law analytic expressions. The time averaging is carried out over $10T_\epsilon$ for $t/T_\epsilon \geq 30$.

equation given by

$$\frac{\partial \langle k \rangle_v}{\partial t} = -\langle P_k \rangle_v + \langle \epsilon_k \rangle_v, \tag{3.24}$$

where $\partial \langle k \rangle_v / \partial t$ is the time rate of change of volume-integrated TKE, $\langle P_k \rangle_v$ is the volume-integrated TKE production by mean shear, and $\langle \epsilon_k \rangle_v$ is the volume-integrated dissipation of TKE. Time-averaging equation 3.24 over an integer number of wave periods implies that the time-averaged TKE production is balanced by the time-averaged dissipation of TKE. Thus, we can conclude that the wave-current system reaches equilibrium once $\partial \langle k \rangle_v / \partial t = 0$ in a time-averaged sense. Based on the definitions presented above, the flat wall, wave-current case appears to converge after around $40T_w$ as seen in figure 3.7. This suggests that the flow in the flat wall, wave-current case requires an additional $6T_\epsilon \sim 40T_w$ after the introduction of the oscillatory pressure gradient to reach equilibrium as defined earlier. As for the bumpy wall, wave-current case, the system reaches equilibrium within $20T_w$ or $3T_\epsilon$, which is consistent with the elevated bottom drag and dissipation for flows over bumpy walls. The convergence of flow statistics has been verified by integrating the governing equations for an additional 200 wave periods and it was found that the statistics change by no more than 1%. In what follows, the turbulent statistics are computed with $T_{avg} = 100T_w$ after an initial transient of 100 wave periods to avoid any residual transitional effects.

3.4.3 Mean and wave-driven velocity profiles

Figure 3.8 shows that the flat wall cases C350F and WC350F follow the log-law, with minimal differences observed between the two cases. Close to the wall ($x_3^+ < 6$), the two cases are identical, while minor differences can be observed outside the buffer layer ($x_3^+ > 30$). These results are consistent with the findings of Lodahl et al. (1998); Manna et al. (2012), and Nelson and Fringer (2018) which suggest that the addition

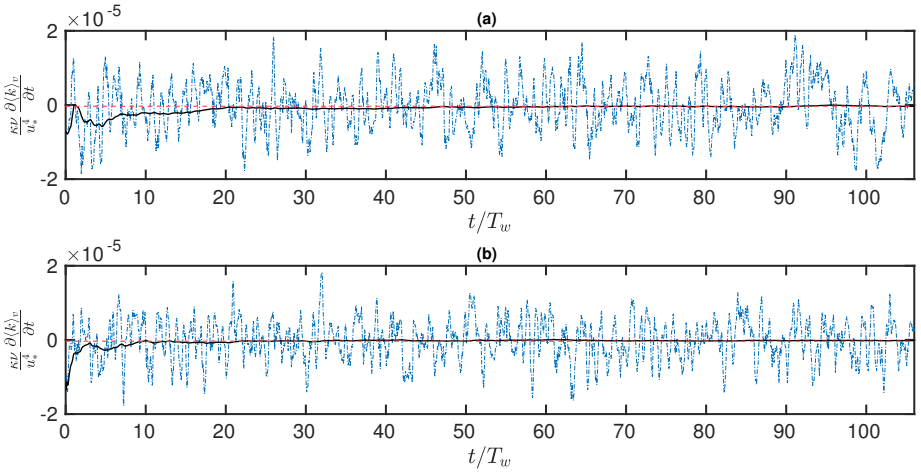

Figure 3.7: Time evolution of the time rate of change of the volume-integrated turbulent kinetic energy. Panel (a) case WC350F and Panel (b) case WC350B. The blue dash-dot lines correspond to the instantaneous value, the solid black lines correspond to the cumulative mean starting from $t/T_w = 0$ until the instantaneous value, while the red dashed lines correspond to the mean over the entire time series.

of a laminar wave to a turbulent current over flat walls in the current dominated flow regime does not alter the mean velocity profile significantly. The bumpy wall log-law is given by (Raupach et al., 1991)

$$\frac{\langle \overline{u}_1 \rangle}{u_*} = \frac{1}{\kappa} \ln \left(\frac{x_3 - \overline{k}_s}{z_0} \right), \tag{3.25}$$

where $\overline{k}_s$ is known a-priori (see figure 3.2) and $z_0 = \overline{k}_s/\alpha_k$, where α_k is the regression factor used to fit the velocity profiles. The values for u_* and κ are constant as discussed earlier. Regressing for α_k for cases C350B and WC350B yields $\alpha_k = 26$ and $\alpha_k = 19$, respectively. For conventional sand-grain type roughness, Nikuradse (1933) proposed $\alpha_k = 30$, where smaller values of α_k imply a larger effective roughness z_0. It is also crucial to note that the sand-grain type roughness discussed in Nikuradse (1933) have $C_o = 1.0$. As seen in figure 3.8, the mean velocity profile for WC350B shifts further away from the flat wall log-law when compared to C350B. Unlike the flat wall cases, the bumpy wall cases are expected to show enhanced drag coefficients

when compared to the flat wall cases. This drag coefficient enhancement is a function of the Corey shape factor presented in equation 3.6. As suggested by Julien (2010), with decreasing C_o the drag coefficient should increase. Therefore, case C350B with a $C_o = 0.6$ exhibits a larger drag coefficient when compared to the sand grain type roughness elements with $C_o = 1.0$ (Raupach and Thom, 1981; Ghodke and Apte, 2017). The smaller value of α_k observed for case WC350B suggests that despite the laminar nature of the wave, it greatly affects the mean flow for bumpy wall cases.

A quantitative measure of the effects of waves is given through a drag coefficient defined as

$$C_d^* = \frac{u_*^2}{\langle \overline{u}_1 \rangle_v^2}. \tag{3.26}$$

Obtaining vertical profiles of the velocity in experimental or in-situ studies of wave-current boundary layers may not always allow computing the drag coefficient using equation 3.26. In this case, the drag coefficient can be defined by assuming a log-law velocity profile, which gives

$$C_d = \left[\frac{\kappa}{\ln(H/z_0) - 1} \right]^2, \tag{3.27}$$

where $z_0 = \overline{k}_s/\alpha_k$ for bumpy walls and $z_0 = \nu/(9u_*)$ for flat walls. As shown in table 3.2, C_d and C_d^* for the flat wall case C350F are comparable to previous numerical studies (Moser et al., 1999). Case WC350F, as expected, does not show any substantial changes in the drag coefficient. However, there is a significant increase in the drag coefficient with the addition of bumps when compared to the flat wall case. Case WC350B surprisingly shows enhanced drag coefficient when compared to case C350B, despite the laminar nature of the waves. Comparison of C_d for case WC350B against the experimental studies by Fredsøe (1984), Myrhaug and Slaattelid (1990) and Huynh-Thanh and Temperville (1991) with similar z_0/H values supports the

validity of the numerical results. However, we note that the flow conditions in the experimental studies listed in table 3.2 correspond to wave-dominated flow conditions since $U_b/\langle\overline{u}_1\rangle_v > 1$ for all cases. These results suggest that the principal conclusion of drag coefficient enhancement under the combined action of waves and currents over rough walls from the wave-current turbulence model developed by Grant and Madsen (1979) hold even for weak wave-current interactions in the current dominated flow regimes. This is despite the fact that the wave-current model proposed by Grant and Madsen (1979) does not apply in the hydraulically smooth wall and current-dominated flow conditions. Using the Grant and Madsen (1979) wave-current friction factor formulation, it can be shown that the lower limit for its validity is $U_b/\langle\overline{u}_1\rangle_v = 0.59$, while $U_b/\langle\overline{u}_1\rangle_v = 0.38$ for case WC350B. These results suggest that C_d^* is a good predictor of the drag coefficient as long as z_0/H is accurately estimated as a function on Re_*, Re_w, $H/\overline{k}_s$, and $u_*/(\omega\overline{k}_s)$. However, the central challenge is to accurately estimate z_0/H as a function of the relevant non-dimensional parameters as discussed in Grant and Madsen (1979). Figure 3.9 supports this observation and suggests that the differences observed between the drag coefficient presented in equations 3.26 and 3.27 can be attributed to the mismatch of $\langle\overline{u}_1\rangle_v(x_3 = H)$ and the log-law prediction. This mismatch is expected to increase with increasing Re_*, due to the presence of a wake region. Wave-driven turbulence, stratification, and inclusion of a buffer region may also affect this comparison (Egan et al., 2020b).

Figure 3.10 shows the differences between the phase-averaged wave velocity for the flat and bumpy wall cases. The analytical solution proposed by Stokes (1851) compares well with the DNS after regressing to determine the wall height. The DNS predicts slightly enhanced peak wave velocities when compared to the analytic solution, although the solutions agree well far from the wall. These results suggest that the wave and the turbulent flow fields are decoupled and any correlations between these two flow components will be small for the current-dominated flow system. This

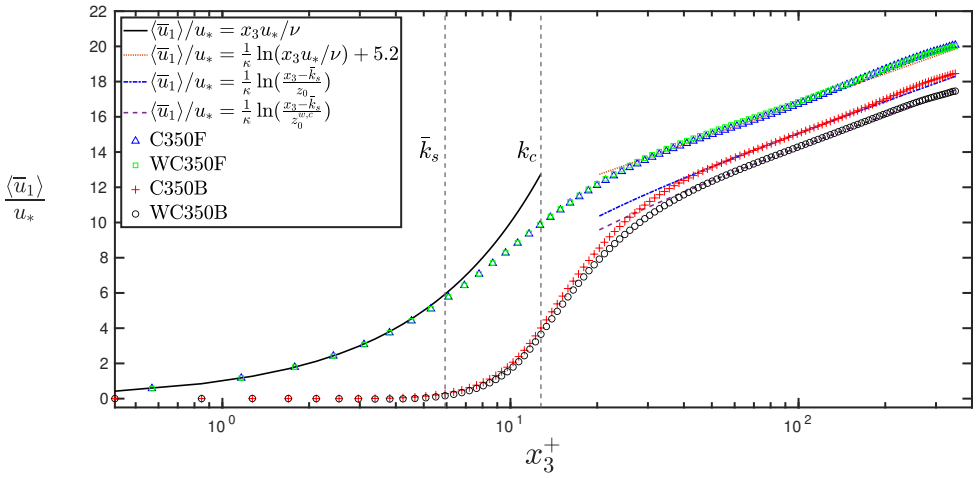

Figure 3.8: Time- and planform-averaged velocity profiles for the flat and bumpy wall cases.

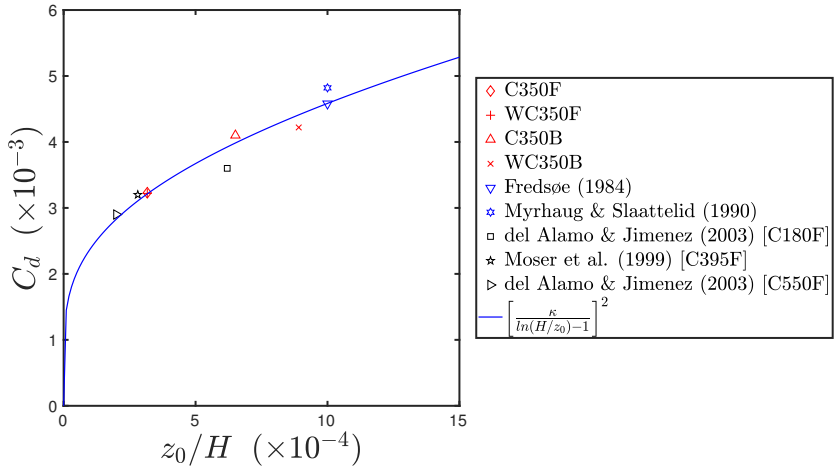

Figure 3.9: Comparison of the drag coefficient computed in the present study against experimental, numerical, and analytic expressions.

Data Source	z_0/H $(\times 10^{-4})$	C_d $(\times 10^{-3})$	C_d^* $(\times 10^{-3})$	Re_*	Re_w	$U_b/\langle \overline{u}_1 \rangle_v$
C350F	3.17	3.21	3.23	350	0	0
WC350F	3.17	3.21	3.22	350	351	0.34
C350B	6.51	3.98	4.10	350	0	0
WC350B	8.91	4.41	4.22	350	351	0.38
Fredsøe (1984); Myrhaug and Slaattelid (1990)	10	4.58	-	NA	NA	> 1
Huynh-Thanh and Temperville (1991)	10	4.82	-	NA	NA	> 1
del Álamo and Jiménez (2003) (C180F)	6.20	3.92	3.60	180	0	0
Moser et al. (1999) (C395F)	2.81	3.10	3.20	395	0	0
del Álamo and Jiménez (2003) (C550F)	2.00	2.84	2.90	550	0	0

Table 3.2: Comparison of drag coefficient computed in the present study to wave-current experiments by Fredsøe (1984), Myrhaug and Slaattelid (1990), and Huynh-Thanh and Temperville (1991) in addition to the steady current flat wall DNS cases by Moser et al. (1999) and del Álamo and Jiménez (2003). Wave-Current experimental data adapted from Soulsby et al. (1993).

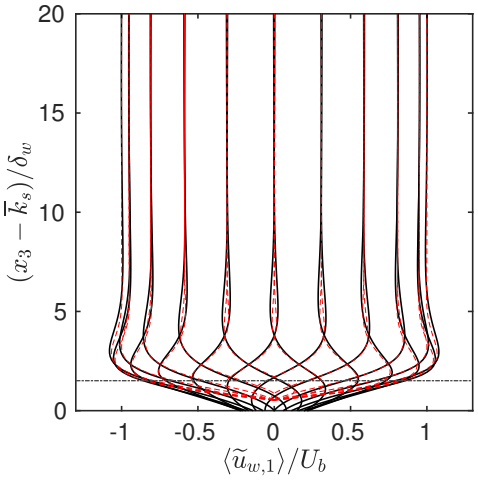

Figure 3.10: Phase- and planform-averaged wave velocity for the bumpy wall case compared with the Stokes wave solution. Black solid line corresponds to the WC350B case while the red dashed line corresponds to the Stokes wave solution. The black dash-dot line denotes the roughness crest level (k_c). The vertical coordinate is normalised by the Stokes boundary layer thickness $\delta_w = \sqrt{2\nu/\omega}$.

also suggests one-way coupling in which the waves affect the turbulence but the turbulence does not affect the waves (Manna et al., 2012).

3.4.4 Time- and planform-averaged stress profiles

The time- and planform-averaged momentum balance for the wave-current channel flow system above the roughness crest is given by

$$0 = \Pi_c + \frac{\partial \langle \overline{\tau} \rangle}{\partial x_3}, \tag{3.28}$$

where the oscillatory forcing vanishes due to time-averaging, $\langle \overline{\tau} \rangle$ represents the time-averaged and planform-averaged total stress, which is the sum of the viscous and the Reynolds stress, viz. $\langle \overline{\tau} \rangle = \nu \frac{\partial \langle \overline{u}_1 \rangle}{\partial x_3} - \langle \overline{u_1' u_3'} \rangle$. Integrating equation 3.28 from some height x_3 to the channel height $x_3 = H$ (where $\langle \overline{\tau} \rangle = 0$) and substituting $\Pi_c = u_*^2/H$ gives

$$\frac{\langle\overline{\tau}\rangle}{u_*^2} = 1 - \frac{x_3}{H}. \tag{3.29}$$

This result suggests that the time- and planform-averaged stress profile above the roughness elements for the wave-current bumpy wall case follows the traditional linear stress profile. Figure 3.11 shows the time- and planform-averaged stress profiles for the four cases discussed earlier. Above the roughness crest, the total stress profiles collapse onto the analytic solution presented in equation 3.29. For the bumpy wall cases below the roughness crest, the immersed boundary force (not shown in figure 3.11) accounts for the deficit stress. This immersed boundary force cannot be easily computed due to the irregular nature of the roughness elements, although it has been validated in previous studies (Scotti, 2006; Yuan and Piomelli, 2014). There are no significant differences between cases C350F and WC350F. For the bumpy wall cases, there is appreciable attenuation of the streamwise rms velocity $\left(u_{i,\mathrm{rms}} = \sqrt{\langle\overline{u_i'^2}\rangle}\right)$ for the wave-current case when compared to its steady current counterpart. This attenuation is limited to a region above the roughness crest throughout the effective buffer layer region ($5 \lesssim x_3^+ - \overline{k}_s^+ \lesssim 30$). Below the roughness crest, the wave-current case shows elevated streamwise rms velocities compared to the other cases. Similar trends are observed for case C350B, suggesting that compared to the flat wall, the roughness elements act as a momentum sink that is stronger for case WC350B when compared to case C350B. Above the roughness elements, the log-law region shows the opposite trend for the streamwise rms velocity, with case WC350B showing larger values compared to the other cases. For the spanwise and vertical rms velocity profiles, the general trend compared to that of the streamwise rms velocity profile is opposite, suggesting that there are exchanges between the streamwise, spanwise and vertical momentum fluctuations.

The vertical and wave phase variation of the turbulent kinetic energy $\left(\widetilde{\langle u_i' u_i'\rangle}\right)$

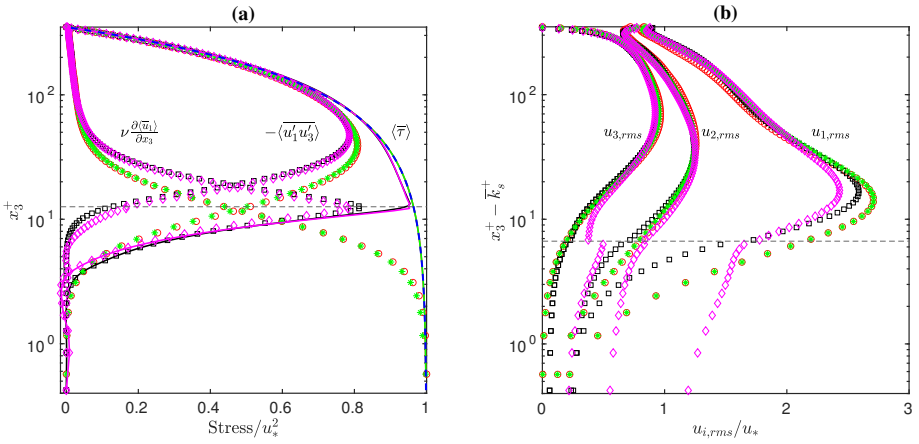

Figure 3.11: (a) Comparison of time-averaged and planform-averaged viscous $\left(\nu\frac{\partial\langle\overline{u}_1\rangle}{\partial x_3}\right)$, Reynolds $\left(-\langle\overline{u_1'u_3'}\rangle\right)$, and total stress $(\langle\overline{\tau}\rangle)$. Red circles represent case C350F, black squares represent case C350B, green asterisks represent case WC350F, and magenta diamonds represent case WC350B. Solid lines indicate total stress while the blue dashed line represents equation 3.29. Dashed horizontal line marks the location of the top of the roughness elements (k_c^+) on both the panels.

and Reynolds stress $\left(-\langle\widetilde{u_1'u_3'}\rangle\right)$ are shown in figure 3.11. Both wave-current cases show similar wave-phase dependence with varying degrees of attenuation as a function of wave-phase and distance away from the wall. Consistent with the time- and planform-averaged rms profiles in figure 3.11, case WC350B shows slightly lower levels of TKE throughout the wave cycle when compared to case WC350F. The TKE peaks during the deceleration $\left(\frac{d}{dt}U_b\sin(\omega t) < 0\right)$ portion of the wave cycle similar to the experimental studies by Hino et al. (1976) and Fishler and Brodkey (1991). As detailed by Bae and Lee (2021), these enhanced TKE levels are indicative of bursting events that transport the TKE away from the wall, as bursting is associated with strong turbulent ejection events (second quadrant events in the u_3' vs. u_1' plot). Figure 3.12 shows the difference between the second quadrant ejection events that are characteristic of the streak lifting or breakdown events. Here $A_1A_3 = (u_1'|u_1' < 0)(u_3'|u_3' > 0)$ is the conditional product that is time- and planform-averaged for the two wave-current cases. The bumpy wall case shows elevated $\langle\overline{A_1A_3}\rangle$ magnitudes when compared to

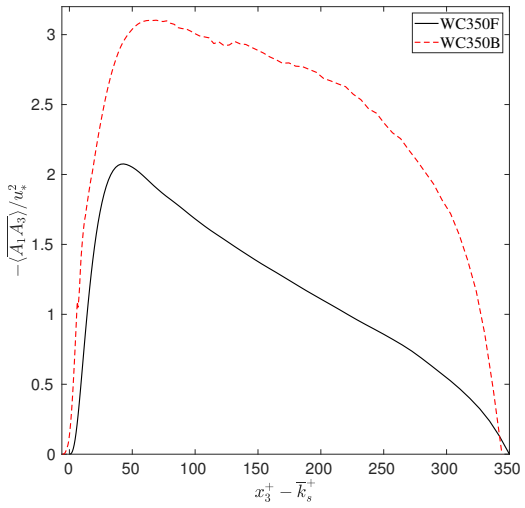

Figure 3.12: Time- and planform-averaged conditional product of the streamwise and vertical turbulent velocity component ($u_1' u_3'$) comparison for the flat and bumpy wall wave-current cases.

the flat wall case, and these events are concentrated during the deceleration portion of the wave cycle (not shown).

Once the TKE within the roughness elements is enhanced at the expense of the TKE above the roughness elements, it becomes available for conversion to the Reynolds stress. As seen in figure 3.13, the Reynolds stress is larger during the acceleration $\left(\frac{d}{dt}U_b \sin(\omega t) > 0\right)$ part of the wave cycle. This suggests that the enhancements in TKE as a result of the turbulent bursting events in the deceleration wave cycle are transported towards the wall during the accelerating part of the wave cycle. While the TKE enhancement occurs in the effective buffer region (defined earlier), the Reynolds stress enhancements appear to occur mainly outside the buffer layer. This phase evolution supports the life cycle of buffer layer streaks proposed by Bae and Lee (2021), where the turbulent streaks are generated within the buffer layer and transported away from the wall during the ejection events, followed by sweep events that transport the associated TKE towards the wall. However, as Bae and Lee (2021) rightly note, this process can only provide a diagnostic explanation for the

observations presented in figure 3.13.

Interactions between the TKE and Reynolds stress can be analysed with the structure parameter defined as

$$\langle \widetilde{M_r} \rangle = -\frac{\langle \widetilde{u_1' u_3'} \rangle}{\langle \widetilde{u_i' u_i'} \rangle}, \tag{3.30}$$

which is a measure of the efficiency with which the turbulent eddies extract the Reynolds stress from the available TKE (Scotti and Piomelli, 2001). Figure 3.14 shows the phase- and planform-averaged structure parameter comparison for the two wave-current cases (i.e. WC350F and WC350B) normalised by case C350F. Case WC350F shown in figure 3.14(a) exhibits elevated values of $\langle \widetilde{M_r} \rangle$ during the acceleration part of the wave cycle, followed by lower values of $\langle \widetilde{M_r} \rangle$ during the deceleration part of the wave cycle. These wave phase variations occur in a region close to the wall and below $2l_t^+$ (defined in equation 3.16). The enhancement that occurs in $\langle \widetilde{M_r} \rangle$ close to the wall during the acceleration wave phase is not equal in magnitude to that occurring during the deceleration wave phase despite the sinusoidal nature of the wave forcing in equation 4.6. Far from the wall, $\langle \widetilde{M_r} \rangle$ does not vary with the wave phase as it does closer to the wall. As lower values of $\langle \widetilde{M_r} \rangle$ are indicative of non-equilibrium flows (Scotti and Piomelli, 2001), case WC350F exhibits a near wall region $x_3^+ < 2l_t^+$ where the flow is in relative non-equilibrium compared to the outer region $x_3^+ > 2l_t^+$. Since the flow is not in equilibrium within the inner region ($x_3^+ < 2l_t^+$), it affects the non-linear production cycle (Jiménez and Moin, 1991) as the inner region includes the location where peak production occurs ($x_3^+ \approx 11.8$).

As for case WC350B, higher values of $\langle \widetilde{M_r} \rangle$ are generated during the acceleration portion of the wave cycle primarily below the roughness crests and transported above them during the deceleration portion of the wave cycle. Most of the $\langle \widetilde{M_r} \rangle$ enhancements compared to case C350F occur below $2l_t^+$, suggesting that the effect of waves

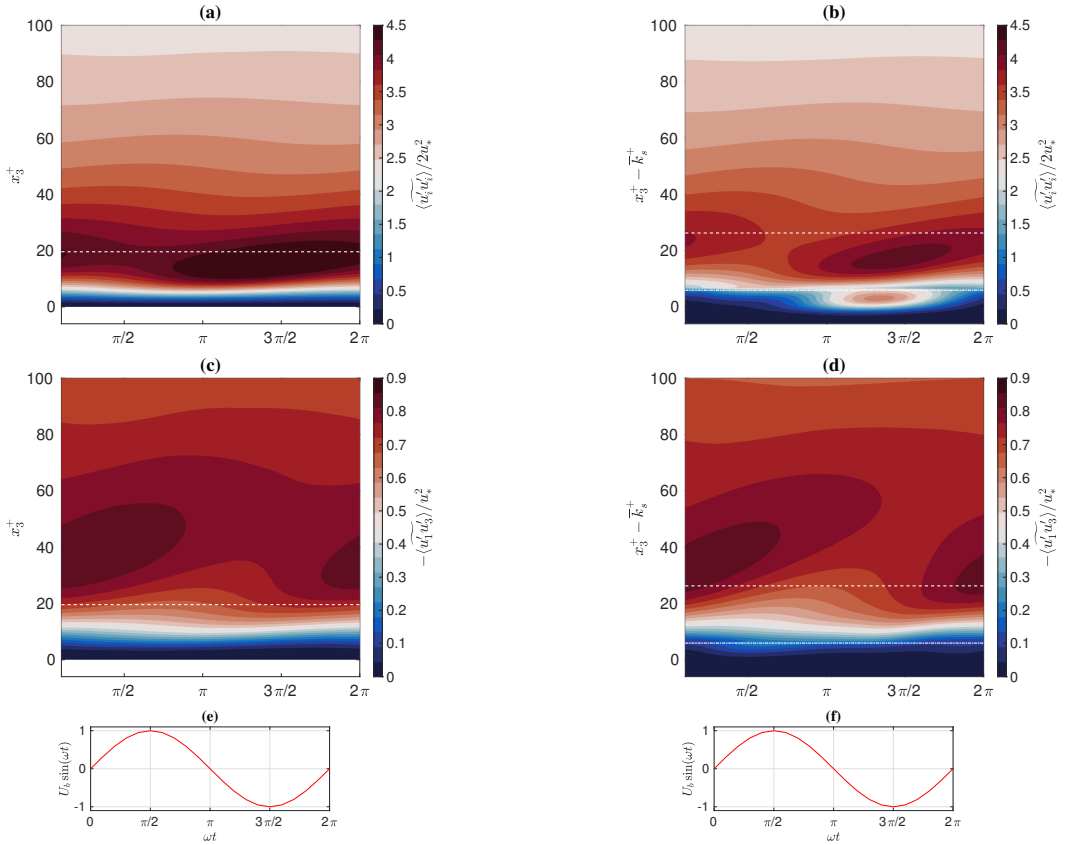

Figure 3.13: Phase- and planform-averaged turbulent kinetic energy (top row) and Reynolds stress (middle row) as a function of height and wave phase. The bottom row shows the wave orbital velocity ($U_b \sin(\omega t)$) which is out of phase with the oscillatory pressure gradient ($U_b \omega \cos(\omega t)$) on the right-hand side of equation 4.6. The left column is the flat wall case WC350F and the right column is the bumpy wall case WC350B. The horizontal dash-dot line marks the roughness crest level (k_c^+) while the horizontal dashed line marks twice the turbulent Stokes length offset above the roughness crest ($2l_t^+ + k_c^+$).

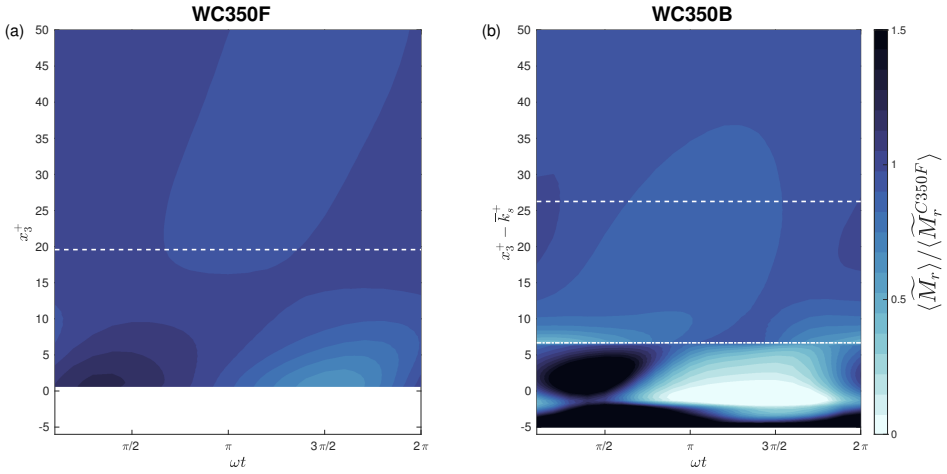

Figure 3.14: Wave phase variations of the normalised structure parameter $\left(\langle \widetilde{M}_r \rangle / \langle \widetilde{M}_r^{C350F} \rangle\right)$ comparing the two wave-current cases (a) WC350F (b) WC350B. The horizontal dashed line marks the roughness crest level, while the horizontal dash-dot line marks twice the turbulent Stokes length offset above the roughness crest $\left(2l_t^+ + k_c^+\right)$.

is confined to a region close to the wall. Similar to case WC350F, case WC350B also exhibits asymmetric $\langle \widetilde{M}_r \rangle$ modifications as a function of wave-phase within the roughness region ($x_3^+ < k_c^+$), with strongly enhanced values during the acceleration phase and strongly attenuated values during the deceleration wave phase. Above the roughness region and below twice the turbulent Stokes length scale ($k_c^+ \leq x_3^+ < 2l_t^+$), minor modifications of $\langle \widetilde{M}_r \rangle$ can be observed with respect to the wave phase and increasing x_3^+. Further away from the wall ($x_3^+ > 2l_t^+$), $\langle \widetilde{M}_r \rangle$ does not change significantly as a function of the wave phase and x_3^+, similar to case WC350F.

The time- and planform-averaged vertical profiles of $\langle \overline{M}_r \rangle$ for the four cases are shown in figure 3.15. It is evident that the time-averaged effects for case WC350F and WC350B are significantly different. Cases C350F and WC350F show similar vertical $\langle \overline{M}_r \rangle$ profiles, while case WC350B shows enhanced $\langle \overline{M}_r \rangle$ values below the roughness crests and twice the turbulent Stokes length scale. This further illustrates the utility of $2l_t^+$ as a length scale that predicts the height below which the effect of waves is

dominant in a wave-current boundary layer type flow. In the outer layer ($x_3^+ > 2l_t^+$), cases WC350F, C350B, and WC350B show reduced values of $\langle\overline{M}_r\rangle$ when compared to case C350F. This suggests that these cases do not effectively convert the available TKE to Reynolds stress in the outer region (or the log-law region) consistent with the observations of Scotti and Piomelli (2001). Comparison of the vertically-integrated $\langle\widetilde{M}_r\rangle$ profile as a function of wave phase within the three regions defined in equations 3.17-3.19 is shown in figure 3.16. Within region I, the vertically-integrated structure parameter for case WC350F is sinusoidal and in-phase with the wave-velocity as seen in figure 3.16. Case WC350B, on the other hand, shows a prominent peak during the acceleration phase, but does not show an equally strong negative peak during the deceleration phase of the wave cycle. This asymmetry leads to a higher $\langle\overline{M}_r\rangle$ for case WC350B when compared to case WC350F in region I. In region II, a similar trend is observed when cases WC350F and WC350B are compared to each other. The phase dependence now is in sync with the driving pressure gradient instead of the wave velocity as observed in region I. One crucial difference between regions I and II is that the phase dependence for case WC350B in region II is sinusoidal. Finally, in region III, the structure parameter is wave-phase independent, and case WC350B shows slightly smaller magnitude when compared to case WC350F. The time- and planform-averaged, vertically-integrated values of the structure parameter ($\langle\overline{M}_r\rangle_v$) shown in table 3.3 further support the net behavior for the four cases under consideration. Both the bumpy wall cases C350B and WC350B show a net increase in the structure parameter within the roughness region (i.e. below the roughness crest $x_3^+ < k_c^+$) at the expense of the other two regions. This is despite the relative increase in $\langle\overline{M}_r\rangle_v$ for cases C350B and WC350B when compared to C350F and WC350F. These results suggest that the effect of waves is confined to a region close to the wall $x_3^+ < 2l_t^+$, while far away from the wall $x_3^+ > 2l_t^+$ there are minor changes observed in the turbulence statistics. Additionally, the strong wave-phase dependence of $\langle\widetilde{M}_r\rangle$

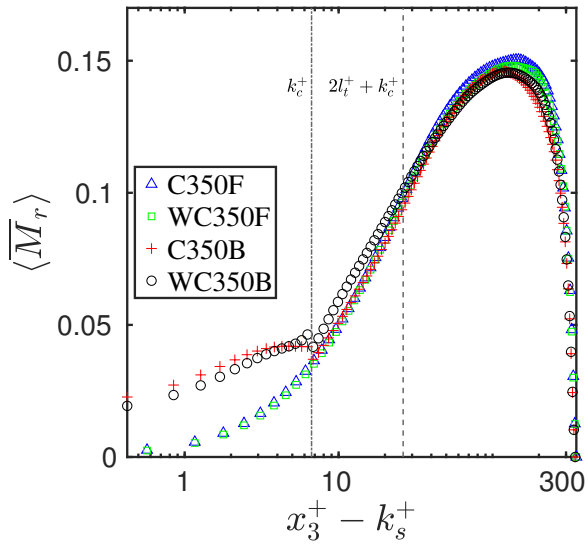

Figure 3.15: Time- and planform-averaged comparison of $\langle \overline{M}_r \rangle$ for the four cases under consideration in this chapter. The vertical dash-dot line represents the roughness crest level while the vertical dashed line represents twice the turbulent Stokes length offset above the roughness crest level ($2l_t^+ + k_c^+$).

for case WC350B when compared to WC350F suggests that the turbulence is out of equilibrium for a portion of the cycle (i.e. acceleration phase) and equilibrates during the deceleration portion of the wave cycle.

3.4.5 Phase-averaged TKE and Reynolds stress budgets

The detailed mechanisms governing the behavior of the structure parameter can be understood by analysing the phase-averaged TKE and Reynolds stress budgets. The phase-averaged Reynolds stress budget for channel flow geometries over bumpy walls can be written as

$$\omega \frac{\partial \langle \widetilde{u_i' u_k'} \rangle}{\partial \theta} = P_s + P_w + P_r + T_k + T_r + T_p + T_v + S_k - \epsilon, \tag{3.31}$$

where the production by mean shear is

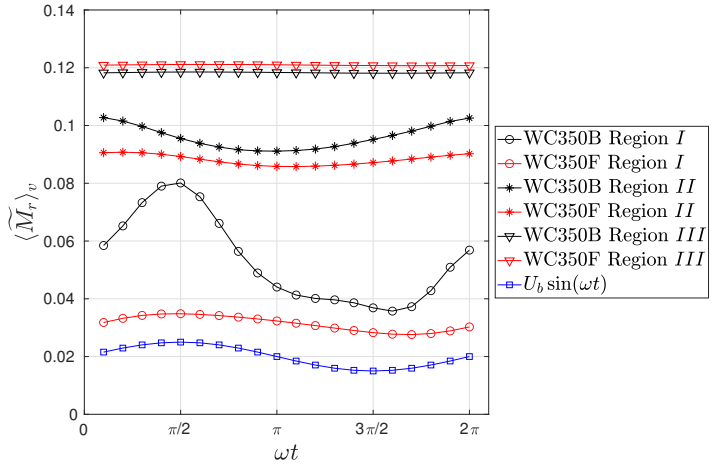

Figure 3.16: Comparison of the time- and planform-averaged, vertically-integrated structure parameter over the three regions for the two wave-current cases as a function of wave phase.

	Region I	Region II	Region III	Total
Case name	$0 \leq x_3^+ < k_c^+$	$k_c^+ \leq x_3^+ < 2l_t^+$	$2l_t^+ \leq x_3^+ < Re_*$	$0 \leq x_3^+ \leq Re_*$
C350F	0.032 (13%)	0.089 (36.5%)	0.123 (50.5%)	0.244 (100%)
WC350F	0.031 (13%)	0.088 (37%)	0.121 (50%)	0.240 (100%)
C350B	0.048 (19%)	0.086 (34%)	0.116 (47%)	0.250 (100%)
WC350B	0.053 (20%)	0.096 (36%)	0.118 (44%)	0.267 (100%)

Table 3.3: Time- and planform-averaged, vertically-integrated structure parameter (M_r) comparison across three regions. The first region is below the top of the roughness elements (k_c^+), the second region is between the top of the roughness elements and twice the turbulent Stokes length scale (l_t^+) defined in equation 3.16, and the third region is above $2l_t^+$. The percentages next to the numerical values represent the contribution of the corresponding region towards the total value.

$$P_s = -\langle\widetilde{u_i'u_3'}\rangle\frac{\partial\langle\overline{u}_k\rangle}{\partial x_3} - \langle\widetilde{u_k'u_3'}\rangle\frac{\partial\langle\overline{u}_i\rangle}{\partial x_3}, \tag{3.32}$$

the production by wave shear is

$$P_w = -\langle\widetilde{u_i'u_3'}\rangle\frac{\partial\langle\widetilde{u}_{w,k}\rangle}{\partial x_3} - \langle\widetilde{u_k'u_3'}\rangle\frac{\partial\langle\widetilde{u}_{w,i}\rangle}{\partial x_3}, \tag{3.33}$$

the production by roughness-induced fluctuations on mean dispersive shear is

$$P_r = -\left\langle\left(\widetilde{u_k'u_j'}\right)_r\frac{\partial\widetilde{u}_{i,r}}{\partial x_j}\right\rangle - \left\langle\left(\widetilde{u_i'u_j'}\right)_r\frac{\partial\widetilde{u}_{k,r}}{\partial x_j}\right\rangle, \tag{3.34}$$

the turbulent transport is

$$T_k = -\frac{\partial}{\partial x_3}\langle\widetilde{u_i'u_k'u_3'}\rangle, \tag{3.35}$$

the dispersive transport is

$$T_r = -\frac{\partial}{\partial x_3}\langle\widetilde{u_i'u_k'\widetilde{u}_{r,3}}\rangle, \tag{3.36}$$

the pressure transport is

$$T_p = -\frac{1}{\rho_0}\frac{\partial}{\partial x_3}\left[\langle\widetilde{u_k'p'}\rangle + \langle\widetilde{u_i'p'}\rangle\right], \tag{3.37}$$

the viscous-diffusion is

$$T_v = \nu\frac{\partial^2}{\partial x_3^2}\langle\widetilde{u_i'u_k'}\rangle, \tag{3.38}$$

the pressure-strain rate correlation is

$$S_k = \frac{1}{\rho_0}\left[\left\langle\widetilde{p'\frac{\partial u_i'}{\partial x_k}}\right\rangle + \left\langle\widetilde{p'\frac{\partial u_k'}{\partial x_i}}\right\rangle\right], \tag{3.39}$$

the dissipation is

$$\epsilon = 2\nu \left\langle \widetilde{\frac{\partial u_i'}{\partial x_j} \frac{\partial u_k'}{\partial x_j}} \right\rangle, \tag{3.40}$$

and θ is the wave phase. The dispersive terms are similar to those derived in the energetic budgets by Raupach et al. (1991), Mignot et al. (2009), and Yuan and Piomelli (2014). Note that eliminating the dispersive transport and dispersive production terms recovers the flat-wall TKE and Reynolds stress budget.

TKE budget

As discussed in Section 3.4.5, the time- and volume-averaged TKE equation can be obtained from equation 3.31 by setting $i = k$ to give a balance between shear production $\langle \overline{P}_s \rangle_v$ and dissipation $\langle \overline{\epsilon} \rangle_v$. For the flat wall wave-current cases, Scotti and Piomelli (2001) found that the evolution of TKE is primarily governed by the changes in $\langle \widetilde{P}_s \rangle$ and $\langle \widetilde{\epsilon} \rangle$. Thus, comparison of $\langle \widetilde{P}_s \rangle$ and $\langle \widetilde{\epsilon} \rangle$ across the four cases can help explain the $\langle \widetilde{M}_r \rangle$ evolution discussed in the previous section. Figure 3.17(a) shows the time- and planform-averaged shear production over dissipation profiles (i.e. $\langle \overline{P}_s \rangle / \langle \overline{\epsilon} \rangle$) for the four cases under consideration. Case C350F has peak production at $x_3^+ \approx 11.6$ as can be shown using the analytic form of the shear production and dissipation for steady channel flows (Pope, 2000). Within the log-law region (i.e. $80 \lessapprox x_3^+ \lessapprox 200$) where shear production is balanced by dissipation, this ratio has a value of unity, while further away from the wall, the ratio decreases due to the presence of a wake region near the free-slip surface (i.e. at $x_3^+ = Re_*$). The flat wall wave-current case WC350F closely follows case C350F except in the region where peak production occurs. The $\langle \overline{P}_s \rangle / \langle \overline{\epsilon} \rangle$ value shows slight attenuation in the peak production region when compared to case C350F. As seen in figure 3.17(b), this attenuation for case WC350F is a result of a minor enhancement of the dissipation when compared to case C350F. Further

away from the wall, case WC350F follows case C350F identically. The bumpy wall cases C350B and WC350B show substantial differences in the shear production and dissipation profiles. Cases C350B and WC350B show significantly attenuated $\langle \overline{P}_s \rangle / \langle \overline{\epsilon} \rangle$ values below the location of peak production (i.e. $x_3^+ \approx 11.8$). Far away from the wall, both cases follow their flat wall counterparts. These differences in the $\langle \overline{P}_s \rangle / \langle \overline{\epsilon} \rangle$ profiles are mainly attributed to the enhanced time-averaged dissipation for both bumpy wall cases. As seen in figure 3.17(b), the location of the peak in magnitude of $\langle \overline{\epsilon} \rangle$ for the bumpy wall cases is just below the top of the roughness elements (i.e. k_c^+). The addition of waves in case WC350B accentuates the effect of the bumps, as indicated by the further decrease in $\langle \overline{P}_s \rangle / \langle \overline{\epsilon} \rangle$ when compared to case C350B. In both bumpy wall cases, the presence of roughness elements shifts the peak production further away from the wall in addition to enhancing dissipation below the peak production region. The additional decrease in $\langle \overline{P}_s \rangle / \langle \overline{\epsilon} \rangle$ for case WC350B is due to a substantial increase in the time-averaged dissipation within the roughness region ($x_3^+ \leq k_c^+$) in comparison to case C350B. These changes lead to substantial reduction in the efficiency with which the available TKE is converted to Reynolds stress as shown in Section 3.4.4.

Wave-phase variations of the ratio of shear production to dissipation across the three regions defined in equations 3.17-3.19 are shown in figure 3.18. The largest variations in $\langle \widetilde{P}_s \rangle / \langle \widetilde{\epsilon} \rangle$ as a function of wave-phase are observed in region II followed by region I and region III, respectively. Starting with region III which is furthest from the wall, cases WC350B and WC350F are roughly the same order of magnitude with case WC350B showing slightly larger magnitude. As most of the production and dissipation is concentrated in regions I and II, the variations of $\langle \widetilde{P}_s \rangle^{(III)} / \langle \widetilde{\epsilon} \rangle^{(III)}$ are in phase with the wave velocity ($U_b \sin(\omega t)$) and peak at $\theta = \pi/2$ showing nearly periodic behavior as a function of the wave phase. The value of $\langle \widetilde{P}_s \rangle^{(III)} / \langle \widetilde{\epsilon} \rangle^{(III)}$ is less than 1 due to the presence of a wake region just above the log-law region close to the channel surface (at $x_3^+ = Re_*$). Closer to the wall in regions I and II,

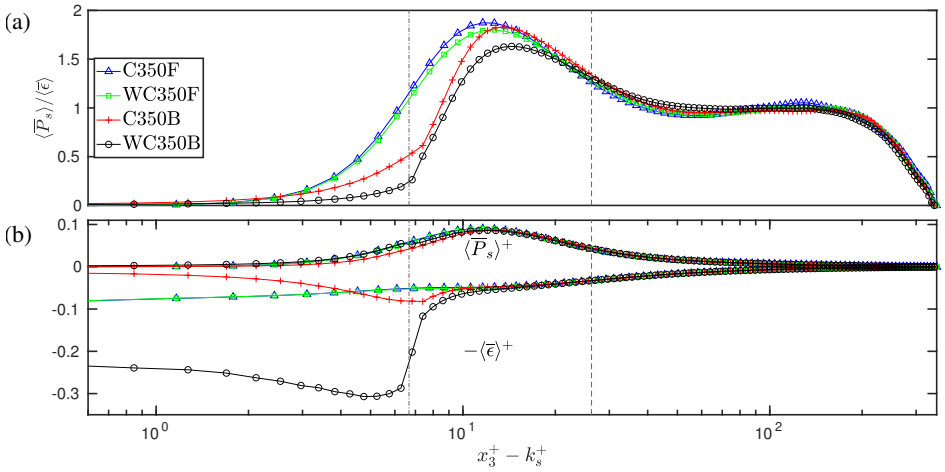

Figure 3.17: (a) Time- and planform-averaged shear production over dissipation comparison for the four cases. (b) Time- and planform-averaged profiles of shear production and dissipation normalised by $u_*^4/(\kappa\nu)$. The vertical dash-dotted line marks the top of the roughness elements (k_c^+) and the vertical dashed line marks $2l_t^+ + k_c^+$.

$\langle \widetilde{P}_s \rangle / \langle \widetilde{\epsilon} \rangle$ is less sinusoidal, especially for the bumpy wall cases. The phase variations in regions I and II can be understood by comparing the phase variations of shear production and dissipation shown in panels (a), (b), (e), and (f) of figure 3.19. The phase variations in shear production are due to phase-variations in the Reynolds stress ($\langle \widetilde{u_1' u_3'} \rangle$). Consequently, the elevated dissipation levels for case WC350B in regions I and II contribute to the suppression of $\langle \widetilde{P}_s \rangle / \langle \widetilde{\epsilon} \rangle$. Additionally, for case WC350F, the peak values in regions I and II are in phase with the wave velocity and occur at the same location. However, case WC350B leads case WC350F in region II by $\pi/4$ while it lags case WC350F in region I, also by $\pi/4$. One possible explanation for this behavior is the phase variation of dissipation which is significantly different for the two wave-current cases. However, the exact mechanisms leading to this behavior are beyond the scope of this dissertation.

The phase variability of $\langle \widetilde{P}_s \rangle / \langle \widetilde{\epsilon} \rangle$ can be quantified by studying the phase variations of the dominant terms in the TKE budget as shown in figure 3.19. As indicated in panels (a) and (b), case WC350B shows a smaller wave-cycle region over which the

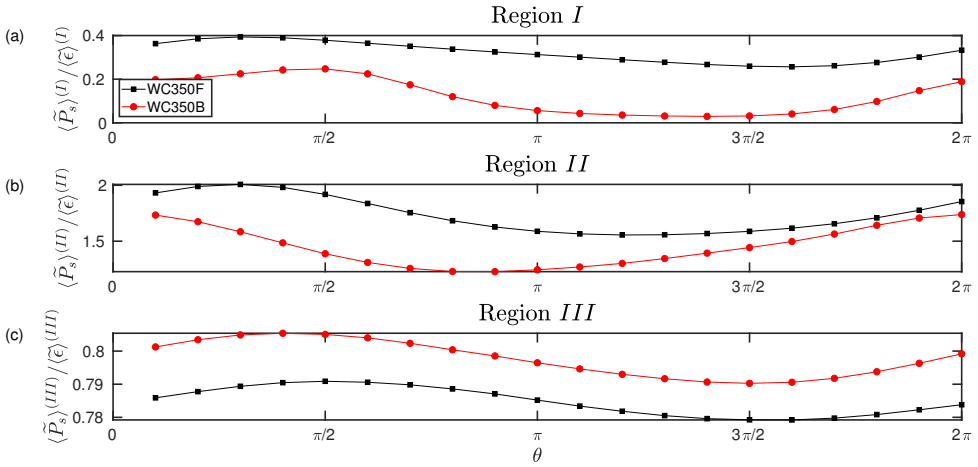

Figure 3.18: Phase- and region-averaged production to dissipation ratio with panels (a), (b), and (c) corresponding to regions I, II, and III, respectively. Note that each of the panels have different scales in the y-axis.

peak production occurs when compared to case WC350F. Additionally, shear production peaks slightly later in the wave cycle for case WC350B when compared to case WC350F. This behavior confirms the slightly reduced shear production magnitudes observed in the time-averaged profiles shown in figure 3.17(b). As discussed earlier, these phase variations suggest that most of the changes observed in $\langle \widetilde{P}_s \rangle / \langle \widetilde{\epsilon} \rangle$ are dominated by the phase variations in dissipation. Panels (e) and (f) in figure 3.19 compare the dissipation for case WC350B and WC350F, and clearly show the large differences. During the acceleration portion of the wave cycle, dissipation occurs primarily just above the top of the roughness elements (k_c^+) for case WC350B. However, during the deceleration portion of the wave cycle, substantial enhancements in dissipation are observed for case WC350B below the top of the roughness elements when compared to case WC350F. In region II (i.e. the buffer layer) similar magnitudes of dissipation are observed for both cases, and far away from the wall (i.e., region III) they are identical. Panels (c) and (d) indicate significant differences in the pressure transport of TKE between cases WC350B and WC350F, implying that pressure transport plays a major role for case WC350B near the wall. Additionally, the changes observed in

$\partial k/\partial\theta$ are confined to a near-wall region as indicated in panels (g) and (h). These results suggest that most of the modifications in TKE occur in a region below the top of the roughness elements for case WC350B. Furthermore, the effects of waves are confined to a region below twice the turbulent Stokes length, while the region far from the wall behaves identically for cases WC350B and WC350F and appear to be dynamically decoupled from the near-wall region. These results support the two-layer model proposed by Townsend (1976) for steady boundary layer flows, in which the region with the highest production (i.e., the buffer layer) is dynamically decoupled from the region far from the wall (i.e., the log-law region).

Vertical Reynolds stress budget

The vertical Reynolds stress budget can be derived by setting $i = 1$ and $k = 3$ in equation 3.31. Since the vertical Reynolds stress (hereafter Reynolds stress) contributes to the total shear stress for the channel geometry, studying the Reynolds stress as a function of wave-phase and x_3^+ can provide a great deal of insight into the mean statistics observed in the previous sections. For hydraulically-smooth, steady turbulent boundary layers, Yuan and Piomelli (2014) showed that the relative magnitude of some of the Reynolds stress budget terms is small, and thus, similar to the TKE budget, not all terms have significant phase variability. Consequently, the phase-variations of the Reynolds stress, turbulent transport, dispersive transport, viscous diffusion, and dissipation terms will not be presented in this section for the sake of brevity. We note that for higher roughness Reynolds number, it may not be justified to neglect some of the terms. After ignoring the terms listed above, the time- and planform-averaged Reynolds stress budget simplifies such that the pressure-strain rate correlations balance the production of Reynolds stress (Pope, 2000). As detailed by Lumley (1975) and Hao and Gorlé (2020), the role of the pressure-strain rate correlations (hereafter

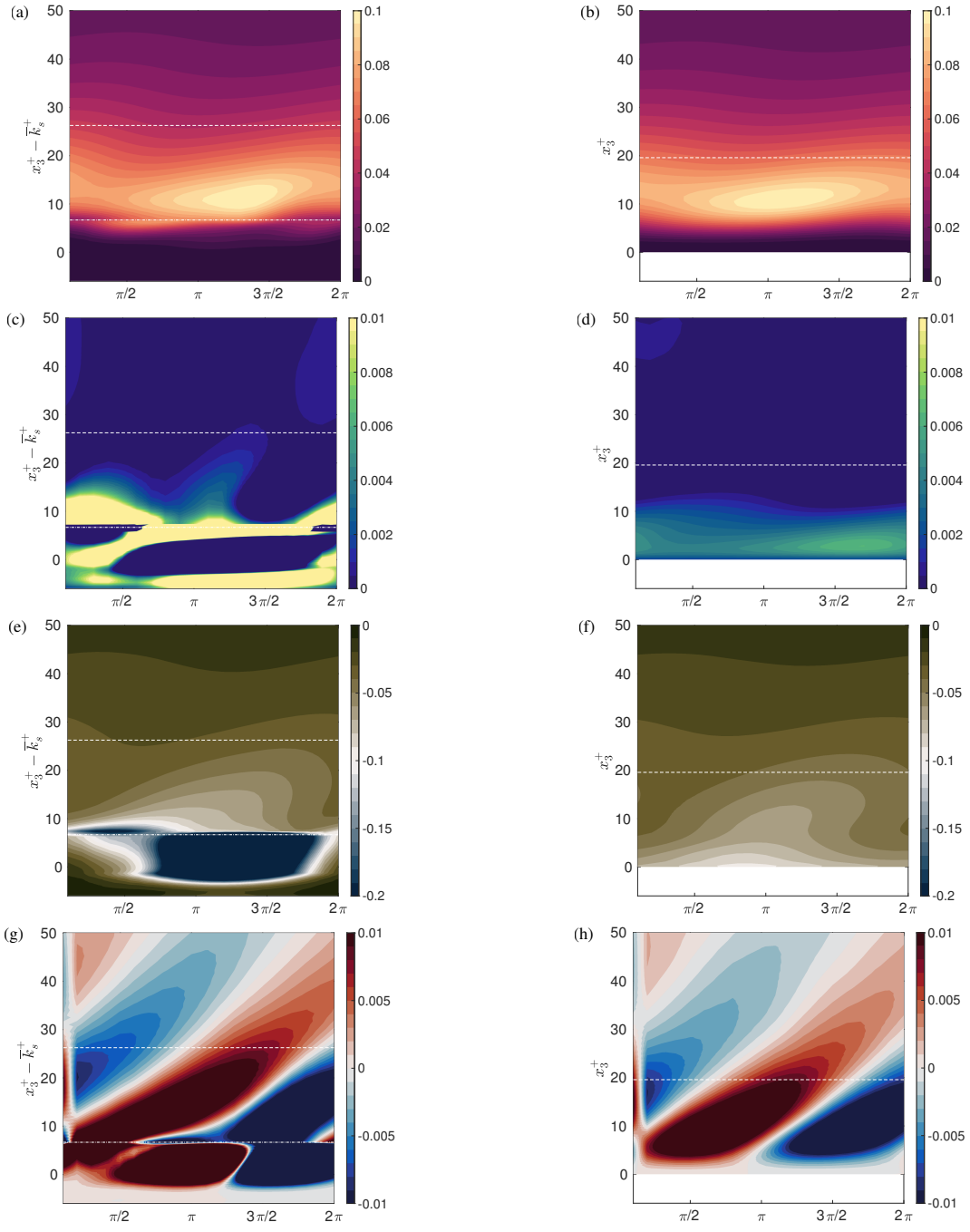

Figure 3.19: Phase variability of the dominant terms in the TKE budget. Panels (a) through (h) show a side-by-side comparison of cases WC350B and WC350F of the shear production (a,b), pressure transport (c,d), dissipation (e,f), and phase rate of change of TKE (g,h), respectively. For each of the pairs, the left panels correspond to case WC350B while the right panels correspond to case WC350F. All terms are normalised by $u_*^4/(\kappa\nu)$. The values indicated on the colorbar are clipped at the maximum and minimum values observed for case WC350F for comparison. The dash-dot line marks the top of the roughness elements (k_c^+) while the dashed line marks the turbulent Stokes length offset above the roughness elements (i.e. $2l_t^+ + k_c^+$).

pressure-strain) is to disorganise the turbulent eddy structures resulting in decorrelation between the streamwise and the vertical turbulent flow components, i.e., they act as a sink term in the Reynolds stress budget. Another perspective on pressure-strain rate correlations is provided by Brasseur and Lee (1989), who interpret the role of the pressure-strain rate correlations as strong local inter-component transfer of energy associated with vortical structures. As seen in the rms velocity profiles in figure 3.11, the role of pressure-strain is evident as the vertical and spanwise turbulent velocities are accentuated at the expense of the streamwise component for the bumpy wall cases C350B and WC350B.

As shown in figure 3.20, case WC350B shows enhanced pressure-strain rate $\left(\overline{S}_{1,3}\right)$ and production of Reynolds stress by mean shear $\left(\overline{P}_{1,3}\right)$ when compared to case WC350F. The peak value of $\overline{S}_{1,3}$ and $\overline{P}_{1,3}$ occurs at the top of the roughness elements for case WC350B, while $\overline{S}_{1,3}$ and $\overline{P}_{1,3}$ both peak within the buffer layer region for case WC350F. Most of the changes observed occur in the vicinity of the wall for case WC350B when compared to case WC350F, while far from the wall, the two wave-current cases have identical behavior. The enhanced rms spanwise and vertical velocity profiles observed in figure 3.13(b) can be explained by the enhanced pressure-strain rate terms near the wall (not shown) as observed by Huang et al. (2021). Since $\langle\widetilde{u_3'u_3'}\rangle\partial\langle\widetilde{u}_1\rangle/\partial x_3$ is a source term in the evolution equation for $-\langle\widetilde{u_1'u_3'}\rangle$, the enhancements of turbulent flow components explains the elevated stress in the wave-current boundary layer.

Panels (a) and (b) in figure 3.21 compare the production of Reynolds stress by mean shear and show higher production during the deceleration portion of the wave cycle. As the TKE peaks during the deceleration portion of the wave cycle, the available $\langle\widetilde{u_3'u_3'}\rangle$ is relatively higher with $\partial\langle\overline{u}_1\rangle/\partial x_3$ being constant. Thus, the net production by mean shear is highest during the deceleration portion of the wave cycle. Panels (e) and (f) compare the Reynolds stress production by wave shear for

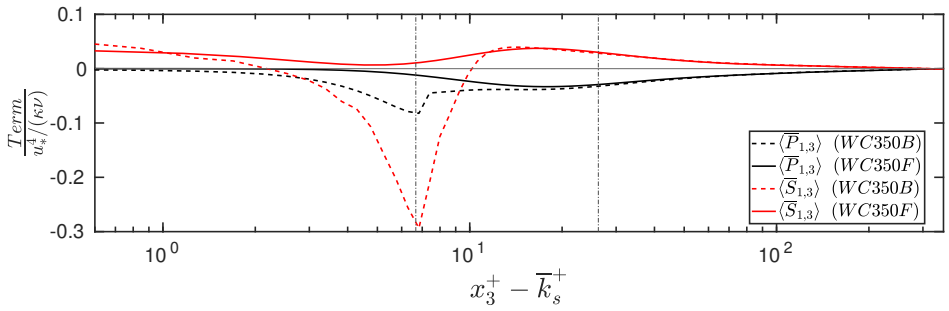

Figure 3.20: Time- and planform-averaged comparison of production of Reynolds stress by mean shear $\left(\langle \overline{P}_{1,3} \rangle\right)$ and pressure-strain $\left(\langle \overline{S}_{1,3} \rangle\right)$ for cases WC350F and WC350B.

cases WC350B and WC350F. Opposing behavior is observed for the wave shear based production, as the values during the acceleration portion of the wave cycle near the wall are negative, i.e., Reynolds stress production by wave shear is negative, while during the deceleration portion positive values are observed suggesting the opposite. It is clear to see that both production mechanisms are significantly enhanced for case WC350B when compared to case WC350F. Similar observations can be made for the pressure transport and pressure-strain rate terms. It is important to note that most of the differences observed are confined to a near-wall region for case WC350B.

3.5 Conclusions

We studied wave-current boundary layer dynamics in current-dominated flow conditions over roughness elements for hydraulically smooth walls to understand the flow drag and energetics. It was found that, although there is negligible flow separation over the hydraulically smooth roughness elements, their presence leads to an increased drag coefficient for the wave-current boundary layer when compared to the steady boundary layer case with identical roughness elements. However, for identical wave forcing conditions, the flat wall case does not undergo any perceptible change

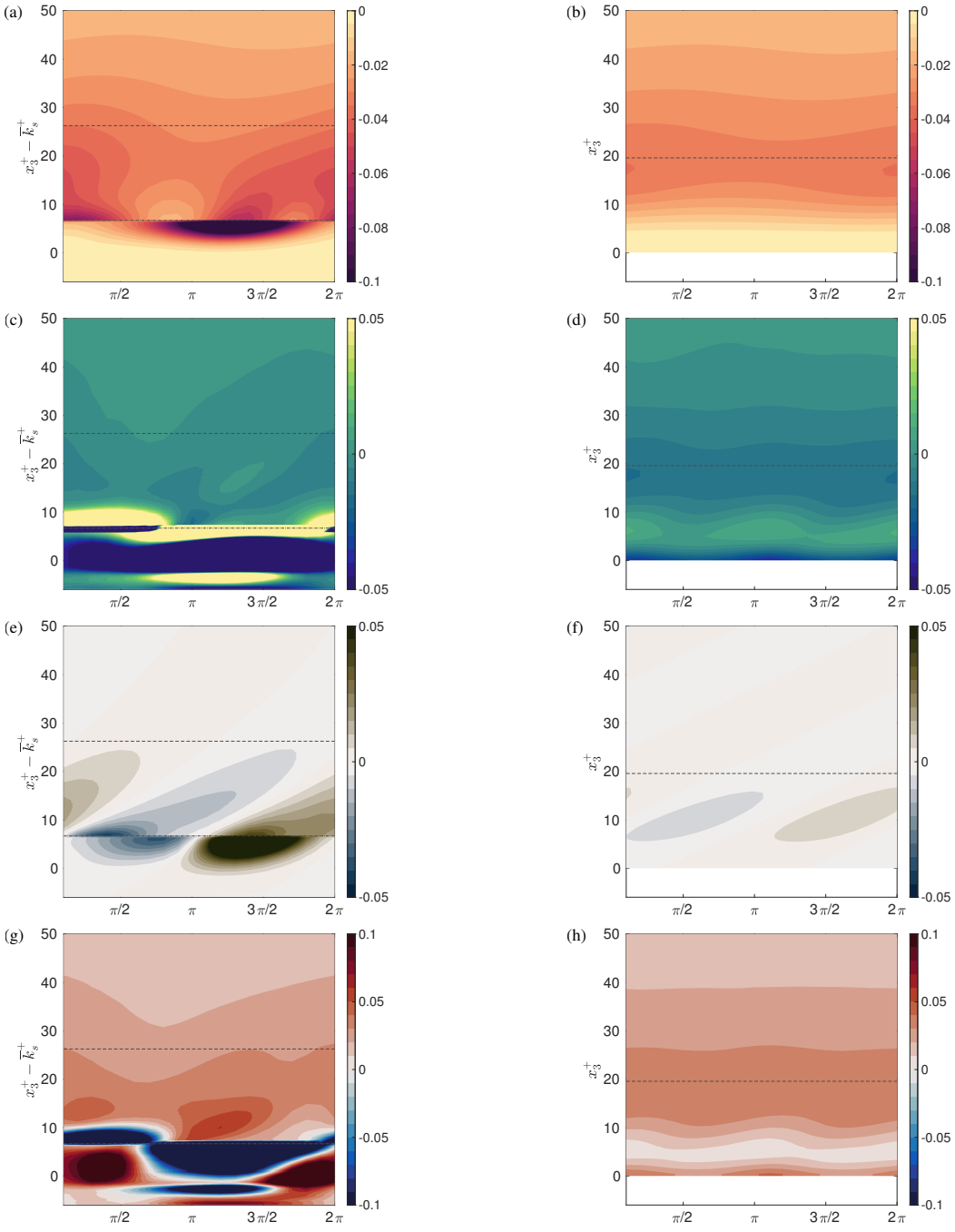

Figure 3.21: Phase variability of the dominant terms in the Reynolds stress budget, namely the shear production (a,b), pressure transport (c,d), production by wave shear (e,f), and pressure-strain (g,h). The left panels correspond to case WC350B while the right panels correspond to case WC350F. All terms are normalised by $u_*^4/(\kappa\nu)$. The values indicated on the colorbar are clipped at the maximum and minimum values observed for case WC350F for comparison. The dash-dot line marks the top of the roughness elements (k_c^+) while the dashed line marks the turbulent Stokes length offset above the roughness elements (i.e. $2l_t^+ + k_c^+$).

in the mean velocity profile when compared to its steady boundary layer counterpart. Despite the three disparate time scale processes i.e., mean flow, waves, and turbulence, the three components are decoupled, suggesting that there is minimal interaction between the wave and the turbulent components for current-dominated flow regimes. However, there seems to exist a one-way coupling such that the waves modulate the turbulence, but not vice-versa. Comparison of the drag coefficients suggests a drag enhancement of $3\% - 11\%$ (depending on the drag coefficient formulation used i.e., equation 3.26 or equation 3.27) when adding waves to the steady case with bumpy walls.

Comparison of the total stress profiles suggests that above the top of the roughness elements, the total stress profile is linear, as expected for steady turbulent channel flows. Comparison of the rms velocity profiles suggests that the presence of roughness elements significantly alters the streamwise nearwall component, but shows slight enhancement away from the wall. As for the other two normal stresses, opposite trends are observed when compared to the steady and wave-current turbulent boundary layer flows over flat walls and steady turbulent boundary layer flows over bumpy walls. These observations suggest that the role of pressure transport and pressure-strain rate for the bumpy wall cases can be significant even for weak wave conditions.

The phase-variations in the TKE and Reynolds stress provide a diagnostic process based explanation of the differences observed in the drag coefficient. During the acceleration portions of the wave cycle, the available TKE is more readily converted to Reynolds stress for the bumpy wall case when compared to the flat wall case. During the deceleration portion of the wave cycle, dissipation intensive turbulent bursting processes lead to a reduction in the Reynolds stress. Most of the alterations observed in the bumpy wall case occur below the top of the roughness elements and between the top of the roughness elements and the turbulent Stokes length.

Phase-dependent TKE budget analysis supports the diagnostic mechanism of drag

enhancement observed with the variations of TKE and Reynolds stress. Observing the ratio of production and dissipation of TKE suggests that there is strong attenuation in the net production for the wave-current bumpy wall case when compared to the flat wall cases. Away from the wall, no significant differences were observed between the four cases discussed in this investigation. The TKE budget phase variations for the bumpy wall cases show strong variations for most of the terms, while the flat wall wave-current case shows minimal changes. The Reynolds stress budget, on the other hand, reveals strong changes in the pressure transport and pressure-strain rate terms for the wave-current bumpy wall case. However, the flat wall cases show minimal to no changes in the Reynolds stress budget.

To summarise, our results suggest that the addition of a weak wave over a steady turbulent current for flat walls does not significantly alter the flow. However, addition of a weak wave over turbulent currents with bumpy walls acts to enhance the drag coefficient. These results have implications for the development and application of wave-current models for estuarine flow conditions. While simple eddy-viscosity wave-current models imply similar consequences for transitional and turbulent wave flow conditions (Grant and Madsen, 1979), the results in this study suggest that such a drag enhancement is also observed for hydraulically smooth, current-dominated flow conditions in the presence of roughness elements. As the drag coefficient is used to model estuarine sediment transport, large-scale variability in the prediction of drag coefficients can drastically change the outcomes of simpler wave-current turbulence models even in current-dominated flow conditions like those discussed in this study.

Chapter 4

Turbulence dynamics and the eddy-viscosity model in wave-dominated, wave-current boundary layers

4.1 Abstract

Estuarine environments play a critical role in supporting some of the most vital components of natural ecosystems such as benthic organisms, corals, coastal anthropogenic activities and marine life, just to name a few. The hydrodynamics in these coastal regions is driven by a combination of different driving agents such as mean currents, gravity waves, bottom bathymetry and organic content in the fluid. Using a turbulence-resolving computational framework, we present the effect of bottom roughness on a wave-current boundary layer in the wave-dominated (wave to current driven ratio of 1.25) flow regime. The turbulent, wave-current channel flow has a friction Reynolds number of 350 and a wave Reynolds number of 4780. At the lower boundary, we introduced a bumpy wall using a direct forcing immersed boundary method, while the top wall has a free-slip boundary condition. We also present a comparison with identical flow conditions over flat walls to quantify the

difference between the flat and the bumpy wall cases. Results suggest that the addition of a transitionally turbulent wave to a turbulent mean current over a flat wall decreases the time-averaged TKE production in the channel flow with a simultaneous (minor) increase in the TKE dissipation magnitude. This leads to a time-averaged faster flow condition when compared to the turbulent channel flow without any wave forcing. On the other hand, the wave-current boundary layer case with a bumpy wall shows the exact opposite behavior, where the time-averaged mean current slows down. By analysing the Reynolds stress and dissipation anisotropy tensor, we establish the return to isotropy mechanism that is dynamically distinct for the bumpy wall, wave-current case that enables modeling the wave-current boundary layer using an eddy-viscosity type model like that of Grant and Madsen (1979).

4.2 Introduction

The dominant driving mechanisms such as tidally and wave-driven mean currents, oscillatory wave motion, bottom bathymetry and sediment induced stratification (to list a few) determine the long-term fate of an estuary as they govern the hydrodynamic, morphodynamic and bio-geological response of the estuarine bottom boundary layer (EBBL). As a result, understanding the effect of varying combinations of the driving mechanisms can provide necessary insights in improving the prediction capabilities of large scale coastal ocean models viz., SUNTANS (Fringer et al., 2006), SWASH (Zijlema et al., 2011), Delft3D (https://oss.deltares.nl/web/delft3d) etc., as they heavily rely on parameterisations for sub-grid scale processes both in space and time. Along with the driving mechanisms, changing boundary conditions viz., rising sea levels, anthropogenic activities, benthic processes etc., may also significantly alter the state of the EBBL, consequently affecting its hydrodynamic and morphodynamic response. For example, Egan et al. (2020a) found that *Sabaco elongatus* worm

tubes significantly modified the bottom boundary conditions in the San Francisco Bay estuary seasonally as observed by Lacy and MacVean (2016), thus impacting the hydrodynamic behavior of the bottom boundary layer.

Tidally- or wave-driven turbulent mean flows interacting with oscillatory wave motions over naturally rough bottom bathymetry are characteristic features of such EBBLs. The morphodynamic response is often parameterised by prescribing the bed shear stress that governs the net erosion and sedimentation (Nielsen, 1992) using a quadratic drag law given by

$$\tau_b = \frac{1}{2}\rho_0 f_{cw} U^2, \tag{4.1}$$

where, τ_b is the bottom shear stress, ρ_0 is the fluid density, f_{cw} is the wave-current friction factor and U is the maximum wave orbital velocity. A quick comparison of the boundary layer thickness for pure wave motion ($\delta_w \equiv \sqrt{2\nu/\omega} \approx 0.1$ mm for a wave with a period of 3 s) versus a pure mean turbulent current ($\delta_c \equiv 11.6\nu/u_*^c \approx 1$ mm for $Re_* = 10^3$) suggests that the velocity gradient is stronger for the wave boundary layer. Thus, waves provide the necessary bottom stress to erode the sediment, while the mean currents and turbulence enable their transport (Lacy and MacVean, 2016). The parameterisation in equation 4.1 essentially involves determining the right value of f_{cw} for a given combination of driving forces and boundary conditions to accurately predict the shear stress. Consequently, this flow configuration has been extensively studied both experimentally and analytically to understand the behavior of f_{cw} as a function of varying driving mechanisms (Hussain and Reynolds, 1970; Grant and Madsen, 1979; van Doorn, 1981; Kemp and Simons, 1982, 1983; Fredsøe, 1984; Myrhaug and Slaattelid, 1990; Arnskov et al., 1993; Soulsby et al., 1993; Lodahl et al., 1998). Lodahl et al. (1998) carried out an extensive experimental study to characterise flat wall, wave-current boundary layer dynamics for varying wave

Reynolds number $Re_w \equiv U_b^2/(\omega\nu)$, where, U_b is the wave orbital velocity, ω is the wave frequency and ν is the kinematic viscosity of the fluid. They found that the bed shear stress shows two distinct behaviors when the boundary layer is wave dominated i.e., $U_b/U_c > 1$, where U_c is the time- and cross sectionally-averaged velocity. For cases where the steady boundary layer is weakly turbulent, Lodahl et al. (1998) observed non-monotonic reduction in the time-averaged shear stress with increasing Re_w followed by monotonically increasing time-averaged shear stress when the wave boundary layer transitions to a turbulent state. For cases where the steady boundary layer is strongly turbulent, the time-averaged shear stress does not show apparent reduction, but instead monotonically increases with increasing Re_w. These observations have since been validated to show reduced turbulent transport mechanism close to the wall, thereby increasing the mean flow magnitude and decreasing the flow drag in the non-monotonic region (Scotti and Piomelli, 2001; Manna et al., 2012, 2015; Nelson and Fringer, 2018).

Estuaries exhibit naturally rough bottom boundaries, and the roughness varies seasonally and spatially (Egan et al., 2020a). For such bumpy wave-current boundary layers, most if not all studies are restricted to experiments or theory as listed earlier. Two notable exceptions are the studies of Bhaganagar (2008) and Jelly et al. (2020) using direct numerical simulations (DNS) and large-eddy simulations (LES), respectively. Despite these advances, both the computational frameworks make use of regular roughness elements with fixed streamwise and spanwise length scales, thus introducing two additional non-dimensional parameters that may influence the behavior of f_{cw}. Jelly et al. (2020) used cosine-based roughness elements to show that the role of pressure (or form) drag can be significant compared to skin friction drag when the forcing time scale (T_w) is significantly smaller than the eddy turnover time ($T_\epsilon \equiv H/u_*$), where H is the channel depth and u_* is the friction velocity of the mean current. Despite these observations, a detailed understanding of the mechanics that

lead to the enhanced drag have been missing in the literature. A diagnostic mechanism suggesting that the pressure-strain rate correlations re-distribute the streamwise turbulent kinetic energy (TKE) to the other two components has been hypothesised for current-dominated flow conditions, thus leading to excess dissipation (Patil and Fringer, 2022). These observations have provided renewed interest to numerically investigate wave-current boundary layers using turbulence-resolving computational frameworks.

Large-scale coastal ocean models rely on bottom drag parameterisations like the ones proposed in Grant and Madsen (1979) that enable prediction of the hydrodynamics and sediment transport over long time scales. These parameterisations are often developed after making specific assumptions about the flow conditions, thus limiting their range of applicability. Additionally, in-situ observations by Bricker et al. (2005) suggest that the Grant and Madsen (1979) model may lead to larger mean flow drag coefficient predictions mainly as such models do not account for appropriate phase lags between the driving pressure gradient and the boundary layer response (Teixeira and Belcher, 2002). Despite the extensive practical utility of such drag parameterisations (Egan et al., 2019, 2020b; Peruzzi et al., 2021; Davis et al., 2021), some of the fundamental assumptions such as the isotropic nature of the underlying turbulence, time-invariance of the eddy-viscosity, and form of the eddy-viscosity, require further investigation and validation to improve their reliability. To this end, in this study we aim to understand and explain the validity of the drag parameterisation proposed by Grant and Madsen (1979) for wave-dominated, wave-current boundary layer flows. We first present a brief review of the Grant and Madsen (1979) wave-current drag model which is followed by a presentation of the first-order flow statistics and a subsequent analysis. We then discuss the validity of the eddy-viscosity model that is used to develop the Grant and Madsen (1979) wave-current drag parameterisation.

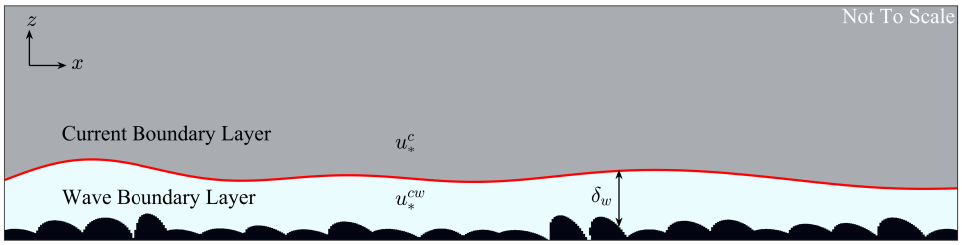

Figure 4.1: Schematic of the two-layer, wave-current boundary layer model developed by Grant and Madsen (1979). Black shading represents the roughness elements, while the red solid line marks the top of the wave boundary layer (δ_w). The grey shading marks the region of the flow that is dominated by mean current dynamics. Here u_*^c is the friction velocity based on the mean flow above the wave boundary layer, and u_*^{cw} is the friction velocity within the wave boundary layer.

4.3 The Grant and Madsen (1979) wave-current bottom drag parameterisation

A succinct theoretical framework for the bottom boundary layer response was first proposed by Grant and Madsen (1979) (hereafter GM79) as a function of wave strength, mean flow strength, bottom roughness and angle between the current and the wave, in wave-dominated flow conditions. In the absence of convective and Coriolis acceleration, GM79 developed a two layer flow model as sketched in figure 4.1 with the governing equation given by

$$\partial_t u = -\frac{1}{\rho_0}\nabla p + \partial_z\left(\frac{\tau}{\rho_0}\right), \tag{4.2}$$

where, $u = u_c + u_w$ is the velocity decomposition and $p = p_c + p_w$ is the pressure decomposition, and the subscript c denotes the mean current and w denotes the wave component. The above governing equation is mathematically unclosed since the form of the stress τ is not known a-priori. GM79 use the eddy-viscosity model $\tau = \nu_t \partial_z u$, where ν_t is the turbulent eddy-viscosity to mathematically close the governing

equations. Very close to the wall, the eddy-viscosity profile is assumed to be linearly proportional to the distance from the wall, viz.

$$\nu_t = \kappa u_* z, \tag{4.3}$$

where κ is the von Kármán constant and u_* is the local friction (or shear) velocity. Note that equation 4.3 is only applicable in the log-law region where the mixing-length is given as $l_m = \kappa z$ (Pope, 2000). For problems involving multiple length scales, the right form of ν_t can be prescribed by choosing the appropriate value of u_*. This approach is used by GM79 to correctly account for the mean velocity gradient within the wave boundary layer and the mean current boundary layer as indicated in figure 4.1. It is important to note that the wave boundary layer is limited by the wave frequency (ω) through a length scale $l \equiv \kappa u_*^{cw}/\omega$. Here u_*^{cw} is friction velocity associated with the wave boundary layer and u_*^c is the friction velocity associated with the region above the wave boundary layer.

Using this simplified model, GM79 solve for the wave and mean current velocity profile inside and outside the wave boundary layer. The wave and mean current solutions obtained using the above analytical model are a function of the wave-current friction factor (f_{cw}) and the enhanced bottom roughness (k_{bc}), that are obtained through solving (numerically) equations (Equation 54 and 49 from Grant and Madsen (1979) respectively)

$$F_1^2 + 2F_1 + \left[\frac{V_2}{2\alpha^{1/4}}\right]\cos\overline{\phi}_c = \frac{\alpha^{3/4}}{4} - \frac{V_2^2}{4\alpha^{1/2}}, \tag{4.4}$$

$$\frac{k_{bc}}{\overline{k}_s} = \left[24\frac{u_*^{cw}}{U_b}\frac{A}{\overline{k}_s}\right]^{1-\frac{u_*^c}{U_b}\frac{U_b}{u_*^{cw}}}, \tag{4.5}$$

where $F_1 = \left[0.097\left(\frac{\overline{k}_s}{A}\right)^{1/2}\frac{K}{f_{cw}^{3/4}}\right]$, K is a factor representing the maximum value of the

wave shear velocity (equation 55 in GM79), V_2 represents the combined effect of the wave to current strength and the angle between the wave and the current (equation 14 in GM79), α is the flow dominance parameter (equation 20 in GM79) and $\overline{\phi}_c$ is angle between the incident wave and the current (equation 17 in GM79). Once f_{cw} is known, the bottom shear stress (τ_b) can be estimated using equation 4.1. A detailed discussion of the GM79 theory can be found in Adelson (2020).

As mentioned earlier, GM79 relies on a variety of assumptions that render the semi-analytical solution tractable. However, some of the assumptions made in GM79 have been shown to be invalid (Sleath, 1987, 1991; Cowherd et al., 2021). Despite the multi-scale (length) nature of the problem, the eddy viscosity (ν_t) and the mixing length (l_m usually proportional to the boundary layer thickness $\sim l$) are assumed to be proportional within the log-law region. Sleath (1991) suggest that this assumption requires the partition of the boundary layer into two regions in-turn forcing the choice of two different shear velocities that set the scale of the eddy viscosity. According to Sleath (1991), this implies that the vertical turbulent velocity component (u_3') is independent of the vertical coordinate (x_3). Additionally, the eddy viscosity and mixing length parameterisations have been traditionally constructed for steady turbulent flows, thus implying the constancy of ν_t with respect to wave-phase variations (ωt) (Prandtl, 1925). Despite these arguments, Sleath (1991) in their model use a time-mean wave eddy viscosity component to account for the wave turbulence and note that the fluctuating component of the wave eddy viscosity ($\widetilde{\nu}_t^w$) is significantly small compared to both the mean current eddy-viscosity (ν_t^c) and time-mean wave eddy-viscosity ($\overline{\nu}_t^w$). However, to account for the possible variations, Sleath (1991) suggests that $\nu_t^w = u_3' l_m$ unlike GM79 who use the linear eddy viscosity model as given in equation 4.3.

Apart from the turbulence modelling choices discussed above, GM79 assume instantaneous bed shear response without any phase lag between U_b outside the wave

boundary layer and τ_b. Cowherd et al. (2021) recently observed that the instantaneous boundary layer response hypothesis may not be true, despite the instantaneous response of the turbulence. The wave forcing is assumed to be monochromatic in frequency space and does not include interactions with turbulent momentum injection from the top of the water column (wave-strain production) as the wave flow component is assumed to be inviscid above the wave boundary layer. Since the wave time scale and the turbulent time scales are generally separated by one order of magnitude, any correlations between the two flow components are assumed to be negligible (Hussain and Reynolds, 1970). However, using an identical framework, Madsen (1994) extended the GM79 theoretical model for a spectrum of waves interacting with a turbulent current.

Despite the above shortcomings, the GM79 wave-current drag parameterisation has proven to be adequate for estuarine environments with significant improvements and additions made to include the effects of stratification (Glenn and Grant, 1987; Styles and Glenn, 2000). Nevertheless, the apparent robustness of the GM79 wave-current drag parameterisation demands renewed investigation using numerical tools that are able to resolve the requisite turbulence dynamics to test the various hypothesis upon which GM79 is based.

4.4 Problem formulation

4.4.1 Governing equations and computational framework

We perform direct numerical simulation (DNS) of wave-current boundary layer flows over flat and bumpy walls in a channel flow configuration using the immersed boundary method (IBM) to simulate the bumps. The governing equations are given by

$$\partial_t u_i + \partial_j(u_j u_i) = -\frac{1}{\rho_0}\partial_i p + \nu\partial_j\partial_j u_i + U_b\omega\cos\omega t\delta_{i1} + \Pi_c\delta_{i1} + F_{\mathrm{IBM}}, \tag{4.6}$$

$$\partial_i u_i = 0, \tag{4.7}$$

where u_i is the velocity vector, t is time, x_j is the Cartesian coordinate vector, δ_{ij} is the Kronecker delta function, ρ_0 is the reference density of the fluid, p is the pressure, ν is the kinematic viscosity, U_b is the maximum wave orbital velocity, ω is the wave frequency, Π_c is the constant pressure gradient driving the flow and F_{IBM} is the immersed boundary force to represent the bumps. Coordinate axes are aligned as x_1, x_2 and x_3 in the streamwise, spanwise and vertical directions, respectively. Periodic boundary conditions are applied in the streamwise and spanwise directions, while a no-slip boundary condition is applied at the bottom wall and a free-slip boundary condition is applied at the top wall to simulate open-channel like geometries. The boundary conditions at the top wall are given by

$$u_3(x_3 = H) = 0, \quad \frac{\partial u_i}{\partial x_3}(x_3 = H) = 0 \quad \forall i \in 1, 2, \tag{4.8}$$

where H is the channel height. The governing equations are solved using the computational framework described in Patil and Fringer (2022).

4.4.2 Computational grid and simulation parameters

The channel has dimensions $2H$, H and H in the streamwise, spanwise and vertical directions, respectively. The one-point turbulent statistics have been shown to converge for $Re_* \leq 4200$ (Lozano-Durán and Jiménez, 2014) for this channel geometry. A constant pressure gradient in equation 4.6 is prescribed as $\Pi_c = u_*^2/H$, where

$u_* = 0.0035$ m/s and $H = 0.1$ m that drives the mean turbulent current. The oscillatory pressure gradient in equation 4.6 is prescribed by fixing $U_b = 0.0775$ m/s and $\omega = 2/T_w$, where $T_w = 5$ s is the wave period. Based on these body forcing conditions, the flow is expected to be in the wave-dominated regime $U_b/U_c = 1.25 > 1$. The bottom boundary can be classified to be in the hydraulically smooth wall flow conditions for the flat wall (also see figure 4.2), while the bumpy wall case is hydraulically transitional based on $\overline{k}_s/\delta_w = 4.82 > 4$, where $\overline{k}_s$ is the mean roughness height and δ_w is the wave boundary layer thickness. The top of the roughness crest ($\overline{k}_c$) is defined as the location where the roughness function is zero (Patil and Fringer, 2022). The mean turbulent friction Reynolds number is $Re_* = u_* H/\nu = 350$ and the wave Reynolds number is $Re_w = U_b^2/(\omega\nu) = 4780$. As shown in figure 4.2 and listed in table 4.1, the red circles correspond to current dominated flow conditions such that the wave boundary layer is hydraulically smooth for these two cases. The blue circles correspond to a wave-dominated flow condition where case WC4780F is hydraulically smooth and case WC4780B21 is transitionally rough. As discussed in Patil and Fringer (2022), the analytical results for Grant and Madsen (1979) can only be obtained for the wave-dominated flow conditions, thus the choice of cases WC4780F and WC4780B21.

For both the bumpy wall cases i.e., CB21 and WC4780B21, the channel is discretised with $768 \times 512 \times 256$ grid points. Uniform grid spacing is used over the bumpy surface (roughness elements) with a resolution of $\Delta x_3^+ = 0.31$, where the plus unit indicates normalisation by wall units, i.e., $\Delta x_3^+ = u_* \Delta x_3/\nu$. Above the roughness crest, the grid is stretched so that the maximum vertical grid spacing at $x_3 = H$ is $\Delta x_{3,max}^+ = 4.3$. Using the maximum instantaneous friction velocity ($u_* = 9.2 \times 10^{-3}$ m/s), the grid has a resolution of $\Delta x_3^+ = 0.81$ over the roughness elements, while above the roughness elements, the grid is stretched until $\Delta x_3^+ = 11.22$. Here the maximum instantaneous friction velocity is estimated using the sum of the

maximum wave orbital velocity and the mean current velocity. For the flat wall case i.e., CF and WC4780F, the channel is discretised with $512 \times 256 \times 92$ grid points. The first vertical grid cell has a height $\Delta x_3^+ = 0.53$ and stretched until $\Delta x_3^+ = 7.45$, where the non-dimensionalisation is presented using the time-averaged friction velocity ($u_* = 3.5 \times 10^{-3}$ m/s). Note that in the following sections the non-dimensionalisation uses the mean friction velocity unless specified otherwise. Uniform grid spacing is used in the streamwise and spanwise directions with $\Delta x_1^+ = 7.52$ and $\Delta x_2^+ = 5.63$ for both the flat and bumpy wall cases. It is important to note that this grid resolution is sufficient for resolving the requisite turbulent features for both the bumpy and flat wall cases as the wave-current boundary layer is not expected to produce turbulence throughout the entire wave cycle. The mean roughness height for the bumpy wall cases is $\overline{k}_s^+ = 21$, based on the time-averaged friction velocity. A time step size of $\Delta t^+ \equiv \Delta t u_*/H = 1.75 \times 10^{-6}$ is used for the bumpy wall cases, and $\Delta t^+ = 1.75 \times 10^{-4}$ for the flat wall case; based on ensuring a maximum Courant number of 0.4 for a total simulation time of 10^3 s or 200 wave periods for the wave-current cases. Simulations are run at the Texas Advanced Computing Cluster on Stampede2 (Intel KNL) using 256 processors. On average, 565, 248 CPU hours are required to simulate 10^3 s of real time. The various flow simulations and parameters are listed in table 4.1.

The flow velocity is decomposed as

$$u_i(x_i, t) = \langle \overline{u}_i \rangle (x_3) + \langle \widetilde{u}_{i,w} \rangle (x_3, t) + u_i'(x_i, t) + u_r(x_i, t), \tag{4.9}$$

where the terms on the right hand side are the time- and planform-averaged velocity, the phase- and planform-averaged wave velocity, turbulent velocity and the dispersive (or roughness) velocity components, respectively. The definitions for the velocity components and the convergence criteria for the turbulent statistics are based on

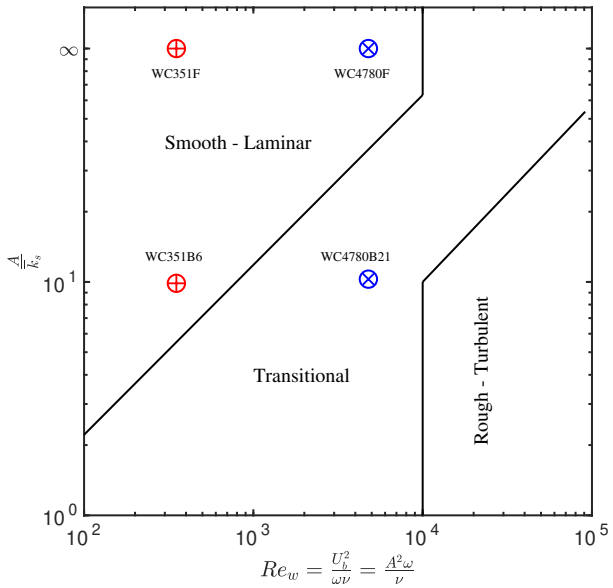

Figure 4.2: Classification of the wave-current boundary layer using the wave flow conditions and the relative roughness. Blue markers with a cross show the simulations that will be discussed in this paper, while the red markers with a plus show the current-dominated boundary layer cases taken from Patil and Fringer (2022). The x axis shows the wave Reynolds number ($Re_w = U_b^2/(\omega\nu)$), where U_b is the maximum wave orbital velocity, while the y axis shows the relative roughness ($A/\overline{k}_s$), where $A = U_b/\omega$ is the wave orbital excursion and $\overline{k}_s$ is the mean roughness height. Adapted from Lacy and MacVean (2016).

Acronym	Description	Re_*	Re_w	$u_*\overline{k}_s/\nu$	$H/\overline{k}_s$	$u_*/(\omega\overline{k}_s)$	U_b/U_c	$\overline{k}_s/\delta_w$
CF	Flat wall channel	350	0	0	0	-	-	-
CB6	Bumpy wall channel smooth	350	0	6	59	-	-	-
CB21	Bumpy wall channel transitional	350	0	21	16.44	-	-	-
WC351F	Flat wave-current weak wave	350	351	0	-	-	0.34	-
WC351B6	Bumpy wall wave-current weak wave	350	351	6	59	1.64	0.34	1.34
WC4780F	Flat wall wave-current strong wave	350	4780	0	-	-	1.25	-
WC4780B21	Bumpy wall wave-current strong wave	350	4780	21	16.44	0.48	1.25	4.82

Table 4.1: The various DNS cases carried out with C denoting the steady channel flow cases, WC denoting the wave-current case, the number between the letters denotes the wave Reynolds number, the letter F denotes the flat wall case, the letter B denotes the bumpy wall case, and the number at the end denotes the roughness Reynolds number. Cases CF, CB6, WC351F and WC351B6 are taken from Patil and Fringer (2022).

the formulations detailed in Patil and Fringer (2022). All statistics presented in the following sections are averaged over 100 wave periods for the wave-current cases and 10 eddy turnovers (H/u_*) for the steady current cases. The convergence history for cases WC4780F and WC4780B21 can be seen in figure 4.3, which shows the deviations of the time rate of change of the turbulent kinetic energy ($\partial_t\langle k\rangle$). The magnitude of $\partial_t\langle k\rangle$ for case WC4780B21 is substantially larger when compared to case WC4780F. Additionally, case WC4780F does not show strong periodic variations in $\partial_t\langle k\rangle$ as seen for case WC4780B21, suggesting that wave motion only weakly modulates the turbulence for case WC4780F. Case W4780F achieves steady-state behaviour around 50 wave periods, while case WC4780B21 achieves steady-state behaviour after 10 wave periods. However, in order to avoid transient effects due to the addition of the oscillatory wave motion, the first 100 wave periods are not included in the statistics. Consequently, all statistics presented in the following sections will be averaged over 100 wave periods after an initial transient of 100 wave periods.

4.5 Results and discussion

4.5.1 Mean and wave-driven velocity profiles

Figure 4.4 shows the time- and planform-averaged velocities for the cases detailed in table 4.1. Cases CF, CB6, WC351F and WC351B6 have been discussed in Patil and Fringer (2022) and are presented here for reference. First, we will compare case WC4780F to the standard flat-wall cases. Case WC4780F follows the linear velocity prediction similar to case CF for $x_3^+ < 6$ as expected. Within the buffer layer ($6 \leq x_3^+ < 30$), the velocity profile deviates from case CF and eventually the log-law region is shifted upwards. The log law for a fully developed (steady) turbulent channel flow is given by

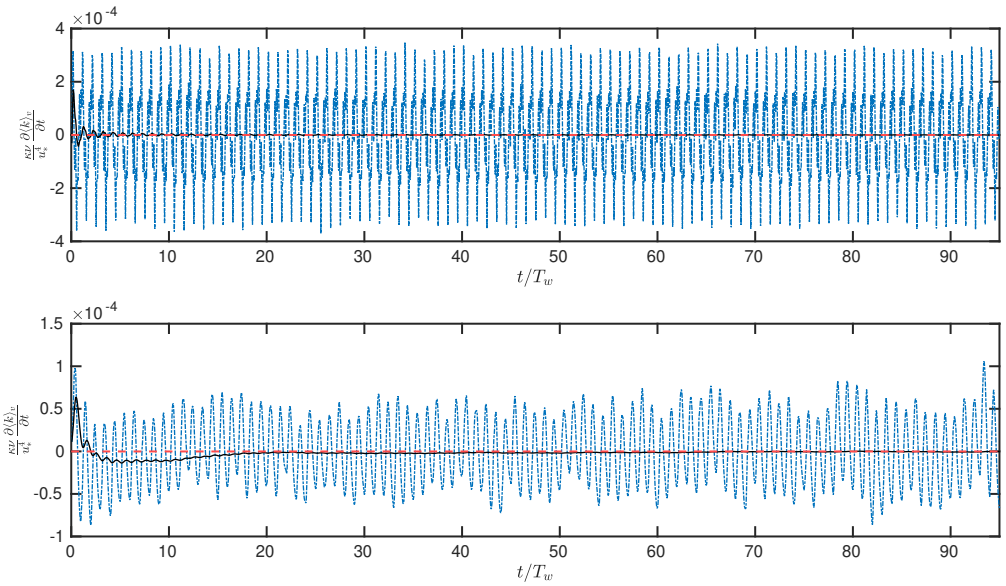

Figure 4.3: Convergence history for cases WC4780B21 (top) and WC4780F (bottom). Time on the x axis is normalised using the wave period, while the time rate of change of TKE is normalised by $u_*^4/\kappa\nu$. Blue dash-dot line marks the instantaneous value of $\partial_t\langle k\rangle$, black solid line marks the cumulative mean until time t and the red dashed line marks the target value of 0 that represents convergence.

$$\frac{\langle \overline{u}_1 \rangle}{u_*} = \frac{1}{\kappa} \ln\left(\frac{x_3 u_*}{\nu}\right) + B + \Delta U_s, \tag{4.10}$$

where $\langle \overline{u}_1 \rangle$ is the time- and planform-averaged streamwise velocity profile, $\kappa = 0.4$ is the von Kármán constant, $B = 5.2$ is an integration/empirical constant and ΔU_s represents the effect of roughness, body forcing, etc., and is negative when there is increased flow drag and positive when there is decreased flow drag. For case CF, $\Delta U_s = 0$, while for case WC4780F, $\Delta U_s = +1.42$. This upward shift in the log-law region is indicative of decreased flow drag and is observed for wave-dominated flow conditions over a flat wall, wave-current boundary layer that is transitioning to a fully turbulent state as marked in figure 4.2 (Lodahl et al., 1998; Scotti and Piomelli, 2001; Manna et al., 2012, 2015; Nelson and Fringer, 2018). Since the time-averaged driving pressure gradient is the same for cases CF and WC4780F, the increased time-averaged velocity profile for case WC4780F indicates that the addition of an oscillatory pressure gradient modulates the turbulence dynamics in a way that decreases the drag coefficient as described in Lodahl et al. (1998), Scotti and Piomelli (2001), and Manna et al. (2012).

Case CB21 shows significant changes across the entire velocity profile. Within the roughness region ($x_3^+ < 21$) the time- and planform-averaged velocity is zero. Thereafter, the velocity exhibits a buffer layer-like region which is strongly affected by the shear layer that develops due to flow separation at the top of the roughness elements. This flow separation modifies the slope of the velocity profile just above the roughness elements. A generalised log-law for the rough wall cases is given by (Raupach et al., 1991)

$$\frac{\langle \overline{u}_1 \rangle}{u_*} = \frac{1}{\kappa} \ln\left(\frac{x_3 - \overline{k}_s}{z_0}\right), \tag{4.11}$$

where $z_0 = \overline{k}_s/\alpha_k$ and α_k is a regression constant. Comparing the best fit value of

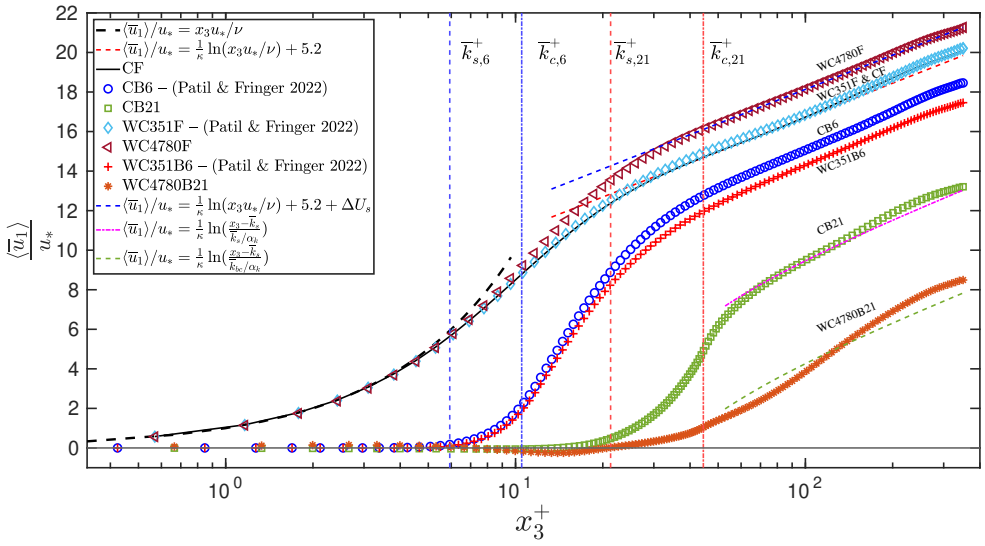

Figure 4.4: Time- and planform-averaged velocity profiles for the various DNS cases detailed in table 4.1. Vertical dashed lines mark the location of the roughness crest and mean roughness height for the two roughness heights. For cases CB21 and WC4780B21, only every other data point has been shown for clarity. For case CB21, the reference magenta-dashed line marks the log-law velocity profile obtained by regressing the value of $\alpha_k = 11.9$. As for case WC4780B21, the reference green-dashed line represents the analytical solution presented by Grant and Madsen (1979), with the apparent roughness ratio computed to $\overline{k}_{bc}/\overline{k}_s = 8.01$.

$\alpha_k = 11.9$ for case CB21 suggests that the log-law region is substantially affected and shifts downwards when there are bumps, which is expected since case CB21 has roughness elements that increase the bottom drag. Since the blocking factor ($H/\overline{k}_s = 16.44 > 40$) for case CB21 is larger than the recommended value of 40 (Jiménez, 2004), we expect the log-law region to be strongly affected. We note that the amount by which the log-law region shifts downward is a function of the underlying roughness characteristics. In particular, since the roughness elements at the bottom are characterised by the Corey shape factor given by (Corey, 1949)

$$C_o = \frac{k_{s,x_1}}{\sqrt{k_{s,x_2} k_{s,x_3}}}, \tag{4.12}$$

where the x_i sub-script denotes the semi-axis lengths of the ellipsoidal roughness elements. For this particular case, $C_o = 0.6$, which gives a larger flow drag when compared to the spherical roughness elements with $C_o = 1$ (Julien, 2010), as discussed in Chapter 2.

Since case WC4780B21 has the same roughness as case CB21, any effects due to blocking should be identical, thus we do not expect α_k to change. As seen in figure 4.4, within the roughness region, the time- and planform-averaged velocity for case WC4780B21 is negligible for $x_3^+ < 9$. For $9 \leq x_3^+ < 21$, the velocity is negative as marked by the data points below the black horizontal line. This is not observed for any of the other cases and has substantial consequences for the turbulence dynamics. At the mean roughness height ($x_3^+ = 21$) the velocity is exactly zero and thereby increases without showing any typical features observed for the other cases listed in table 4.1. The velocity profile does not seem to exhibit a buffer layer as seen for case CB21. Additionally, the log-law exists for a small region away from the wall. The GM79 prediction of the log-law through the apparent roughness ($\overline{k}_{bc}$) is close to the numerical solution. As discussed earlier, we do not expect any changes in α_k, and

GM79 predicts the factor by which the apparent roughness ($\overline{k}_{bc}$) increases due to the addition of waves when compared to the mean roughness height ($\overline{k}_s$). Hence, the green dashed line in figure 4.4 marks the expected location of the velocity profile in the log-law region without any additional regression for α_k for case WC4780B21. Comparing the GM79 prediction and the location of the log-law region for case WC4780B21, it is clear to see that within the log-law region the location of the velocity profile predicts a velocity that is smaller in magnitude when compared to the numerical prediction for case WC4780B21. Since GM79 uses a time-invariant and bulk turbulent eddy viscosity (ν_t) to estimate the shear, it is expected that this model over-estimates ν_t during some of the wave phases (Grant and Madsen, 1979). Consequently, the GM79 prediction for the apparent roughness is larger than what is expected, consistent with the observations in figure 4.4. As noted by Grant and Madsen (1979) and Sleath (1991), experimenting with different formulations of ν_t can provide further insights into the differences observed in this time- and planform-averaged velocity profile. The lower slope of the velocity profile close to the roughness crests for case WC4780B21 is suggestive of the fact that we expect the TKE and Reynolds stress production rate to be lower when compared to case CB21. The TKE and Reynolds stress production terms involve the gradient of the time- and planform-averaged velocity ($\partial_{x_3}\langle\overline{u}_1\rangle$) and dominate the near wall region (in this case just above the roughness crest). In this region that is close to the wall, we anticipate strongly attenuated TKE and Reynolds stress production terms. However, it must be noted that the value of $\overline{k}_{bc}$ is not just an indicator of the location of the log-law region as shown in figure 4.4, but also includes the bulk effect of the changes occurring within the roughness elements. Consequently, despite the substantial (apparent) mismatch between the green dashed line and the velocity profile for case WC4780B21 in figure 4.4, the formulation of $\overline{k}_{bc}$ is quite accurate in the context of drag coefficient prediction as discussed below.

To quantify the effect of the roughness, we define the drag coefficient in two ways

given by

$$C_d^* = \frac{u_*^2}{\langle \overline{u}_1 \rangle_v^2}, \tag{4.13}$$

and

$$C_d = \left[\frac{\kappa}{\ln\left(z_0/H\right) - 1} \right]^2, \tag{4.14}$$

where the operator $\langle \rangle_v$ represents planform- and vertical-averaging and z_0 is the reference roughness height computed using the apparent roughness for each of the cases. Equation 4.14 assumes a log-law velocity profile to define the drag coefficient, while equation 4.13 includes the effect of the numerically predicted velocity profile through the vertical averaging operator. For the bumpy wall cases, the velocity profiles are integrated for $x_3^+ > 10$ (as shown in figure 4.4) to avoid bias due to the roughness region. Although the bias for the roughness region can be eliminated, the value of the drag coefficient computed using equation 4.13 is sensitive to the upper limit. As a result, for a large value of $H/\overline{k}_s$ the drag coefficient is sensitive to the limits of integration. Table 4.2 compares the drag coefficient obtained numerically against equation 4.14 that holds in the log-law region of the flow. Case WC4780F has a smaller drag coefficient when compared to the log-law prediction as observed by the elevated log-law region when compared to case CF as seen in figure 4.4. Case CB21 has a slightly larger drag coefficient which can be attributed to the lower Corey shape factor leading to slightly higher drag. Additionally, since the value of z_0 is obtained through the regression of α_k that best fits in the log-law region, $C_o = 0.6$ results in a velocity profile that is relatively smaller just above the roughness region when compared to spherical roughness elements with $C_o = 1$. These effects lead to a larger value of C_d^* for case CB21. However, for case WC4780B21, which has identical roughness features as case CB21, the drag is substantially larger (see table 4.2) when compared to case CB21. As seen in table 4.2, the log-law prediction of C_d matches the numerical prediction

Acronym	Re_*	Re_w	z_0/H $(\times 10^{-4})$	C_d^* $(\times 10^{-3})$	C_d $(\times 10^{-3})$
CF	350	0	3.17	3.23	3.22
CB21	350	0	51.10	9.51	8.75
WC4780F	350	4780	3.17	2.90	3.22
WC4780B21	350	4780	408.74	32.30	33.14

Table 4.2: Comparison of drag coefficients computed using equations 4.13 and 4.14. For the flat wall cases, $z_0 \equiv \nu/(9u_*)$, while $z_0 \equiv \overline{k}_{bc}/\alpha_k$ for the bumpy wall cases, where $\overline{k}_{bc}$ is the apparent roughness and $\alpha_k = 11.9$ is the best fit regression parameter.

very well. However, this is not surprising as the results in table 4.2 are computed based on GM79 solution for apparent roughness $\overline{k}_{bc} = 8\overline{k}_s$ which is obtained by enforcing the log-law relationship. Despite the oversimplified modelling assumptions detailed in Section 4.3, GM79 prediction is acceptable. It is important to note that when computing the value of z_0 for case WC4780B21, the value of α_k is not regressed to match the log-law prediction. Instead, the same value as case CB21 is used for α_k. As a result, the data point presented in table 4.2 for case WC4780B21 is the non-regressed value obtained by using the apparent roughness $\overline{k}_{bc} = 8\overline{k}_s$, where the factor 8 is obtained after solving equation 4.5 using the requisite input conditions. It is important to note that the right prescription of the apparent roughness (z_0) is essential for most operational coastal ocean models which have grid resolutions on the order of 10 cm in the vertical direction. This grid resolution does not resolve the essential near-wall turbulence and thus requires accurate specification of z_0 as this parameter governs the behavior of other essential processes such as sediment erosion, transport of passive and active scalars to list a few.

The wave velocity solution for case WC4780F (not shown here) follows the Stokes' solution (Stokes, 1851) since the flow is one-way coupled as validated by multiple studies (Lodahl et al., 1998; Scotti and Piomelli, 2001; Manna et al., 2012, 2015; Nelson and Fringer, 2018). Figure 4.5 compares the numerical solution for case WC4780B21 to the analytical solution proposed by GM79. Outside the wave boundary layer and

far from the wall, the numerical solution is identical to the prediction by GM79. If the top of the wave boundary layer is defined as the location where the velocity profile is equal to 99% of the wave orbital velocity (U_b), then the wave boundary layer $\delta_w \sim 0.4A$. It is important to note that the actual boundary layer thickness defined earlier changes as a function of the wave phase and can be clearly seen in figure 4.5. Within the boundary layer, the wave velocity is significantly different from the GM79 predictions. The numerical wave solution is consistently larger in magnitude when compared to GM79 at all wave phases. As mentioned earlier, because the eddy viscosity is over-predicted by GM79, the velocity predictions are expected to be smaller when compared to DNS results. We expect that this effect is stronger for larger wave Reynolds numbers because the bulk eddy viscosity is expected to be significantly larger than the true phase-averaged eddy viscosity. This discrepancy was also observed by Cowherd et al. (2021) for in-situ measurements of wave-current boundary layers in San Francisco Bay. However, both GM79 and Cowherd et al. (2021) under predict the maximum wave velocity when compared to the DNS results in figure 4.5.

4.5.2 Time- and planform-averaged stress profiles and anisotropy tensors

As explained in detail in Patil and Fringer (2022), the time- and planform-averaged stress profile is given by

$$\frac{\langle \overline{\tau} \rangle}{u_*^2} = 1 - \frac{x_3}{H}, \tag{4.15}$$

where $\langle \overline{\tau} \rangle$ is the stress with units of velocity squared given by

$$\langle \overline{\tau} \rangle = \underbrace{\nu \frac{\partial \langle \overline{u}_1 \rangle}{\partial x_3}}_{\text{Viscous Stress}} - \underbrace{\langle \overline{u_1' u_3'} \rangle}_{\text{Reynolds Stress}} + \underbrace{\langle \overline{\tau} \rangle_d}_{\text{Dispersive Stress}} + F_{\text{IBM}}, \tag{4.16}$$

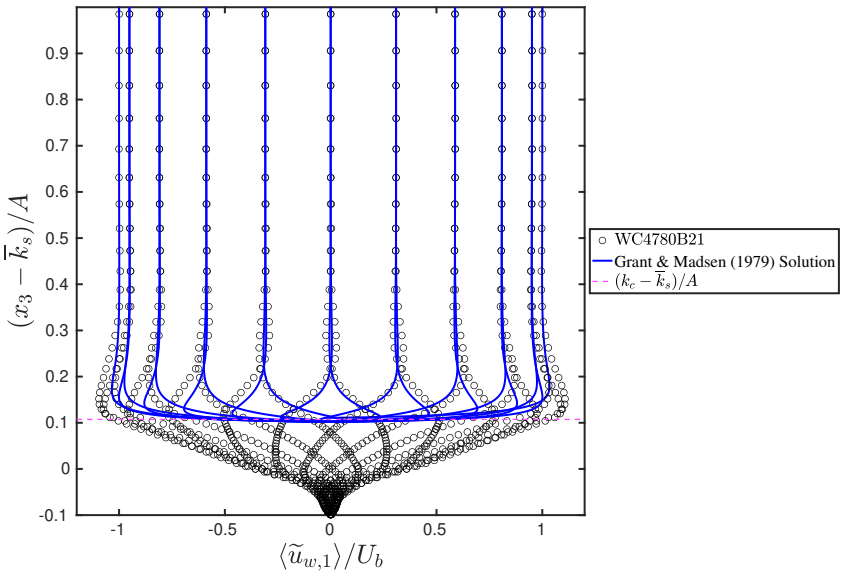

Figure 4.5: Comparison of the wave velocity component for Case WC4780B21 against the analytic solution proposed by GM79. Note that the analytic solution only applies to the portion of the flow above the roughness elements. Thus, the solution origin is set to $\overline{k}_s = 21$.

where the dispersive stresses (defined in Patil and Fringer (2022)) vanish with increasing distance from the rough wall, and the immersed boundary force $F_{\text{IBM}} = 0$ for $x_3^+ > \overline{k}_c^+$.

For the flat wall cases, the dispersive stress and the immersed boundary force are zero. As shown in figure 4.6 (a), for case WC4780F, close to the wall, the viscous stress (VS) dominates the contribution to the total stress, while the Reynolds stress (RS) is small. The total stress for this case exactly matches the analytical solution of the linear stress given by equation 4.15. For case CB21, close to the wall, the immersed boundary force and the dispersive stresses (not shown) dominate the stress balance as both the Reynolds and viscous stresses are negligible. Close to the mean roughness height, both RS and VS contributions to the total stress start becoming significant. With VS dominating initially, the RS dominates far from the wall as the viscous effects are smaller. Above the roughness crest, the total stress profile is

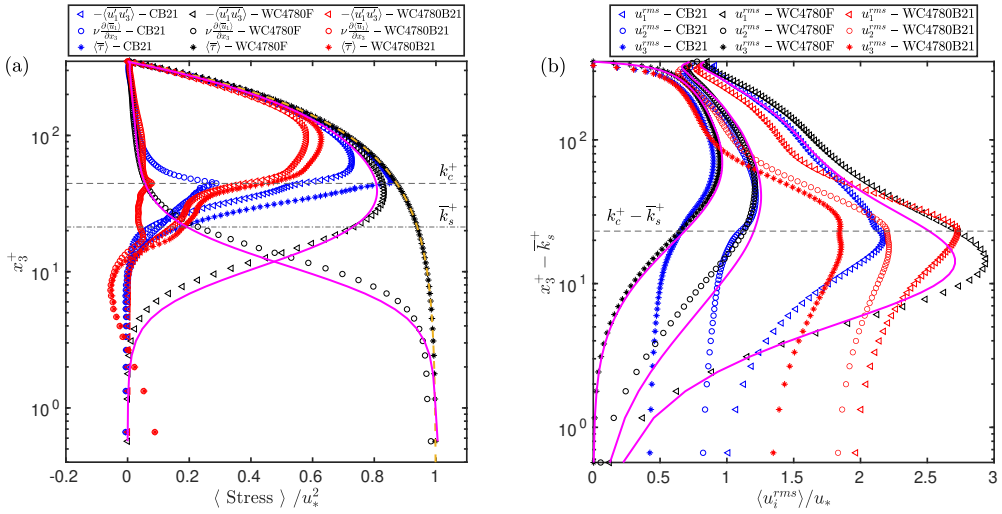

Figure 4.6: (a) Comparison of time- and planform-averaged viscous ($\nu \partial_{x_3} \langle \overline{u_1} \rangle$), Reynolds ($-\langle \overline{u_1' u_3'} \rangle$) and total stress ($\langle \overline{\tau} \rangle$), for cases CB21, WC4780F and WC4780B21. Note that the dispersive stress and the immersed boundary forcing are not shown. (b) Root-mean-squared (RMS) turbulent velocity components for cases CB21, WC4780F and WC4780B21. Because the y-axis is a log-scale, negative values of $x_3^+ - \overline{k}_s^+$ are not shown. Solid magenta line on both panels correspond to case CF.

exactly matched by the sum of VS and RS, although it is important to note that instantaneously, significant overshoots are observed due to flow separation events at the roughness crest. The contribution of the VS is maximum at the roughness crests and thereafter decreases rapidly (note the y axis is a log scale) and asymptotes to zero with increasing distance from the wall. The contribution of the RS increases with increasing distance from the wall and equals VS just above the mean roughness height for case CB21. The peak RS is smaller in magnitude when compared to the peak RS for case WC4780F suggesting that the dispersive stresses contribute significantly below the roughness crest.

Case WC4780B21 shows significantly different behavior despite identical bumps as case CB21. The viscous stress has a peculiar negative maximum below the mean roughness height. The sign of the viscous stress is determined by the sign of the

mean velocity gradient which would imply that the turbulent kinetic energy and Reynolds stress production terms are locally negative, thus implying upscale transport. The locally negative viscous stress magnitude is expected to increase with increasing wave Reynolds numbers and was also observed by Patil and Fringer (2022) for case WC351B6 listed in table 4.1. Further from the wall, the viscous stress magnitude is substantially smaller and is limited by the presence of the roughness elements as clearly seen by two sharp peaks. This locally negative velocity cannot be explained by the turbulent asymmetric streaming introduced in Yuan and Madsen (2015) as there is no higher-order Stokes correction type forcing included in the wave forcing given by equation 4.6. The sinusoidal nature of the wave forcing does not lead to a mean flow in the streamwise direction, thus the origin of this negative velocity region is unclear and beyond the scope of this work.

As shown in figure 4.6(b), the streamwise turbulent rms velocity component exhibits a consistently larger magnitude across the entire vertical profile when compared to case CF. The spanwise and vertical rms velocity components are consistently smaller in magnitude close to the wall compared to case CF and are not able to recover until $x_3^+ \sim 250$, i.e. very close to the top wall of the channel. Despite the attenuation, the rms velocity profiles for case WC4780F retain the shape for all the components across the entire vertical profile. Case CB21 exhibits strong attenuation in the streamwise component for $(x_3^+ - \overline{k}_s^+) < 50$, while the other two components are significantly enhanced below the roughness crest when compared to case WC4780F. Above the roughness crest, the streamwise component has a consistently smaller magnitude when compared to case WC4780F with clear signs of a roughness affected region above the roughness crest. The spanwise and vertical components for case CB21 follow case WC4780F closely just above the roughness elements, while further from the wall, slightly smaller magnitudes are observed. Between the mean roughness height and the roughness crest, the non-streamwise components undergo substantial

enhancement at the expense of the streamwise component. Immediately above the mean roughness height (i.e., $x_3^+ - \overline{k}_s^+ = 0$), the magnitudes of the streamwise and the vertical rms velocity components are approximately similar in magnitude suggesting that the roughness acts to reduce the anisotropy associated with the large scales (Gerolymos and Vallet, 2016) close the wall (further discussed in figure 4.7). For case WC4780B21, the global peak of the streamwise rms velocity component is smaller than that of case WC4780F. However, just above the roughness crest, similar profiles are observed for roughly 25 wall units, followed by consistent reduction in the magnitude compared to both cases CB21 and WC4780F. Similar to case CB21, just above the mean roughness height, the streamwise and spanwise rms velocity components exhibit comparable magnitudes. The spanwise rms velocity peak for case WC4780B21 is slightly larger than the streamwise rms velocity peak for case CB21 at the roughness crest, while it significantly attenuates over the next 80-100 wall units and is equal to the spanwise rms velocity profile of case CB21. The vertical rms velocity components also exhibits similar behavior as seen for the spanwise component. The region over which case WC4780B21 is observed to substantially differ from case CB21 corresponds exactly to the wave-boundary layer thickness observed in figure 4.5 (i.e., $x_3^+ - \overline{k}_s^+ \sim 0.4A \sim 10^2$).

Changes observed in the rms velocity profiles are indicative of potential changes to the Reynolds stress tensor $r_{ij} \equiv u_i' u_j'$, thus by extension imply changes to the Reynolds stress anisotropy tensor, the non-dimensional form of which is given by (Lumley, 1979)

$$b_{ij} = \frac{r_{ij}}{r_{ll}} - \frac{1}{3}\delta_{ij}. \tag{4.17}$$

Figure 4.7 compares the time- and planform-averaged anisotropy tensor terms for four cases as a function of the vertical coordinate. Away from the wall, there are

some differences observed between the magnitudes of all the components of b_{ij}. This is expected as b_{ij} is indicative of large-scale anisotropy and is sensitive to the size of the computational box used to resolve the large scales in the flow (Reynolds and Lee, 1985; Gerolymos and Vallet, 2016). Thus, we expect that the reliability of predicting b_{ij} degrades with increasing distance from the wall for a fixed box size with the different forcing and boundary conditions introduced here. Case WC4780F shows enhanced anisotropy for all components except b_{13} across the entire vertical profile when compared to case CF except at the very top of the channel. For all components of case WC4780F, as discussed earlier, the choice of the box size introduces significant differences at the top wall of the domain, thus the differences close to the top wall cannot be attributed reliably to the changes in the forcing conditions. As for component b_{13} of case WC4780F, minor attenuation is observed for $x_3^+ > 50$ i.e., above the buffer layer region, presumably as a consequence of increased magnitudes of the other components. The flat nature of the wall for case WC4780F does not introduce any other substantial differences close to the wall in stark contrast to the other two cases.

The anisotropy component b_{11} for case CB21 shows strongly diminished magnitudes below the mean roughness height ($\overline{k}_s^+$), with a global minimum observed just below $\overline{k}_s^+$. Between the mean roughness height and the roughness crests ($\overline{k}_c^+$), b_{11} changes trend and increases to reach the global maximum just below $\overline{k}_c^+$. Above $\overline{k}_c^+$, b_{11} monotonically increases with increasing x_3^+. Component b_{12} for the flat wall cases is expected to be zero and the numerical solutions for both the flat wall cases predict profiles that integrate to zero with case WC4780F showing a minor imprint of the wave boundary layer close to the bottom wall. Case CB21 exhibits enhanced magnitudes below $\overline{k}_s^+$ with a negative peak close to the wall and a positive peak (smaller in magnitude compared to the negative peak) just below the mean roughness height, thereafter decreasing and following a similar trend as case CF with some

minor oscillations.

Component b_{13} has been widely discussed through the definition of the structure parameter (Scotti and Piomelli, 2001)

$$\langle \overline{M}_r \rangle = -\frac{\langle \overline{u_1' u_3'} \rangle}{\langle \overline{u_l' u_l'} \rangle} \tag{4.18}$$

which suggests $b_{13} = -M_r$. Note that the time- and planform-averaging operators are presented here in the context of figure 4.7, and one could independently define an instantaneous structure parameter without any averaging operations. Using the structure parameter interpretation, case CB21 is observed to effectively convert the available TKE to RS for $x_3^+ < 100$. Further from the wall, some oscillations are observed about the b_{13} profile of case CF, thereafter decaying and following case WC4780B21. These results suggest that case CB21 is able to effectively convert the available TKE to RS close to the bottom wall when compared to case CF. However, further from the wall in the log-law region, this efficiency saturates and is lower when compared to case CF. The spanwise normal component b_{22} has a peak with positive magnitude below the mean roughness height followed by a rapid change in the slope and a negative peak just below the roughness crest. This negative peak for case CB21 is smaller in magnitude when compared to the flat wall cases, indicating decreased local anisotropy. Above the roughness crest, the anisotropy in b_{22} increases relative to the flat wall cases and stays this way for the rest of the vertical profile. Interestingly, the b_{23} component is observed to be strongly negative below the mean roughness height and goes to zero at the roughness crest followed by oscillations around a small negative value. It is not clear why this case shows strong oscillations above the buffer layer region, although we expect that this is a consequence of flow separation above the roughness crest and not a consequence of the lack of sample size for computing averages as the other statistics have converged. Lastly, the vertical normal component

b_{33} shows identical reduction in anisotropy below the mean roughness height, followed by a local recovery to match case CF around the roughness crest region and eventual increase in the magnitude above the buffer layer similar to the other components. There are no significant changes in the shape of the anisotropy profiles observed for this case apart from some oscillations around the profiles of case CF.

Case WC4780B21 shows elevated attenuation of anisotropy across all the tensor components that otherwise exhibit larger magnitudes i.e., b_{11}, b_{13}, b_{22} and b_{33} near the bottom wall. However, away from the wall, the normal components i.e., b_{11}, b_{22} and b_{33} are observed to be consistently larger in magnitude when compared to case CF. Component b_{13} shows consistent reduction in magnitude across the entire profile unlike the normal components which are only enhanced above the buffer layer region. A small enhancement of b_{12} is observed for case WC4780B21, with most of this enhancement of magnitude concentrated below the mean roughness height. Additionally, it is clear to see that significant departures from case CB21 for all RS anisotropy components are observed below the wave boundary layer marked by the blue dotted line. These enhancements observed within the roughness region for the bumpy wall cases suggest re-organisation of the TKE locally through the return to isotropy (pressure-strain rate correlation) mechanisms (Lumley, 1979). This was hypothesised to be the mechanism driving the enhanced dissipation within the wall region for bumpy cases in the presence of weak waves (Patil and Fringer, 2022). These observations collectively provide further insights and support for the isotropisation of the turbulent velocity fields in the presence of roughness elements for wave-current boundary layers. Additionally, we note that effects of pressure-strain rate may be useful in estimating the right value of z_0 as observed in figure 4.4, despite the fact that most operational coastal ocean models do not resolve the near-wall dynamics due to the lack of grid resolution.

As discussed in Ma et al. (2021), the second-order structure function (D_{ij}) allows

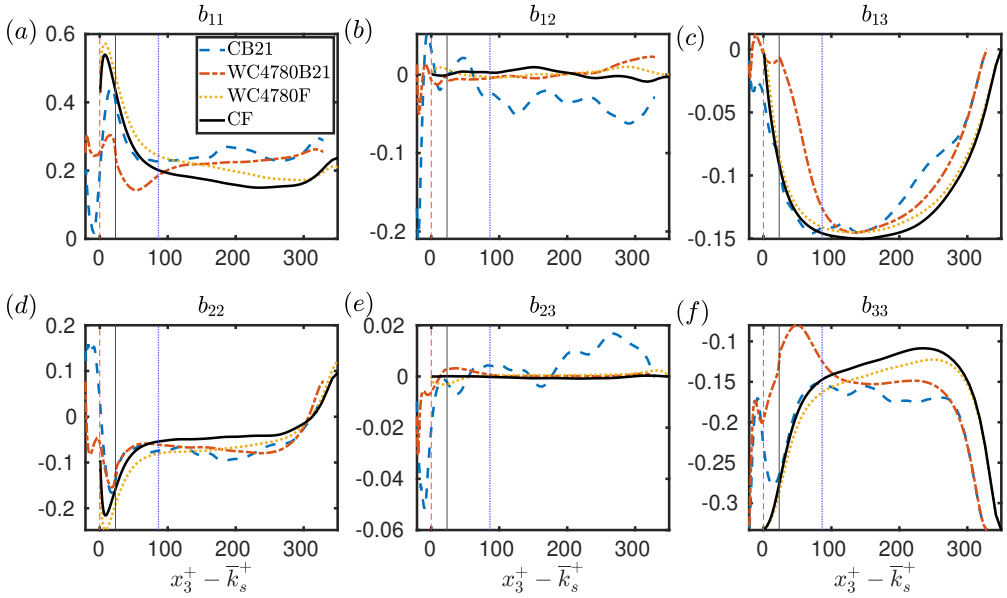

Figure 4.7: Comparison of the time- and planform-averaged Reynolds stress anisotropy (b_{ij}). Vertical dashed (red) line marks the location of the mean roughness height ($\overline{k}_s^+$), while the vertical solid (black) line marks the location of the roughness crest level ($\overline{k}_c^+$). Vertical dotted (blue) line marks the location of the top of the wave boundary layer for case WC4780B21.

the definition of a scale-local anisotropy tensor such that the deviation of D_{ij} from D_{ij}^{iso} denotes the level of anisotropy. Here, D_{ij}^{iso} represents isotropy for incompressible flows, which is different from a three-component flow which simply means that the magnitudes of the three turbulent velocity components are similar (see equations 3.1 - 3.4 in Ma et al. (2021)). However, Ma et al. (2021) show that for large scales ($\mathbf{r} \to \infty$), where $\mathbf{r}$ is the length scale, D_{ij}^{iso} represents the normal components of the Reynolds stress tensor. Consequently, the Reynolds stress tensor corresponds to anisotropy at the large scales where isotropy corresponds to a three-component flow (Rivlin, 1955; Gerolymos and Vallet, 2016; Ma et al., 2021). However, in the other limit ($\mathbf{r} \to 0$), three-component flow does not always correspond to isotropy. However, recognising that we have access to the entire three-dimensional velocity field and all its gradients, we can infer the state of isotropy from the dissipation anisotropy tensor (Rivlin, 1955; Pope, 2000; Gerolymos and Vallet, 2016)

$$b_{ij}^{\epsilon} = \frac{\epsilon_{ij}}{2\epsilon} - \frac{1}{3}\delta_{ij}, \tag{4.19}$$

where $2\epsilon \equiv \epsilon_{mm}$ and $\epsilon_{ij} \equiv 2\nu\partial_{x_m}u_i'\partial_{x_m}u_j'$. Figure 4.8 compares the dissipation anisotropy tensor (b_{ij}^{ϵ}) for the different cases discussed here. For the flat wall cases CF and WC4780F, the peak values of b_{ij}^{ϵ} are located within the viscous sub-layer ($x_3^+ < 5$) as expected for the normal components (i.e., $i = j$). For cases CF and WC4780F, except for minor changes to the magnitude of case WC4780F, there are no significant differences observed in the general behavior, suggesting that the small-scale anisotropy is not significantly affected by the oscillatory pressure gradient in the time-averaged sense. For case CB21, most of the anisotropy changes occur within the roughness layer below the mean roughness height. For the normal and b_{13}^{ϵ} components of the tensor, there is substantial magnitude reduction in the roughness region for case CB21 when compared to case CF. Thereafter, profiles for case CB21 seem to

follow case CF closely for about $x_3^+ \sim 100$ beyond which the normal components increase in magnitude when compared to case CF. However, b_{13}^ϵ decreases in magnitude when compared to case CF. As for the off-diagonal components b_{12}^ϵ and b_{23}^ϵ, most of the enhancements occur below the roughness crest above which the profiles oscillate around zero as expected. Note that for the off-diagonal components, the minor differences above the roughness crest are negligible in magnitude as the values are roughly three orders of magnitude smaller when compared to the other components. Similar to the RS anisotropy changes, most of the dynamical changes appear to occur at the bottom wall within the roughness region where we expect that most of the TKE is being re-organised and dissipated. As for case WC4780B21, the normal (or diagonal) components undergo similar reduction in magnitude as seen for case CB21 within the roughness region i.e., $x_3^+ < \overline{k}_c^+$. In addition to the effect of roughness, the imposed wave motion also appears to further reduce the anisotropy which is clearly visible for components b_{11}^ϵ, b_{13}^ϵ, and b_{33}^ϵ. Above the wave boundary layer, components b_{13}^ϵ and b_{33}^ϵ are enhanced while the other components closely follow case CB21. Despite these similarities observed in the normalised dissipation anisotropy, the dissipation magnitude for case WC4780B21 is an order of magnitude greater when compared to the other three cases discussed in this section. Thus, despite identical driving forces, the response of the wave boundary layer for case WC4780B21 is drastically different, as discussed in the following sections. This discussion about the large- and small-scale anisotropy shows the important dynamical differences observed for the bumpy wall cases with oscillatory wave forcing.

4.5.3 Wave phase variations of turbulence statistics

Wave phase variations in the Reynolds stress ($\widetilde{u_1' u_3'}$) as shown in figure 4.9 suggest strong phase variability in the response of the boundary layer turbulence. For a bumpy wall, steady turbulent channel flow, the u_3' vs. u_1' scatter is distributed mainly within

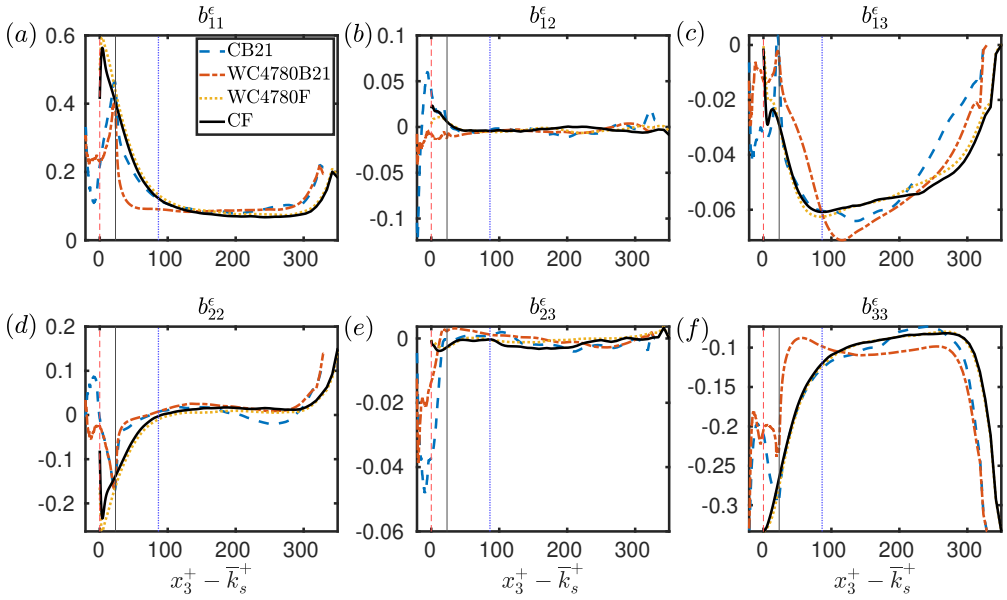

Figure 4.8: Comparison of the time- and planform-averaged dissipation anisotropy (b^{ϵ}_{ij}). Vertical dashed (red) line marks the location of the mean roughness height ($\overline{k}_s^+$), while the vertical solid (black) line marks the location of the roughness crest level ($\overline{k}_c^+$). Vertical dotted (blue) line marks the location of the top of the wave boundary layer for case WC4780B21.

the second and the fourth quadrants, giving $u_1' u_3' < 0$ (Pope, 2000; Cecchetto et al., 2017). For case WC4780B21, figure 4.9(a) shows that during the acceleration portion of the wave cycle ($U_b \omega \cos \omega t > 0$), there are more outward interactions (first quadrant events) that decrease the magnitude of the Reynolds stress (i.e., since $\overline{u_1' u_3'} < 0$, positive $u_1' u_3'$ events in the first quadrant make $\overline{u_1' u_3'}$ less negative). These outward interactions result in transport of faster moving streamwise turbulence components further from the wall ($u_1' > 0$ and $u_3' > 0$). The first quadrant events are enhanced until the wave velocity ($U_b \sin \omega t$) attains its peak positive maximum. Thereafter, the second quadrant events that increase the magnitude of the Reynolds stress start to dominate over the entire deceleration wave phase until $U_b \sin \omega t$ attains a negative maximum.

As shown in figures 4.9(b)-(c), immediately after the peak $U_b \sin \omega t$, the magnitude of the Reynolds stress increases due to an increase in the second quadrant events ($u_1' < 0$ and $u_3' > 0$). These phase variations are suggestive of widely varying changes observed in the boundary layer turbulence and have wide implications for estuarine systems. As discussed in Cecchetto et al. (2017) and Li et al. (2022), enhanced first quadrant events can contribute positively to suspended sediment entrainment and bed load transport. It is also important to note that the time-averaged Reynolds stress has a negative value within the roughness canopy (i.e., below the roughness crest) as shown in figure 4.6. Additionally, the enhancements observed in the first quadrant events are suggestive of increased vertical momentum transport in the presence of oscillatory wave motion.

In Section 4.5.2, the time- and planform-averaged anisotropy was used to describe the aggregate behavior of changing the boundary conditions (i.e., roughness) and body forcing (i.e., oscillatory wave motion) on the turbulence dynamics. The wave-phase variations of the anisotropy tensors given in equations 4.17 and 4.19 can help explain why the eddy-viscosity assumption appears to be valid for the wave-current boundary

layer case (see Section 4.3). The principal invariants of the RS anisotropy tensors can be used to characterise the level of local anisotropy (Lumley, 1979) through the anisotropy-invariant map (AIM) for different wave-phases. However, as detailed in Banerjee et al. (2007), the AIM in the non-linear space proposed by Lumley (1979) concentrates the data points towards the isotropic (or III component) point. To avoid this bias, we show the barycentric mapping of the AIM proposed by Banerjee et al. (2007) in figure 4.10 for case WC4780B21. It is important to note that case WC4780F does not show significant wave phase variability except for minor movement along line $I - II$ for the region close to the bottom wall. As a result, case WC4780F is not presented for the sake of brevity. As shown in figure 4.10, the region close to the bottom wall i.e., the roughness affected region, for all wave phases oscillates from the two component limit on the left to mid-way between I and II. With increasing distance from the wall, the RS anisotropy exhibits brisk variations as a function of the wave phase. It is critical to note that the wave velocity $U_b \sin \omega t$ lags the driving pressure gradient by $\pi/2$. During the acceleration phase of the wave velocity, i.e. panels (a)-(e), the region close to the wall moves from one component state in the phase diagram to the two component state. The region further from the wall approaches the axisymmetric expansion limit with the intermediate region developing a lobe connecting the axisymmetric contraction region to the axisymmetric expansion portion of the vertical profile. In panel (c), the vertical region $20 < x_3^+ < 80$ lies on the plane stress line marked in red, thereby crossing this state in the subsequent wave phase. Following the peak velocity as the wave velocity starts to decelerate close to the wall, i.e. panels (f)-(j), the region close to the wall stays on the left of the plane stress region marked by the red line, while the region further from the wall concentrates closer to the isotropic and axisymmetric expansion region. During the following wave cycle, i.e panels (k)-(o), the region close to the wall crosses the plane stress line momentarily to transition back to the left of this curve. However, the

region away from the bottom wall once again falls onto the axisymmetric expansion region. During the last portion of the wave cycle, i.e. panels (p)-(t), the lobe that develops during the acceleration phase in the intermediate region starts to roll back and concentrate along the axisymmetric expansion region to complete the wave cycle.

These observations suggest two interesting things about the boundary layer response to the oscillatory wave forcing. First, there are substantial differences between the region close to the bottom wall, the roughness affected region and the region away from the wall. The state of turbulence as a function of the wave phase has a clearly distinct response in the three regions. Secondly, as the RS anisotropy is indicative of large-scale anisotropy, there is good reason to suggest that the state of the RS anisotropy is in phase with the wave forcing, i.e. the oscillatory pressure gradient and not the wave velocity. This is clear to see as the axisymmetric contraction of the near-wall region is in phase with the wave forcing (blue dashed curve in figure 4.11). Because these changes are not observed for case WC4780F, they can be attributed to the roughness elements. Additionally, the wave phase behavior of the state of the turbulence suggests that the region above the roughness elements behaves more like isotropic, three-component turbulence during the deceleration phase of the wave cycle. The region close to the wall, on the other hand, oscillates between one- and two-component conditions depending on the wave phase.

4.5.4 Comments on the validity of the eddy-viscosity model

The above discussion suggests that for case WC4780B21, the eddy-viscosity model which assumes isotropic mixing is a relatively good choice because the flow at large scales becomes more three-component like and at the smaller scales it becomes relatively more isotropic. Therefore, because eddy-viscosity models assume isotropic mixing through the definition of the turbulent eddy-viscosity that is only a function

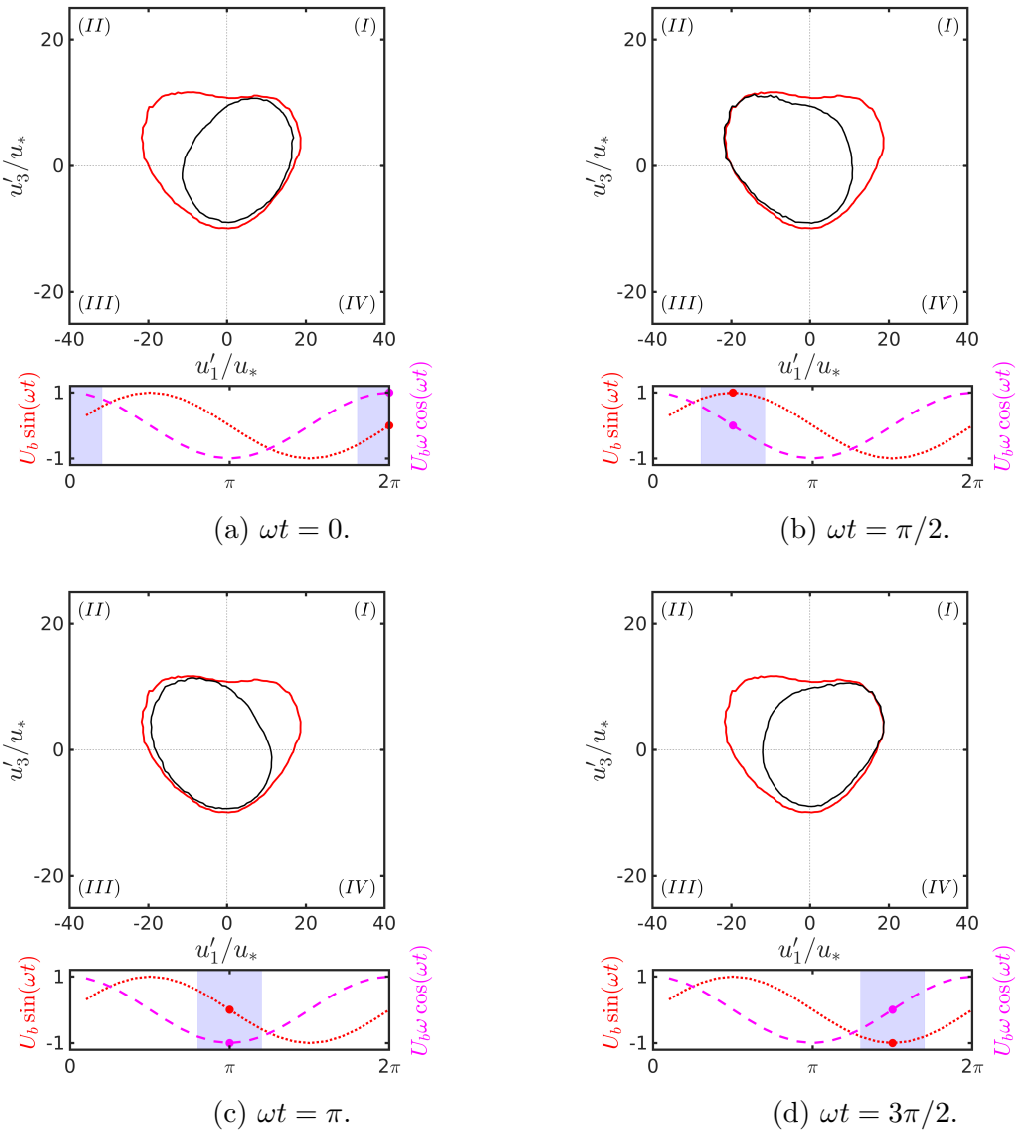

(a) $\omega t = 0$. (b) $\omega t = \pi/2$.

(c) $\omega t = \pi$. (d) $\omega t = 3\pi/2$.

Figure 4.9: Quadrat plots for case WC4780B21 using data just above the roughness crest at $x_3^+ = 50$, showing contours of the histograms with a value of 0.049 in $u_1' - u_3'$ space for data over the entire wave cycle (red) and limited to the phase interval marked in blue (black). In the time series panels below each histogram, the red dotted line shows the wave velocity ($U_b \sin \omega t$), while the magenta dashed line shows the oscillatory wave forcing ($U_b \omega \cos \omega t$) introduced in the streamwise momentum equation.

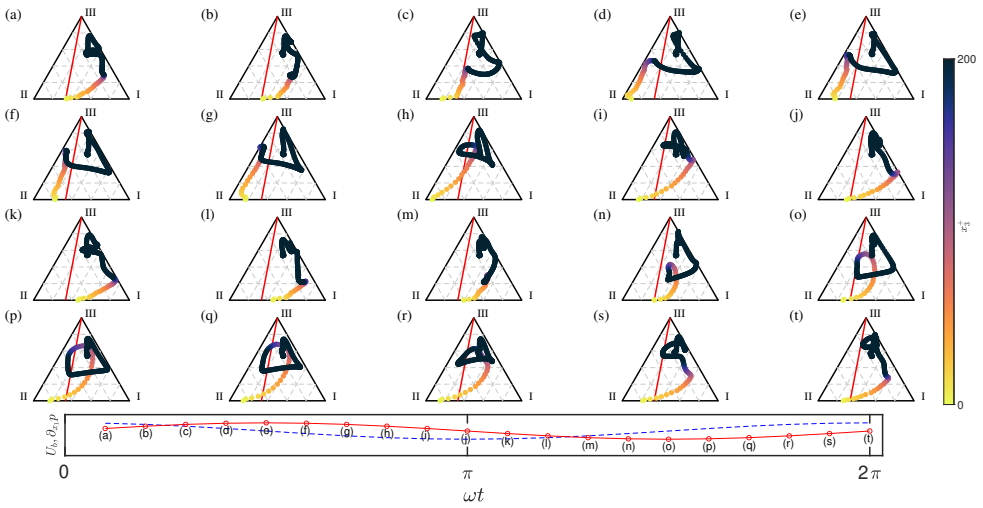

Figure 4.10: Barycentric AIM for case WC4780B21 with color shading represents the distance away from the wall. The vertical coordinate is capped at $x_3^+ = 200$ as there are no significant variations above this point. The red line marks the plane stress state in the AIM. The horizontal panel at the bottom portion of the figure shows the wave velocity as a function of the wave phase (red) along with the phase of each of the sub-panels with respect to the wave velocity. The blue dashed curve in this panel is the oscillatory pressure gradient (or wave forcing) in equation 4.6. Roman numerals I, II and III correspond to one-, two- and three-component (isotropic) turbulent conditions, respectively. Line $I - III$ marks the axisymmetric expansion limit, line $I - II$ marks the two-component limit and line $II - III$ marks the axisymmetric contraction limit.

of the vertical coordinate (i.e., x_3), this discussion supports the isotropic mixing assumption made in such models. The applicability of these models can be further quantified using the non-dimensional phase-averaged rate of straining given by

$$\langle \widetilde{S}_* \rangle = \frac{\partial \langle \widetilde{U}_1 \rangle}{\partial x_3} \frac{\langle \widetilde{k} \rangle}{\langle \widetilde{\epsilon} \rangle}, \tag{4.20}$$

where $\langle \widetilde{U}_1 \rangle$ is the phase- and planform-averaged velocity, $\langle \widetilde{k} \rangle \equiv \frac{1}{2} \langle \widetilde{u_i' u_i'} \rangle$ is the TKE and $\langle \widetilde{\epsilon} \rangle \equiv \nu \langle \widetilde{\partial_{x_j} u_i' \partial_{x_j} u_i'} \rangle$ is the dissipation rate of TKE. Note that equation 4.20 is specifically defined for the governing equations described in equation 4.6 assuming that the phase-averaged rate of strain (i.e., $\widetilde{S}_{ij} \equiv \frac{\partial \langle \widetilde{U}_i \rangle}{\partial x_j}$) is non-zero only for $i = 1$ and $j = 3$. Figure 4.11(a) shows that the time- and planform-averaged strain-rate ($\langle \overline{S}_* \rangle$) is relatively large close to the wall for cases CF and WC4780F. On the contrary, the bumpy wall cases CB21 and WC4780B21 have largely reduced values of $\langle \overline{S}_* \rangle$ in the vicinity of the roughness. Away from the wall, case CB21 is observed to closely follow cases CF and WC4780F, while case WC4780B21 shows elevated levels of $\langle \overline{S}_* \rangle$ away from the wall when compared to the other three cases. Cases CF and WC4780F peak just above the wall with case WC4780F showing an attenuated $\langle \overline{S}_* \rangle$ peak when compared to case CF. Similarly, case CB21 peaks just above the roughness crests with a strongly attenuated $\langle \overline{S}_* \rangle$ peak compared to case CF and approaches the flat wall profile at around 100 wall units on the compensated vertical coordinate. Case WC4780B21, on the other hand, shows negligible $\langle \overline{S}_* \rangle$ values for the first 100 wall units and is larger than the other cases thereafter. For the eddy-viscosity model to fail, $\langle \overline{S}_* \rangle > 1$, which is observed for cases CF and WC4780F close to the wall. The intrinsic assumption of the eddy-viscosity model states that locally (in space and time), the RS anisotropy is determined by the mean velocity gradient ($\partial U_i / \partial x_j$). Large values of $\langle \overline{S}_* \rangle$ indicate that the turbulence cannot rapidly adjust to the changing mean strain rate, and thus the local RS anisotropy cannot be governed by the local

mean strain-rate (Pope, 2000). Therefore, for cases CF and WC4780F the validity of the eddy-viscosity model close to the wall is less tractable when compared to the small values observed for case WC4780B21. This observations supports the model development choice made by GM79 as discussed in Section 4.3. We thus expect that the eddy-viscosity model is appropriate in the wave-current boundary layer framework over bumpy walls, and less so for the flat-wall counterparts which exhibit large values of $\langle \overline{S}_* \rangle$.

In addition to the non-dimensional strain-rate, the eddy-viscosity model assumes a local balance between the TKE production and the dissipation i.e., $\langle \overline{P}_k \rangle / \langle \bar{\epsilon} \rangle \approx 1$. As shown in figure 4.11(b), cases CF, WC4780F and CB21 exhibit a clear region where the TKE production approximately balances the TKE dissipation in the inertial range i.e., $50 < x_3^+ < 200$, while case WC4780B21 does not show any significant sign of such a local balance. This is also clear from figure 4.4 where case WC4780B21 does not show a substantial log-law region as seen for the other three cases. It is important to note that the DNS simulations considered in the present study do not show an appreciable overlap layer because DNS is unable to reach the channel depth and grid resolution required to resolve these large scales i.e., a large separation between small and large scales ($Re_* \gg 350$) for wave-current boundary layer flows over rough walls. However, this is not a deterrent because the turbulence model developed by GM79 aims to parameterise the region of the flow close to the wall while assuming that the rest of the water column is inviscid as required by the linear wave theory. Additionally, the lack of a persistent log-law region as seen in figure 4.4 is not concerning since we expect that the inner and outer layers are independent, and the inner layer merely sets the apparent roughness as seen by the outer layer (Grant and Madsen, 1979; Townsend, 1976; Jiménez, 2004).

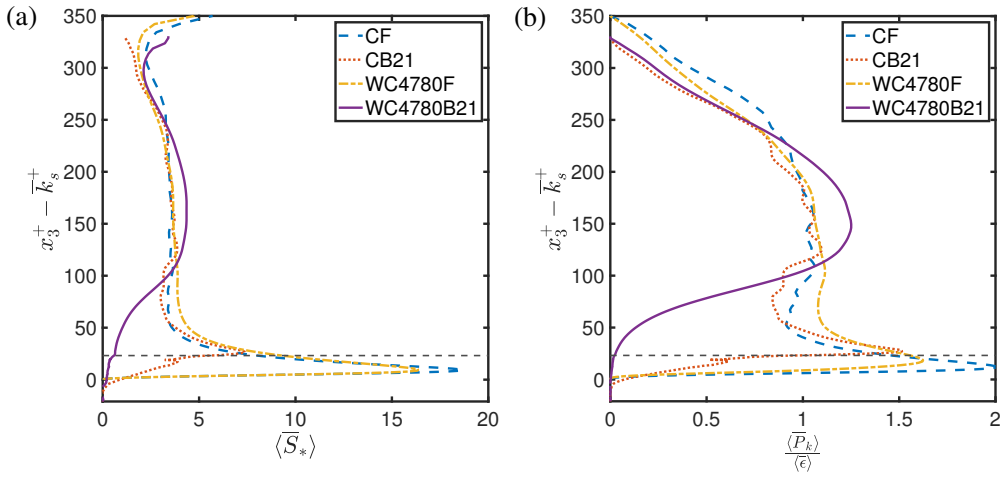

Figure 4.11: (a) Comparison of the vertical profiles of time- and planform-averaged non-dimensional strain rate. (b) Comparison of the vertical profiles of the ratio of TKE production over TKE dissipation rate. The horizontal dashed line marks the location of the roughness crest for the bumpy wall cases on both panels.

4.6 Conclusions

We studied the turbulence dynamics of a wave-dominated, wave-current boundary layer over transitionally rough walls to understand the turbulence dynamics and the applicability of the eddy-viscosity modeling approach as developed by Grant and Madsen (1979). The addition of a transitionally-turbulent wave to a turbulent mean flow over flat walls produces a characteristic flow drag reduction when compared to the flow drag in the absence of wave motion as first observed by Lodahl et al. (1998). However, identical flow conditions over bumpy walls lead to a substantial increase in the flow drag consistent with the analytical predictions made by Grant and Madsen (1979). It was observed that, while the flat wall wave-current case agrees with the analytical solution proposed by Stokes (1851), the bumpy wall wave-current case shows significant deviations from both the analytical solution proposed by Stokes (1851) and Grant and Madsen (1979). Nevertheless, the wave-current case over bumpy walls exhibits a mean roughness height that is consistent with the

Grant and Madsen (1979) theory, in that it is approximately eight times larger when compared to the bumpy wall case in the absence of waves.

Comparison of the total stress profiles suggests that above the top of the roughness elements, the total stress profile is linear, as expected for all the cases discussed in this paper. The rms velocity profiles provide the first indicators of significant alterations to the turbulence anisotropy observed for the bumpy wall cases where the presence of roughness elements significantly alters all component near the wall. These observations coupled with the time- and planform-averaged anisotropy tensors representing the large and small scales show that the flow close to the wall becomes significantly less anisotropic for the bumpy wall, wave-current case when compared to the flat wall, wave-current case. This is further supported by the time- and planform-averaged strain rate which is significantly reduced close to the bumpy wall thus rendering the eddy-viscosity approach tractable for turbulence modeling.

Chapter 5

Summary and conclusions

5.1 Summary of the results

This dissertation was a natural extension of the previous work done by Nelson (2018). My work addressed the recommendation in Nelson (2018) to understand the dynamics of wave-current boundary layers over bumpy walls. In this section, I provide a summary of the results.

Using a scale-resolving computational framework, my work solidifies our understanding of wave-current boundary layers over naturally rough bottom bathymetry akin to estuarine boundary layers. In Chapter 2, the primary focus was to quantify the effect of various roughness shapes through the definition of a Corey shape factor (C_o) on the mean flow drag in a steady turbulent channel flow. Through the use of full-span and minimal-span channel flow simulations, it was observed that there was a systematic increase in the mean flow drag with decreasing C_o. The mean flow drag for sand-grain type roughness (i.e., spherical roughness with $C_o = 1$), agrees with the Nikuradse (1933) estimate. The contribution of the form drag increased for cases with a smaller Corey shape factor due to flow separation. At the same time,

the viscous drag contribution to the total stress decreased. While this chapter provides insights into the systematic increase in the mean flow drag with decreasing C_o, the drag coefficient is a function of various other non-dimensional parameters that were held constant in addition to the procedure of sampling and generating the rough walls used in these simulations. As a result, these findings can be further solidified by exploring the effect of other relevant non-dimensional parameters listed in Chapter 2.

Having understood the effect of the Corey shape factor on the mean flow drag, in Chapter 3 I discussed the turbulence dynamics of wave-current boundary layers in weak wave (i.e., current-dominated) boundary layers over hydraulically smooth walls. By choosing $C_o = 0.6$ for the roughness, the interactions between a mean turbulent current and a laminar wave (oscillatory motion) were studied using direct numerical simulations. It was found that, unlike the flat wall, wave-current boundary layer, the wave-current boundary layer over hydraulically smooth bumps acts much like the wave-current boundary layer over a hydraulically rough wall. Specifically, the addition of oscillatory wave motion does not change the mean flow drag compared to the case with no waves over flat walls. However, the addition of oscillatory wave motion increases the mean flow drag by about 11% compared to the case with no waves over bumpy walls. This increase in the mean flow drag for the bumpy wall case resulted from increased pressure-strain rate correlations that scramble the energy across the three components. Additionally, the flow undergoes a net decrease in the turbulent kinetic energy production to dissipation rate ratio close to the wall, suggesting that even the presence of hydraulically smooth roughness elements affects the turbulence dynamics in such unsteady flows.

Finally, Chapter 4 presents a detailed discussion of the turbulence dynamics for wave-current boundary layers that represent realistic estuarine conditions. Wave-dominated flow conditions and hydraulically transitional wall conditions were studied to understand the applicability of simple bottom drag formulations used in large-scale

coastal ocean models. It was found that similar to the weak wave conditions, the turbulent velocities are re-organised to take on similar magnitudes in the vicinity of the rough wall due to the isotropisation at the dissipation scale through the pressure-strain rate correlation terms. Comparing the drag parameterisation developed by Grant and Madsen (1979) with the numerical results suggests excellent agreement providing further proof of its validity. Our observations support the drag parameterisation developed by Grant and Madsen (1979) through the changes observed in the dissipation anisotropy tensor and the mean strain rate.

It is my sincere hope that this dissertation improved our insights into the dynamics of unsteady, rough wall turbulent boundary layer flows through the use of a high-resolution numerical model. It goes without saying that additional work is needed to further expand our understanding of such coastal boundary layer flows and I have included my suggestions in the following section.

5.2 Future work

A lot remains to be understood and explained when it comes to turbulent flows over naturally rough walls. A central enigma in this literature is understanding the connection between the mean flow response and the underlying roughness characteristics. Specifically, the effect of sampling the orientation of the roughness elements used to generate the rough wall requires further attention and quantification. This can help provide insights into the potential origins of the enhanced drag upon reducing the Corey shape factor. Since $C_o = 1.0$ is invariant under rotation, the rough wall conforms to a regular array of spheres that is fundamentally different from the rough wall generated using roughness elements with $C_o \neq 1.0$. Additional simulations can be envisioned to understand the effect of sampling and rotation by placing the roughness elements with $C_o \neq 1.0$ without random rotations and comparing the results

to a rough bed generated using random rotations. Another approach would be to generate a rough wall using roughness elements with $C_o = 1.0$ but with spheres of different sizes. These additional simulations can provide fruitful insights by isolating the effect of random orientation and varying radii of the roughness elements used to generate the bumpy wall.

Real estuaries rarely experience perfectly sinusoidal oscillatory wave motion. Therefore, introducing higher harmonics to the oscillatory pressure gradient can help include the effects of non-linearity. Thus, the wave-current boundary layer flow can closely replicate some aspects of realistic estuarine conditions. The computational framework used in this dissertation can accurately and efficiently solve for the range of wave strength and relative roughness parameters as measured in Egan et al. (2020b). For example, the wave-current boundary layer cases simulated in this dissertation fall in the range of data collected in San Francisco Bay as shown in Figure 5.1. Comparing the numerical results with in-situ measurements as discussed in Egan et al. (2020b) can provide additional insights into the dynamics of such systems.

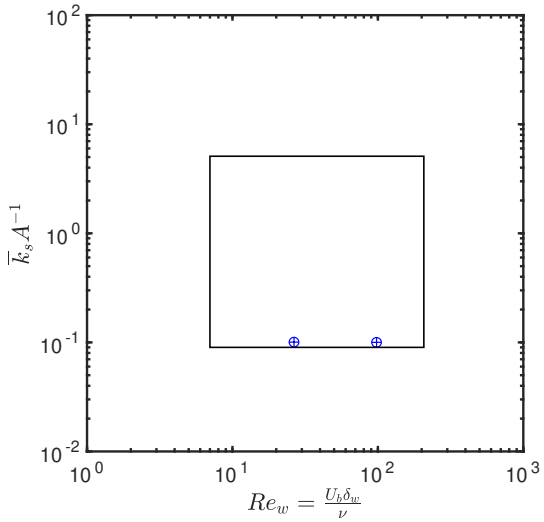

Figure 5.1: Comparison of the wave-current boundary layer cases simulated in this dissertation (blue plus-circle) to the parametric range of measurements in Egan et al. (2020b) (black rectangle).

With respect to turbulence modelling, improving the turbulence closures by including the effects of the pressure-strain rate may help include an important dynamic process that would otherwise be missing in two-equation closures. Another fruitful approach would be to understand the mean flow drag increase using an LES framework for increasing wave Reynolds numbers that cannot be simulated through the DNS framework. Given that the flow at large and small scales seems to become relatively three-component-like and isotropic, LES-type closures may provide a suitable way to retain the large-scale dynamics without imposing a large computational cost.

Finally, the effect of suspended-sediment-induced stratification can be included within the computational framework through the implementation of a scalar transport equation (with settling) as done in Nelson and Fringer (2018). This line of inquiry may further our understanding of realistic wave-current boundary layers in estuarine environments using numerical models.

Bibliography

Adelson, J. H. (2020). *Remote sensing of suspended sediment in San Francisco Bay using satellite and drone imagery.* PhD thesis, Stanford University.

Arnskov, M. M., Fredsøe, J., and Sumer, B. M. (1993). Bed shear stress measurements over a smooth bed in three-dimensional wave-current motion. *Coastal Engineering*, 20(3-4):277–316.

Bae, H. J. and Lee, M. (2021). Life cycle of streaks in the buffer layer of wall-bounded turbulence. *Phys. Rev. Fluids*, 6:064603.

Banerjee, S., Krahl, R., Durst, F., and Zenger, C. (2007). Presentation of anisotropy properties of turbulence, invariants versus eigenvalue approaches. *Journal of Turbulence*, 8:N32.

Barman, K., Debnath, K., and Mazumder, B. (2019). Turbulence over chains of hemispherical ribs under waves in a current. *Water Resources Research*, 55(1):55–75.

Barnard, P. L., Schoellhamer, D. H., Jaffe, B. E., and McKee, L. J. (2013). Sediment transport in the San Francisco Bay coastal system: An overview. *Marine Geology*, 345:3–17.

Bhaganagar, K. (2008). Direct numerical simulation of unsteady flow in channel with rough walls. *Physics of Fluids*, 20(10):101508.

Bosboom, J. and Stive, M. J. F. (2022). *Coastal Dynamics*. Delft University of Technology, Delft, The Netherlands.

Brasseur, J. G. and Lee, M. J. (1989). Pressure-strain rate events in homogeneous turbulent shear flow. In Fernholz, H.-H. and Fiedler, H. E., editors, *Advances in Turbulence 2*, pages 306–312, Berlin, Heidelberg. Springer Berlin Heidelberg.

Bricker, J. D., Inagaki, S., and Monismith, S. G. (2005). Bed drag coefficient variability under wind waves in a tidal estuary. *Journal of Hydraulic Engineering*, 131(6):497–508.

Cecchetto, M., Tregnaghi, M., Bottacin-Busolin, A., Tait, S., and Marion, A. (2017). Statistical description on the role of turbulence and grain interference on particle entrainment from gravel beds. *Journal of Hydraulic Engineering*, 143.

Chou, Y.-J. and Fringer, O. B. (2008). Modeling dilute sediment suspension using large-eddy simulation with a dynamic mixed model. *Physics of Fluids*, 20(11):115103.

Chow, F. K., Street, R. L., Xue, M., and Ferziger, J. H. (2005). Explicit filtering and reconstruction turbulence modeling for large-eddy simulation of neutral boundary layer flow. *Journal of the Atmospheric Sciences*, 62(7):2058–2077.

Chung, D., Chan, L., MacDonald, M., Hutchins, N., and Ooi, A. (2015). A fast direct numerical simulation method for characterising hydraulic roughness. *Journal of Fluid Mechanics*, 773:418–431.

Chung, D., Hutchins, N., Schultz, M. P., and Flack, K. A. (2021). Predicting the drag of rough surfaces. *Annual Review of Fluid Mechanics*, 53:439–471.

Clauser, F. H. (1954). Turbulent boundary layers in adverse pressure gradients. *Journal of the Aeronautical Sciences*, 21(2):91–108.

Cloern, J. E., Schraga, T. S., Nejad, E., and Martin, C. (2020). Nutrient status of San Francisco Bay and its management implications. *Estuaries and Coasts*, 43(6):1299–1317.

Conomos, T., Smith, R., and Gartner, J. (1985). Environmental setting of San Francisco Bay. *Hydrobiologia*, 129:1–12.

Corey, A. T. (1949). Influence of shape on the fall velocity of sand grains. Master's thesis, Colorado A and M College.

Cowherd, M., Egan, G., Monismith, S., and Fringer, O. (2021). Phase-resolved wave boundary layer dynamics in a shallow estuary. *Geophysical Research Letters*, 48(8):e2020GL092251.

Davis, K. A., Pawlak, G., and Monismith, S. G. (2021). Turbulence and coral reefs. *Annual Review of Marine Science*, 13:343–373.

del Álamo, J. C. and Jiménez, J. (2003). Spectra of the very large anisotropic scales in turbulent channels. *Physics of Fluids*, 15(6):L41–L44.

Deltares (2010). *Delft3D-FLOW, Simulation of multi-dimensional hydrodynamic flow and transport phenomena, including sediments*. Rotterdamseweg, Delft, The Netherlands.

Eckelmann, H. (1974). The structure of the viscous sublayer and the adjacent wall region in a turbulent channel flow. *Journal of Fluid Mechanics*, 65(3):439–459.

Egan, G., Chang, G., Revelas, G., Monismith, S., and Fringer, O. (2020a). Bottom drag varies seasonally with biological roughness. *Geophysical Research Letters*, 47:e2020GL088425.

Egan, G., Cowherd, M., Fringer, O., and Monismith, S. (2019). Observations of near-bed shear stress in a shallow, wave- and current-driven flow. *Journal of Geophysical Research: Oceans*, 124(8):6323–6344.

Egan, G., Manning, A. J., Chang, G., Fringer, O., and Monismith, S. (2020b). Sediment-induced stratification in an estuarine bottom boundary layer. *Journal of Geophysical Research: Oceans*, 125(8):e2019JC016022.

Fishler, L. and Brodkey, R. (1991). Transition, turbulence and oscillating flow in a pipe: A visual study. *Experiments in Fluids*, 11(6):388–398.

Flack, K. A. and Schultz, M. P. (2014). Roughness effects on wall-bounded turbulent flows. *Physics of Fluids*, 26(10):101305.

Flack, K. A., Schultz, M. P., and Rose, W. B. (2012). The onset of roughness effects in the transitionally rough regime. *International Journal of Heat and Fluid Flow*, 35:160–167.

Flores, O. and Jiménez, J. (2010). Hierarchy of minimal flow units in the logarithmic layer. *Physics of Fluids*, 22(7):071704.

Fredsøe, J. (1984). Turbulent boundary layer in wave-current motion. *Journal of Hydraulic Engineering*, 110(8):1103–1120.

Fringer, O. B., Gerritsen, M., and Street, R. L. (2006). An unstructured grid, finite-volume, nonhydrostatic, parallel coastal ocean simulator. *Ocean Modelling*, 14(3-4):139–278.

Gerolymos, G. A. and Vallet, I. (2016). The dissipation tensor in wall turbulence. *Journal of Fluid Mechanics*, 807:386–418.

Ghodke, C. D. and Apte, S. V. (2017). Roughness effects on the second-order turbulence statistics in oscillatory flows. *Computers and Fluids*, 162:160–170.

Glenn, S. M. and Grant, W. D. (1987). A suspended sediment stratification correction for combined wave and current flows. *Journal of Geophysical Research*, 92:8244.

Grant, W. D. and Madsen, O. S. (1979). Combined wave and current interaction with a rough bottom. *Journal of Geophysical Research: Oceans*, 84(C4):1797–1808.

Grant, W. D. and Madsen, O. S. (1986). The continental-shelf bottom boundary layer. *Annual Review of Fluid Mechanics*, 18(1):265–305.

Hama, F. R. (1954). Boundary layer characteristics for smooth and rough surfaces. *Transactions - The Society of Naval Architects and Marine Engineers*, 62:333–358.

Hao, Z. and Gorlé, C. (2020). Pressure scrambling effects and the quantification of turbulent scalar flux model uncertainties. *Physical Review Fluids*, 5(8):082501.

Hino, M., Sawamoto, M., and Takasu, S. (1976). Experiments on transition to turbulence in an oscillatory pipe flow. *Journal of Fluid Mechanics*, 75(2):193–207.

Huang, Y., Wang, L., and Fu, S. (2021). Drag reduction in turbulent channel flows by a spanwise traveling wave of wall blowing and suction. *Physics of Fluids*, 33(9):095111.

Hussain, A. K. M. F. and Reynolds, W. C. (1970). The mechanics of an organized wave in turbulent shear flow. *Journal of Fluid Mechanics*, 41(2):241–258.

Huynh-Thanh, S. and Temperville, A. (1991). A numerical model of the rough turbulent boundary layer in combined wave and current interaction. *In: Soulsby, R.L., Bettess, R. (Eds.), Sand transport in Rivers, Estuaries and the Sea. Balkema, Rotterdam.*

Jelly, T. O., Chin, R. C., Illingworth, S. J., Monty, J. P., Marusic, I., and Ooi, A. (2020). A direct comparison of pulsatile and non-pulsatile rough-wall turbulent pipe flow. *Journal of Fluid Mechanics*, 895:3.

Jensen, B., Sumer, B., and Fredsøe, J. (1989). Turbulent oscillatory boundary layers at high Reynolds numbers. *Journal of Fluid Mechanics*, 206:265–297.

Jiménez, J. (2004). Turbulent flows over rough walls. *Annual Review of Fluid Mechanics*, 36(1):173–196.

Jiménez, J. and Moin, P. (1991). The minimal flow unit in near-wall turbulence. *Journal of Fluid Mechanics*, 225:213–240.

Jonsson, I. G. (1966). Wave boundary layers and friction factors. *Coastal Engineering Proceedings*, (10):127–148.

Julien, P. Y. (2010). *Erosion and Sedimentation (2nd ed.)*. Cambridge University Press, Cambridge.

Kemp, P. H. and Simons, R. R. (1982). The interaction between waves and a turbulent current: Waves propagating with the current. *Journal of Fluid Mechanics*, 116:227–250.

Kemp, P. H. and Simons, R. R. (1983). The interaction of waves and a turbulent current: Waves propagating against the current. *Journal of Fluid Mechanics*, 130:73–89.

Kim, J. and Moin, P. (1985). Application of a fractional-step method to incompressible Navier-Stokes equations. *Journal of Computational Physics*, 59(2):308–323.

Kim, J., Moin, P., and Moser, R. (1987). Turbulence statistics in fully developed channel flow at low Reynolds number. *Journal of Fluid Mechanics*, 177:133–166.

Krogstad, P.-Å. and Antonia, R. (1994). Structure of turbulent boundary layers on smooth and rough walls. *Journal of Fluid Mechanics*, 277:1–21.

Lacy, J. R. and MacVean, L. J. (2016). Wave attenuation in the shallows of San Francisco Bay. *Coastal Engineering*, 114:159–168.

Li, R., Voulgaris, G., and Wang, Y. P. (2022). Turbulence structure and burst events observed in a tidally induced bottom boundary layer. *Journal of Geophysical Research: Oceans*, 127.

Lodahl, C. R., Sumer, B. M., and Fredsøe, J. (1998). Turbulent combined oscillatory flow and current in a pipe. *Journal of Fluid Mechanics*, 373:313–348.

López, F. and García, M. H. (1999). Wall similarity in turbulent open-channel flow. *Journal of Engineering Mechanics*, 125(7):789–796.

Lowe, R. J., Koseff, J. R., and Monismith, S. G. (2005). Oscillatory flow through submerged canopies: 1. Velocity structure. *Journal of Geophysical Research: Oceans*, 110(C10).

Lozano-Durán, A. and Bae, H. J. (2016). Turbulent channel with slip boundaries as a benchmark for subgrid-scale models in LES. *Annual Research Briefs. Center for Turbulence Research (U.S.)*, 2016:97–103.

Lozano-Durán, A. and Bae, H. J. (2019). Characteristic scales of Townsend's wall-attached eddies. *Journal of Fluid Mechanics*, 868:698–725.

Lozano-Durán, A., Flores, O., and Jiménez, J. (2012). The three-dimensional structure of momentum transfer in turbulent channels. *Journal of Fluid Mechanics*, 694:100–130.

Lozano-Durán, A. and Jiménez, J. (2014). Effect of the computational domain on direct simulations of turbulent channels up to $Re_\tau = 4200$. *Physics of Fluids*, 26(1):011702.

Lumley, J. L. (1975). Pressure-strain correlation. *Physics of Fluids*, 18(6):750.

Lumley, J. L. (1979). Computational modeling of turbulent flows. *Advances in Applied Mechanics*, 18:123–176.

Ma, T., Ott, B., Fröhlich, J., and Bragg, A. D. (2021). Scale-dependent anisotropy, energy transfer and intermittency in bubble-laden turbulent flows. *Journal of Fluid Mechanics*, 927:A16.

MacDonald, M., Chung, D., Hutchins, N., Chan, L., Ooi, A., and García-Mayoral, R. (2017). The minimal-span channel for rough-wall turbulent flows. *Journal of Fluid Mechanics*, 816:5–42.

Madsen, O. S. (1994). Spectral wave-current bottom boundary layer flows. *Coastal Engineering Proceedings*, 1(24).

Manna, M., Vacca, A., and Verzicco, R. (2012). Pulsating pipe flow with large-amplitude oscillations in the very high frequency regime. Part 1. Time-averaged analysis. *Journal of Fluid Mechanics*, 700:246–282.

Manna, M., Vacca, A., and Verzicco, R. (2015). Pulsating pipe flow with large-amplitude oscillations in the very high frequency regime. Part 2. Phase-averaged analysis. *Journal of Fluid Mechanics*, 766:272–296.

Mignot, E., Barthelemy, E., and D., H. (2009). Double-averaging analysis and local flow characterization of near-bed turbulence in gravel-bed channel flows. *Journal of Fluid Mechanics*, 618:279–303.

Miyake, Y., Tsujimoto, K., and Agata, Y. (2000). A DNS of a turbulent flow in a rough-wall channel using roughness elements model. *JSME International Journal Series B Fluids and Thermal Engineering*, 43(2):233–242.

Moin, P. and Kim, J. (1982). Numerical investigation of turbulent channel flow. *Journal of Fluid Mechanics*, 118:341–377.

Moin, P. and Verzicco, R. (2016). On the suitability of second-order accurate discretizations for turbulent flow simulations. *European Journal of Mechanics - B/Fluids*, 55:242–245.

Moody, F. (1944). Friction factors for pipe flow. *Trans. ASME*, 66:671–684.

Moser, R. D., Kim, J., and Mansour, N. N. (1999). Direct numerical simulation of turbulent channel flow up to $Re_\tau = 590$. *Physics of Fluids*, 11(4):943–945.

Murphy, E. A. K., Barros, J. M., Schultz, M. P., Flack, K. A., Steppe, C. N., and Reidenbach, M. A. (2018). Roughness effects of diatomaceous slime fouling on turbulent boundary layer hydrodynamics. *Biofouling*, 34:976–988.

Myrhaug, D. and Slaattelid, O. H. (1990). A rational approach to wave-current friction coefficients for rough, smooth and transitional turbulent flow. *Coastal Engineering*, 14:265–293.

Nelson, K. (2018). *Simulating suspended sediment dynamics in shallow-water wave- and current-driven environments.* PhD thesis, Stanford University.

Nelson, K. S. and Fringer, O. B. (2018). Sediment dynamics in wind wave-dominated shallow-water environments. *Journal of Geophysical Research: Oceans*, 123(10):6996–7015.

Nielsen, P. (1992). *Coastal bottom boundary layers and sediment transport*. Advanced series on ocean engineering. World Scientific Publishing Company, Singapore.

Nikora, V., McEwan, I., McLean, S., Coleman, S., Pokrajac, D., and Walters, R. (2007). Double-averaging concept for rough-bed open-channel and overland flows: Theoretical background. *Journal of Hydraulic Engineering*, 133(8):873–883.

Nikuradse, J. (1933). *Strömungsgesetze in rauhen Rohren*. VDI- Forschungsheft, 361, Berlin.

Orlandi, P. (2000). *Fluid Flow Phenomena, Volume 55 of Fluid Mechanics and Its Applications*. Springer Netherlands, Dordrecht.

Patil, A. and Fringer, O. (2022). Drag enhancement by the addition of weak waves to a wave-current boundary layer over bumpy walls. *Journal of Fluid Mechanics*, 947:A3.

Peruzzi, C., Vettori, D., Poggi, D., Blondeaux, P., Ridolfi, L., and Manes, C. (2021). On the influence of collinear surface waves on turbulence in smooth-bed open-channel flows. *Journal of Fluid Mechanics*, 924:6.

Pope, S. B. (2000). *Turbulent Flows*. Cambridge University Press, Cambridge.

Prandtl, L. (1925). Report on studies on developed turbulence/bericht über untersuchungen zur ausgebildeten turbulenz. *ZAMM - Journal of Applied Mathematics and Mechanics / Zeitschrift für Angewandte Mathematik und Mechanik*, 5:136–139.

Raupach, M. R., Antonia, R. A., and Rajagopalan, S. (1991). Rough-wall turbulent boundary layers. *Applied Mechanics Reviews*, 44(1):1–25.

Raupach, M. R. and Thom, A. S. (1981). Turbulence in and above plant canopies. *Annual Review of Fluid Mechanics*, 13(1):97–129.

Reynolds, W. C. and Lee, M. J. (1985). *Theoretical Approaches to Turbulence*, The structure of homogeneous turbulence. pages 231–261. Springer New York, New York, NY.

Rivlin, R. S. (1955). Further remarks on the stress-deformation relations for isotropic materials. *Journal of Rational Mechanics and Analysis*, 4:681–702.

Rogers, J. S., Maticka, S. A., Chirayath, V., Woodson, C. B., Alonso, J. J., and Monismith, S. G. (2018). Connecting flow over complex terrain to hydrodynamic roughness on a coral reef. *Journal of Physical Oceanography*, 48:1567–1587.

Schlichting, H. and Gersten, K. (2003). *Boundary-layer theory*. Springer Science & Business Media, New York, NY.

Schultz, M. P. and Flack, K. A. (2009). Turbulent boundary layers on a systematically varied rough wall. *Physics of Fluids*, 21:015104.

Schultz, M. P. and Myers, A. (2003). Comparison of three roughness function determination methods. *Experiments in Fluids*, 35:372–379.

Scotti, A. (2006). Direct numerical simulation of turbulent channel flows with boundary roughened with virtual sandpaper. *Physics of Fluids*, 18(3):031701.

Scotti, A. and Piomelli, U. (2001). Numerical simulation of pulsating turbulent channel flow. *Physics of Fluids*, 13(5):1367–1384.

Sleath, J. F. (1987). Turbulent oscillatory flow over rough beds. *Journal of Fluid Mechanics*, 182:369–409.

Sleath, J. F. A. (1991). Velocities and shear stresses in wave-current flows. *Journal of Geophysical Research*, 96:15237.

Soulsby, R. L., Hamm, L., Klopman, G., Myrhaug, D., Simons, R. R., and Thomas, G. P. (1993). Wave-current interaction within and outside the bottom boundary layer. *Coastal Engineering*, 21(1-3):41–69.

Spalart, P. R. and Baldwin, B. S. (1987). Direct simulation of a turbulent oscillating boundary layer. *NASA Tech. Mem. 89460 Ames Research Center, Moffett Field, California*.

Spalart, P. R. and Mclean, J. D. (2011). Drag reduction: Enticing turbulence, and then an industry. *Trans. R. Soc. A*, 369:1556–1569.

Stokes, G. G. (1851). On the effect of the internal friction of fluids on the motion of pendulums. *Trans. Cambridge Philos. Soc.*, 9:1–141.

Styles, R. and Glenn, S. M. (2000). Modeling stratified wave and current bottom boundary layers on the continental shelf. *Journal of Geophysical Research: Oceans*, 105:24119–24139.

Tamburrino, A. and Gulliver, J. S. (1999). Large flow structures in a turbulent open channel flow. *Journal of Hydraulic Research*, 37(3):363–380.

Teixeira, M. A. and Belcher, S. E. (2002). On the distortion of turbulence by a progressive surface wave. *Journal of Fluid Mechanics*, 458:229–267.

Thakkar, M., Busse, A., and Sandham, N. (2017). Surface correlations of hydrodynamic drag for transitionally rough engineering surfaces. *Journal of Turbulence*, 18:138–169.

Townsend, A. A. (1976). *The structure of turbulent shear flow (2nd ed.)*. Cambridge University Press, Cambridge.

van Doorn, T. (1981). Experimental investigation of near-bottom velocities in water waves with and without a current. Technical report, M1423, Delft Hydraulics, Delft, The Netherlands.

Volino, R. J., Schultz, M. P., and Flack, K. A. (2011). Turbulence structure in boundary layers over periodic two- and three-dimensional roughness. *Journal of Fluid Mechanics*, 676:172–190.

von Kármán, T. (1930). Mechanische Ähnlichkeit und turbulenz. *Nachrichten von der Gesellschaft der Wissenschaften zu Göttingen, Fachgruppe 1 (Mathematik)*, 5:58–76.

Wei, T. and Willmarth, W. (1989). Reynolds-number effects on the structure of a turbulent channel flow. *Journal of Fluid Mechanics*, 204:57–95.

Winterwerp, J. (2001). Stratification effects by cohesive and noncohesive sediment. *Journal of Geophysical Research: Oceans*, 106(C10):22559–22574.

Yu, X., Rosman, J. H., and Hench, J. L. (2022). Boundary layer dynamics and bottom friction in combined wave–current flows over large roughness elements. *Journal of Fluid Mechanics*, 931:A11.

Yuan, J. and Madsen, O. S. (2015). Experimental and theoretical study of wave-current turbulent boundary layers. *Journal of Fluid Mechanics*, 765:480–523.

Yuan, J. and Piomelli, U. (2014). Roughness effects on the Reynolds stress budgets in near-wall turbulence. *Journal of Fluid Mechanics*, 760:R1.

Yuan, J. and Piomelli, U. (2015). Numerical simulation of a spatially developing accelerating boundary layer over roughness. *Journal of Fluid Mechanics*, 780:192–214.

Zijlema, M., Stelling, G., and Smit, P. (2011). SWASH: An operational public domain code for simulating wave fields and rapidly varied flows in coastal waters. *Coastal Engineering*, 58:992–1012.